

Copyright
by
Keeseong Park
2007

The Dissertation Committee for Keeseong Park
certifies that this is the approved version of the following dissertation:

**Magnetic Phase Diagram of $\text{Ca}_{2+x}\text{Y}_{2-x}\text{Cu}_5\text{O}_{10-\delta}$:
Oxygen Hole-Doping Effects**

Committee:

John T. Markert, Supervisor

Alejandro de Lozanne

Zhen Yao

Allan MacDonald

John Goodenough

**Magnetic Phase Diagram of $\text{Ca}_{2+x}\text{Y}_{2-x}\text{Cu}_5\text{O}_{10-\delta}$:
Oxygen Hole-Doping Effects**

by

Keeseong Park, B.S.; M.S.

DISSERTATION

Presented to the Faculty of the Graduate School of
The University of Texas at Austin
in Partial Fulfillment
of the Requirements
for the Degree of

DOCTOR OF PHILOSOPHY

THE UNIVERSITY OF TEXAS AT AUSTIN

August 2007

Dedicated to my wife, Meejung and my daughter, Jeenah.

Acknowledgments

First of all, I wish to thank my supervisor, professor John T. Markert for his endless kindness and encouragement. I have learned a lot as a scientist, as a man, and as a new father from him. I want to thank Dr. Gan Liang in San Houston State University for his kind teaching and Dr. Jianshi Zhou in mechanical engineering department for his explanation to all my embarrassing questions.

I met many friends in my laboratory who should be recognized and kept in touch with in my post graduate school life. I remember Yong as a good friend to talk with about everything including physics, Korea, and even small things in common life. I wish Yong, his wife, Soyeun and his son, Junhyuong happiness. I remember Utkir who made my laboratory a pleasant place to work. I remember Wei who is always diligent and sincere. I wish Wei and his wife, Sun happiness. I remember Samaresh with whom I had good times in trying various challenging food around Austin. I remember Rosie who is always kind and ready to learn. I remember Han-jong who is always next to me on Thursday nights. I also want to say thanks Mark, and Isaac for the wonderful time in my laboratory. Sara, and my co-worker, Ted are best undergraduate researchers who I have ever known.

I wish to thank my 13th floor friends, Dagim, Yafis, Kang, Chang-

bae, Su-eon, Seongsoo, Junwei, Ming, Jeehoon, and Adrian for their pleasant smile and coffee breaks. In addition, the following people made life in Austin easy to get through: Wanyoung, Jonghyuk, Jinwook, Yunphil, Bonggu, Junho, Sungyeun, Hoyoung, Suyong, Byungick, Hongki, Juhyung, Jusang, Insun, Jaekwang, Yongsup, Wooseok, Jeongdae, Jiseon. I will remember your names.

Lastly, I should thank my wife, Meejung, and my daughter, Jeenah, who give me a reason to live. I also need to say thank you my mother and grandmother in my hometown, Taegu, for their prayers, and Meejung's parents in Suwon for their support. Especially, I want to thank Meejung's eldest sister, Guijin Park, and her husband, Kangil Lee for their support.

All I have achieved in Austin is due to these good people around me. Thank you all.

Magnetic Phase Diagram of $\text{Ca}_{2+x}\text{Y}_{2-x}\text{Cu}_5\text{O}_{10-\delta}$: Oxygen Hole-Doping Effects

Publication No. _____

Keeseong Park, Ph.D.
The University of Texas at Austin, 2007

Supervisor: John T. Markert

Oxygen hole-doping effects on a spin-chain system, $\text{Ca}_{2+x}\text{Y}_{2-x}\text{Cu}_5\text{O}_{10-\delta}$ (CaYCuO) are reported. CaYCuO is a good specimen to study the magnetic properties of the CuO_2 chain at the ground state because it has no complex structure other than the chain and it has hole dopability up to the formal copper valence number of +2.4. Specifically, we can dope holes into the CuO_2 chain by substituting Ca^{2+} for Y^{3+} or by utilizing oxygen deficiency. After a systematic study of the two methods to dope holes, we found that oxygen doping makes a more critical change in magnetic ordering in the chain than the replacement of Ca^{2+} . Oxygen deficiency effects of the chain on the magnetic properties were explained using a mean field theory. A new relation for the effective hole doping was found as $p = x - a\delta$, where $a = 3/2(x - \delta) - 1/4$, and the linear equation, $p = x - (2/3)\delta$. We study the anisotropy of magnetic properties of single crystal Li-cathode material (LiFePO_4) for g-factor, Curie-Weiss

temperature, and effective moment. Magnetic properties Au/SiO₂ coated γ -Fe₂O₃ are compared with pure γ -Fe₂O₃ finding a decrease in the blocking temperature and the irreversible temperature for the coated nanoparticles.

Table of Contents

Acknowledgments	v
Abstract	vii
List of Tables	xi
List of Figures	xii
Chapter 1. Introduction	1
Chapter 2. Theory and Background	3
2.1 Basics of magnetism	3
2.2 $\text{Ca}_{2+x}\text{Y}_{2-x}\text{Cu}_5\text{O}_{10-\delta}$	9
2.3 Oxygen deficiency in cuprates	25
Chapter 3. Experiments	31
3.1 Sample Preparation	31
3.2 Sample Analysis	33
3.2.1 X-ray Diffraction [103]	34
3.2.2 Iodometric Titration	36
3.3 Magnetic Properties	38
3.4 Heat Capacity	40
3.4.1 Review of Measurement Techniques	40
3.4.2 Semi-adiabatic calorimetry	44
3.4.3 Data Acquisition	49

Chapter 4. Fe magnetism in single-crystal LiFePO_4 and in Fe_2O_3 nanoparticles	52
4.1 Anisotropy in the magnetic properties of single crystal LiFePO_4	52
4.1.1 Background	52
4.1.2 Results and Discussion	55
4.2 Effects of Au/Silica double coating on the properties of Fe_2O_3 magnetic nanoparticles	65
4.2.1 Background	65
4.2.2 Results and Discussion	69
Chapter 5. Results and Discussion of $\text{Ca}_{2+x}\text{Y}_{2-x}\text{Cu}_5\text{O}_{10-\delta}$	80
5.1 Sample analysis	80
5.1.1 x-ray diffraction	80
5.1.2 Iodometric titration	84
5.2 Magnetic susceptibility	85
5.3 Specific heat	93
5.4 Discussion	97
Chapter 6. Summary and Future work	105
Appendices	108
Appendix A. High Pressure Oxygen Furnace	109
Appendix B. Iodometric Titration[69]	112
B.1 Preparation of the solutions	113
B.2 Experimental Procedures	115
B.2.1 Calculations, etc.	117
Appendix C. Derivation of the Magnetic Susceptibilities in anisotropic systems	120
C.1 Magnetic field applied parallel to the z-axis	120
C.2 Magnetic field applied perpendicular to the z-axis	122
Bibliography	125
Vita	137

List of Tables

2.1	Absence (O) or presence (X) of a long-range phase transition at a finite temperature for various magnetic systems [23]	10
4.1	Néel temperature and fitting parameters from the Curie-Weiss law for LiFePO_4 . Here the Curie constant C has units (emu K/mole).	62
5.1	Titration results for $\text{Ca}_{2+x}\text{Y}_{2-x}\text{Cu}_5\text{O}_{10-\delta}$	85
5.2	Magnetic parameters of $\text{Ca}_{2+x}\text{Y}_{2-x}\text{Cu}_5\text{O}_{10-\delta}$ including Néel temperature, effective magnetic moment, and the Curie-Weiss temperature.	89

List of Figures

2.1	Magnetic specific heats of Ising (left) of Heisenberg (right) model with the calculation performed using the mean field theory[24]	8
2.2	Geometric view of edge-sharing and corner-sharing cuprates . . .	11
2.3	Phase diagrams for the CaO-Y ₂ O ₃ -CuO systems at 1000°C [22]	12
2.4	Powder x-ray diffraction pattern of CaYCuO. Incommensurate superstructure peaks shaded [22]	13
2.5	Structure of Ca _{2+x} Y _{2-x} Cu ₅ O _{10-δ} for $x = 2$	14
2.6	Temperature dependence of magnetic susceptibility and resistance of CaYCuO [39]	15
2.7	NMR lineshape and relaxation times of ⁸⁹ Y in CaYCuO at various temperatures. [13]	17
2.8	Thermal conductivity of CaYCuO	19
2.9	Lattice parameters of single crystal CaYCuO [61]. Open and closed circles represent data of the single crystal and powder sample [39], respectively	20
2.10	Magnetic susceptibility and specific heat of single crystal CaYCuO [61].	22
2.11	Magnetic phase diagram of single crystal CaYCuO [61].	24
2.12	Variation in resistivity of LSMO single crystals [93].	27
3.1	Baking profiles in three different furnaces	32
3.2	Three methods of low temperature calorimetry	42
3.3	The base and addenda of the semi-adiabatic calorimeter.	45
3.4	Schematic diagram and electronic setup for calorimetry.	47
3.5	Raw data and exponential fitting to find temperature deviation	48
3.6	Heat capacities of the sum of addenda and samples (dots), and addenda only (crosses)	50
4.1	Baking profile of LiFePO ₄ by using a flux method	53
4.2	Structure diagram of LiFePO ₄ (left) and magnetic interaction of Fe ²⁺ ions (right).	54

4.3	X-ray pattern of ground single crystal LiFePO_4	55
4.4	Magnetic susceptibilities of single crystal LiFePO_4 along each axis with average susceptibility. Inset (a) shows the enlarged transition temperature region. Inset (b) shows $d(\chi T)/dT$ versus temperature noting the exact Néel temperature.	57
4.5	The inverse susceptibility (χ^{-1}) versus temperature along fitted to Curie-Weiss law. The inset shows the average of the magnetic susceptibilities of all axes with the polycrystal data [90].	61
4.6	Field dependence of magnetization of each axis for different temperatures (a)-(c), and hysteresis of each axis at 5 K and 35 K (d)	64
4.7	(a) Typical TEM image of Au/SiO_2 doubly coated $\gamma\text{-Fe}_2\text{O}_3$ nanoparticles. (b) Enlarged image of the rectangular area in the upper silica sphere shown by the white dashed loop.	67
4.8	Background data of magnetic susceptibility measurements. M-T graph at the top, M-H graphs at the middle and the raw data from the Au/SiO_2 coated $\gamma\text{-Fe}_2\text{O}_3$ at the bottom.	70
4.9	Field cooling (FC) and zero-field-cooling (ZFC) of magnetization graph for the pure $\gamma\text{-Fe}_2\text{O}_3$ with 10 Oe and 500 Oe, for the SiO_2 coated $\gamma\text{-Fe}_2\text{O}_3$ with 500 Oe, and for Au/SiO_2 coated $\gamma\text{-Fe}_2\text{O}_3$ with 500 Oe. The blocking temperature are expressed as an arrow.	73
4.10	Field dependence of magnetization of pure and Au/SiO_2 coated $\gamma\text{-Fe}_2\text{O}_3$ at various temperatures.	75
4.11	Field dependence of magnetization of pure and Au/SiO_2 coated $\gamma\text{-Fe}_2\text{O}_3$ at various temperatures.	76
4.12	Coercivity versus Temperature ^{1/2} for pure and coated NPs. The solid and dotted line shows fits with Equ. 4.30.	78
5.1	X-ray diffraction patterns of $\text{Ca}_{2+x}\text{Y}_{2-x}\text{Cu}_5\text{O}_{10-\delta}$ for $x = 0, 0.75$ and 1.0, for different oxygen annealing procedures. The raw data for $x = 0$ and 0.75, and the data after a smooth background subtraction for $x = 1.0$. The impurity signal from $\text{Cu}_2\text{Y}_2\text{O}_5$ is marked with circles.	81
5.2	X-ray diffraction patterns of $x = 1.25$ and 1.5 for different oxygen annealing procedures.	83
5.3	Dependence of lattice parameters on Ca-doping and oxygen deficiency.	84
5.4	Temperature dependence of magnetic susceptibility for all samples	86

5.5	Magnetic susceptibilities and their enlargements of $x = 1.25$ and 1.5 samples with different oxygen annealing pressures.	88
5.6	Inverse of magnetic susceptibility versus temperature for the fully oxygenated samples. Solid lines are from the fitting with Curie-Weiss law above 75 K.	90
5.7	Effective magnetic moments and the Curie-Weiss temperatures using Eq. 5.1 at different temperature ranges. The data connected with the solid lines are from fully oxygenated samples. The data from oxygen deficient samples are connected by dotted lines.	92
5.8	Temperature dependence of the specific heat of CaYCuO for different oxygen deficiencies. The last figure shows C/T versus T^2 of $x = 0.9, 1.0$ and 1.25	94
5.9	Specific heat of two contributions, phonon and spin. The red line in the first graph shows the phonon contribution. The second graph shows the spin contribution with fits using dimer, Ising, and Heisenberg chain models. The last graph shows Quantum Monte Carlo simulation results for the dimensional transition from 3D to 2D of specific heat where $\alpha = J_{\perp}/J_{plane}$ [91]	96
5.10	Magnetic phase diagram where hole doping dependence considers both Ca-doping and oxygen deficiency. Single crystal data from prior experiment [61].	98
5.11	Néel temperature, Curie-Weiss temperature, and effective magnetic moments of CaYCuO. The last figure shows the oxygen deficiency dependence of Néel temperature for each hole doping.	100
5.12	Phase diagram with different hole doping relations	102
5.13	Phase diagram with different relations for hole doping, cation doping and oxygen deficiency	104

Chapter 1

Introduction

Low dimensional cuprate spin systems have attracted much attention because they are the key to understanding high-temperature superconductivity, and a playground to study fundamental physics of spin interactions. $\text{Ca}_{2+x}\text{Y}_{2-x}\text{Cu}_5\text{O}_{10-\delta}$ (CaYCuO) is an interesting quasi one-dimensional system because it only has a CuO_2 chain structure which makes the analysis simple; and it is hole-dopable up to the formal copper valence of +2.4. Moreover, calcium doping and oxygen deficiency have been shown to create hole-doping, making available the direct comparison of the effects of Ca-doping and oxygen deficiency on the properties of CaYCuO.

Oxygen has played an important role in cuprate superconductors and manganite giant magnetoresistants (GMR), but many studies are complicated by multiple oxygen sites, for example, the plane and chain site, in $\text{YBa}_2\text{Cu}_3\text{O}_{7-\delta}$ or the chain and ladder sites in $\text{Ca}_{14}\text{Cu}_{24}\text{O}_{41}$. Our oxygen deficiency study of the more ideal CaYCuO is a good starting point to further understand the role of oxygen in for cuprate spin chain systems, since only a single type of oxygen site (on-chain) is present.

We made CaYCuO compounds with various calcium-doping and oxy-

gen deficiency. After confirming their single phase and chemical stoichiometry using x-ray powder diffraction and iodometric titration, magnetic susceptibility and heat capacity were measured to study the dependence of their magnetic properties dependent on hole doping. During these experiments, oxygen effects were investigated systematically on the structural and magnetic properties of CaYCuO. Especially the dependence of the Néel temperature on hole doping was examined for both calcium-doping and oxygen deficiency. Oxygen deficiency was found to be more influential in changing magnetic interactions.

In separate studies, the anisotropy of the magnetic properties of the single crystal Li-cathode material LiFePO₄ was measured to determine the g-factor, the Curie-Weiss temperature, and the effective Fe moment. We explain these anisotropies with a mean-field theory. Also, magnetic properties of Au/SiO₂ coated γ -Fe₂O₃ nanoparticles were compared with pure γ -Fe₂O₃ nanoparticles. A decrease in the blocking temperature and the irreversible temperature was found for the coated sample.

Chapter 2

Theory and Background

2.1 Basics of magnetism

This section basically follows 'Quantum theory of magnetism' by Robert White [114]. Magnetic properties of solids, including cuprates, are derived from the electrons in the materials. The electron's intrinsic magnetic moment can not be explained by classical mechanics. Therefore let's use quantum mechanics and start with a Hamiltonian describing the motion of electrons. The general wave equation is given by

$$i\hbar \frac{\partial \psi(\mathbf{r}, t)}{\partial t} = H\psi(\mathbf{r}, t). \quad (2.1)$$

Considering the relativistic symmetry of time and space, we need a linear space derivative so we get the Dirac expression

$$H = c\boldsymbol{\alpha} \cdot \mathbf{p} + \beta mc^2 \quad (2.2)$$

where c is the speed of light, α and β are arbitrary coefficients, $\mathbf{p} = -i\hbar\nabla$ is the momentum of electron and m is the rest mass of electron. To satisfy the correct energy-momentum relation $E^2 = p^2c^2 + m^2c^4$, α and β should be, by the 4×4 representation,

$$\alpha = \begin{pmatrix} 0 & \sigma \\ \sigma & 0 \end{pmatrix} \text{ and } \beta = \begin{pmatrix} \mathbf{1} & 0 \\ 0 & \mathbf{1} \end{pmatrix},$$

where σ is the Pauli matrix

$$\sigma_x = \begin{pmatrix} 0 & 1 \\ 1 & 0 \end{pmatrix}, \sigma_y = \begin{pmatrix} 0 & -i \\ i & 0 \end{pmatrix}, \sigma_z = \begin{pmatrix} 1 & 0 \\ 0 & -1 \end{pmatrix}, \mathbf{1} = \begin{pmatrix} 1 & 0 \\ 0 & 1 \end{pmatrix}.$$

The wave function ψ has four components. Two of them have positive energy, which is for electrons, and the others are negative, which is for positrons or holes. We may add the effect of an external electromagnetic field with vector and scalar potentials \mathbf{A} and ϕ . Then the Dirac equation becomes

$$i\hbar \frac{\partial \psi(\mathbf{r}, t)}{\partial t} = [c\boldsymbol{\alpha} \cdot (\mathbf{p} - \frac{e}{c}\mathbf{A}) + \beta mc^2 + e\phi]\psi(\mathbf{r}, t). \quad (2.3)$$

Now if we consider the positive energy terms, the Hamiltonian is given by

$$H = [mc^2 + \frac{1}{2m}(\mathbf{p} - \frac{e}{c}\mathbf{A})^2 - \frac{p^4}{8m^3c^2}] + e\phi - \frac{e\hbar}{2mc}\boldsymbol{\sigma} \cdot \mathbf{H} - i\frac{e\hbar^2}{8m^2c^2}\boldsymbol{\sigma} \cdot \nabla \times \mathbf{E} - \frac{e\hbar}{4m^2c^2}\boldsymbol{\sigma} \cdot \mathbf{E} \times \mathbf{p} - \frac{e\hbar^2}{8m^2c^2}\nabla \cdot \mathbf{E}. \quad (2.4)$$

The first term in the second line shows the interaction of electron spins with an external magnetic field \mathbf{H} , the next two terms come from spin-orbit coupling and the last term, which is called the Darwin term, represents the correction to the Coulomb interaction due to electron's fluctuations from the effects of negative-energy component in the wave function [114]. If we imagine that the vector potential stationary ($\nabla \times \mathbf{E} = 0$) and the scalar potential $V(r)$ is spherically symmetric, then we obtain

$$\boldsymbol{\sigma} \cdot \mathbf{E} \times \mathbf{p} = -\frac{1}{r}\frac{\partial V}{\partial r}\boldsymbol{\sigma} \cdot \mathbf{r} \times \mathbf{p} = -\frac{1}{r}\frac{\partial V}{\partial r}\boldsymbol{\sigma} \cdot \mathbf{l},$$

where $\hbar\mathbf{l} = \mathbf{r} \times \mathbf{p}$. Now considering the $p^4/8m^3c^2$ and the Darwin term to be small, and defining the zero of energy as the rest-mass energy, the Hamiltonian

for the motion of electrons[114] is

$$H = \frac{1}{2m}(\mathbf{p} - \frac{e}{c}\mathbf{A})^2 + e\phi - \frac{e\hbar}{2mc}\boldsymbol{\sigma} \cdot \mathbf{H} + \zeta\mathbf{l} \cdot \boldsymbol{\sigma}, \quad (2.5)$$

where the spin-orbit parameter is

$$\zeta = \frac{e\hbar^2}{4m^2c^2} \frac{1}{r} \frac{\partial V}{\partial r}.$$

For the vector and the scalar potentials, we may think of several sources including the uniform external field, the electric quadrupole field, the magnetic dipole (hyperfine) field which is from the electron-nucleus magnetic coupling, the fields from other electrons on the same ion, crystalline electric fields, the fields from interactions between an ion and its surrounding magnetic neighbors, which is called dipole-dipole interaction, direct exchange, superexchange, double exchange, RKKY exchange, etc. Direct exchange is from the direct overlap of two wavefunctions of electrons within an atom or of adjacent atoms. Indirect exchange needs intermediaries, which could be diamagnetic atoms for superexchange and for double exchange. RKKY exchange is from the surrounding conduction electrons [101].

We usually choose only the most important terms for each case out of the above Hamiltonian because it is so general and not easy to find solutions. Transition-metal ions including Cu^{2+} have the magnetic electrons in the outermost d shell of the ions contrary to rare-earth ions which have unpaired electrons inside the $6s^2$ shells. So the $3d$ electrons can easily participate in the interaction with the ligands and overlap with the oxygen $2p$ orbitals. It means

the crystalline field interaction is important. But the spin-orbit interaction is not strong because the electrons lie relatively far from the center of the ions compared to rare-earth ions. Therefore we may write down the effective Hamiltonian as, in order of descending strength,

$$H = H_{intra-atomic\ Coulomb} + H_{crystal\ field} + H_{spin-orbit} + H_{Zeeman}. \quad (2.6)$$

The intra-atomic Coulomb interaction gives the spectroscopic energy level, whose lowest energy sub-level can be determined by Hund's rule; for example, the lowest energy level of Cu^{2+} , $3d^9$, is ${}^2D_{\frac{5}{2}}$. And the lowest level is enough to explain magnetic properties because the spectroscopic energy is on the order of a few eV, but the magnetic energy is on the order of a few meV. The crystal field Hamiltonian reduces the degeneracy of the lowest spectroscopic level state. With the help of group theory, we find the degenerate d states are split into t_2 and e states [17]. That is, the ground state of the Cu^{2+} ion is from Hund's rules

$$|L, M_L; S, M_S \rangle = |2, M_L; \frac{1}{2}, M_S \rangle, \quad (2.7)$$

which is $(2L + 1)(2S + 1) = 10$ -fold degenerate. Adding the crystal field, the ground state would be $|\Gamma, \gamma; S, M_S \rangle = |t_2, \gamma; \frac{1}{2}, M_S \rangle$, where Γ is the irreducible representation of the point-group symmetry.

For a given spin state, we may calculate the spin-orbit and Zeeman energy term by using perturbation theory based on the orbital ground state, $|\Gamma, \gamma \rangle$. This is because the orbital and spin states are not mixed due to either the inter-atomic or the crystal field, so we may separate the state into a

product of two states, $|\Gamma, \gamma; S, M_S\rangle = |\Gamma, \gamma\rangle |S, M_S\rangle$. So the expectation value of $H_{spin-orbit} + H_{Zeeman}$ is, in first order perturbation,

$$H_{eff} = H_{spin-orbit} + H_{Zeeman} \quad (2.8)$$

$$= \lambda \mathbf{L} \cdot \mathbf{S} + \mu_B (\mathbf{L} + 2\mathbf{S}) \cdot \mathbf{H} \quad (2.9)$$

$$= 2\mu_B \mathbf{H} \cdot \mathbf{S} - \sum_{\Gamma', \gamma'} \frac{|\langle \Gamma', \gamma' | \mu_B \mathbf{H} \cdot \mathbf{L} + \lambda \mathbf{L} \cdot \mathbf{S} | \Gamma, \gamma \rangle|^2}{E_{\Gamma', \gamma'} - E_{\Gamma, \gamma}} \quad (2.10)$$

$$= \sum_{\mu, \nu} (\mu_B g_{\mu\nu} H_\mu S_\nu - \lambda^2 A_{\mu\nu} S_\mu S_\nu - \mu_B^2 \Lambda_{\mu\nu} H_\mu H_\nu). \quad (2.11)$$

Here $g_{\mu\nu}$ is the g tensor,

$$g_{\mu\nu} = 2(\delta_{\mu\nu} - \lambda \Lambda_{\mu\nu}) \quad (2.12)$$

$$\Lambda_{\mu\nu} = \sum_{\Gamma', \gamma'} \frac{\langle \Gamma, \gamma | L_\mu | \Gamma', \gamma' \rangle \langle \Gamma', \gamma' | L_\nu | \Gamma, \gamma \rangle}{E_{\Gamma', \gamma'} - E_{\Gamma, \gamma}}. \quad (2.13)$$

These equations will be used to explain the magnetic anisotropy of LiFePO₄.

The Coulomb interaction between the valence electrons on different ions can be expressed as an effective interaction between the individual electron spins. Many systems can be explained by this interaction expressed in the spin states, called the Heisenberg exchange Hamiltonian, whose general form for the ground spin state of the same ions is

$$H_{ex} = -2 \sum_{i < j} (J_x S_{ix} S_{jx} + J_y S_{iy} S_{jy} + J_z S_{iz} S_{jz}) - D \sum_i S_{iz}^2 \quad (2.14)$$

where the second term shows anisotropy from the crystal-field term called Dzialoshinski-Moriya exchange [23]. For $D \rightarrow \infty$, the moments are forced to lie along to the z-axis, which makes the system behave like the 1D Ising model,

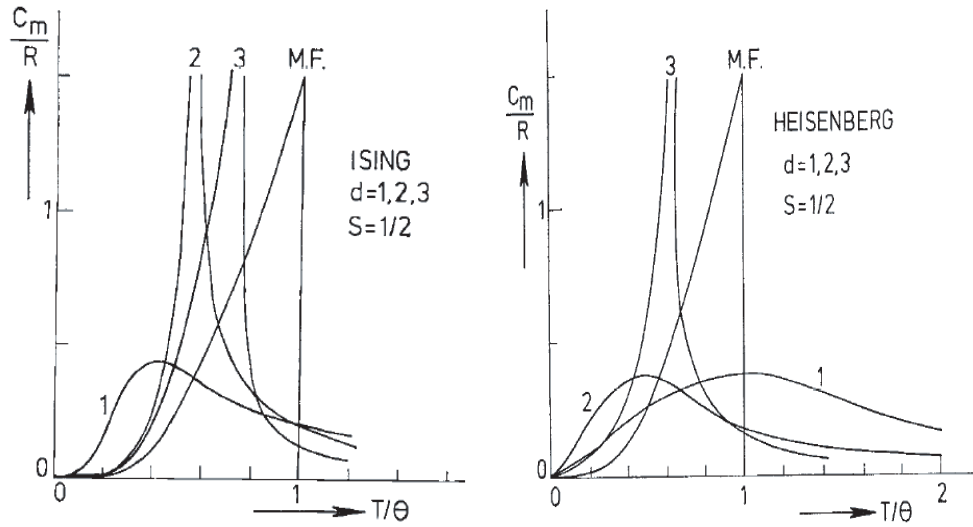


Figure 2.1: Magnetic specific heats of Ising (left) of Heisenberg (right) model with the calculation performed using the mean field theory[24]

and for $D \rightarrow -\infty$, the moments lies perpendicular to the z-axis, which makes the system 2D planar or XY type.

From the Hamiltonian, we may calculate the partition function Z and the free energy $F = -kT \ln Z$, which enables us to find all physical quantities. That is, the magnetic energy U_m , the entropy S and the magnetization M_T are the first derivatives of the free energy. And the specific heat C and the magnetic susceptibility χ are its second derivatives.

$$\begin{aligned}
 U_m &= \langle H \rangle = -\frac{\partial \ln Z}{\partial (kT)^{-1}}; & S &= -\frac{\partial F}{\partial T}; & M &= -\frac{\partial F}{\partial H} \\
 C &= \frac{\partial U}{\partial T} = -T \frac{\partial S}{\partial T} = -T \frac{\partial^2 F}{\partial T^2} \\
 \chi &= \frac{\partial M}{\partial H} = -\frac{\partial^2 F}{\partial H^2}.
 \end{aligned}$$

However, only 1D and 2D Ising models have exact solutions. The other models should be calculated numerically or approximately [24]. Figure 2.1 represents the magnetic specific heats of all models. From these figures, we find the phase transition occurs for the 2D and 3D Ising models and the 3D Heisenberg model. The phase transition on each model is summarized in Table 2.1. For example, mean field theory, one approximate method, gives the partition function for spin $S = \frac{1}{2}$ as

$$Z = 2\cosh(g\mu_B H_{MF}/2kT) \quad (2.15)$$

where the mean field $H_{MF} = 2nJ \langle S_z \rangle / g\mu_B = \lambda M_s$, n is the number of nearest neighbors, $\lambda = 2nJ/g^2\mu_B^2$ is the molecular field parameter, and $M_s = g\mu_B \langle S_z \rangle$ is the spontaneous magnetization per spin [23]. The Curie - Weiss constant from this theory is $\theta = 2zJS(S + 1)/3k$ [10] which will be used to explain the Néel temperature of the data.

2.2 $\text{Ca}_{2+x}\text{Y}_{2-x}\text{Cu}_5\text{O}_{10-\delta}$

Low dimensional spin systems have attracted a great deal of attention because they are excellent models for linking experimental and theoretical studies of spin and charge dynamics. Moreover the low dimension cuprate systems have been a main topic in condensed matter physics since the discovery of high - T_c superconductivity in cuprate materials. Cuprate chain systems can be categorized into two groups according to their geometrical alignment, see Fig. 2.2. One is the corner-sharing chain where the copper-oxygen-copper

Table 2.1: Absence (O) or presence (X) of a long-range phase transition at a finite temperature for various magnetic systems [23]

model	interaction	d=1	d=2	d=3
Ising	J_x and $J_y = 0$	O	X	X
XY	$J_z = 0$	O	\otimes^1	X
Heisenberg	$J_x^2 + J_y^2 + J_z^2 \neq 0$	O	O	X

¹ No temperature below which an order-parameter, for example spontaneous magnetism, can be defined but there is a temperature where the susceptibility diverges in an exponential pattern.

At this temperature, termed the Kosterlitz-Thouless temperature, vortex-antivortex pairs are unbounded [59]

interaction has almost an 180° angle. Its ground state shows long range anti-ferromagnetic order, and high T_c superconductors possess the same structure in a 2 dimensional plane. Ca_2CuO_3 , La_2CuO , Sr_2CuO_3 and SrCuO_2 are examples of this type. The other group is the edge-sharing chain which shows around 90° copper-oxygen-copper coupling. The super-exchange interaction of the edge-sharing chain critically depends on the Cu-O-Cu bonding angle [33, 74]. This group has been more attractive than the corner-sharing one because it has diverse magnetic ground states including spin-Peierls phase in CuGeO_3 [75], spin-charge separation [1], spin gap [62], superconductivity under high pressure [110] in a spin ladder system $\text{Sr}_{14-x}\text{Ca}_x\text{Cu}_{24}\text{O}_{41+y}$, extended magnetic moment formation in Li_2CuO_2 [112], and Wigner crystallization in $\text{Na}_{1+x}\text{CuO}_2$ [46].

$\text{Ca}_{0.8}\text{CuO}_2$, the $x = 2$ limit material of the $\text{Ca}_{2+x}\text{Y}_{2-x}\text{Cu}_5\text{O}_{10-\delta}$ (CaY-

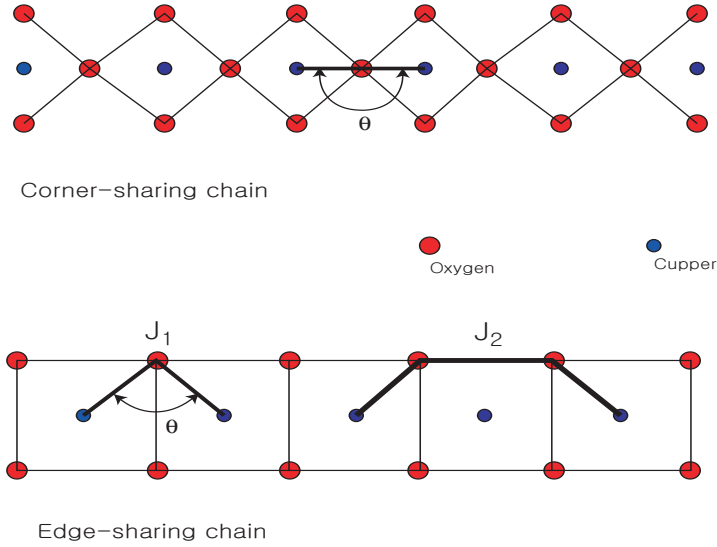


Figure 2.2: Geometric view of edge-sharing and corner-sharing cuprates

CuO) family, was reported to be stable at 750°C in one of the enormous trials to find the high T_c superconducting phase right after the discovery of cuprate superconductors [94], which is isostructural with NaCuO_2 consisting of one-dimensional chains of edge-sharing square planes linked by Na ions in an octahedral coordination. After a series of studies following the phase diagram (see the Fig. 2.3), Davies [21, 22] published the fabrication and the structural study of new phases including CaYCuO at 1000°C . The reported system was for $0 \leq x \leq 0.8$; x-ray diffraction data shows this system has an orthorhombic unit cell, and space group $Fmmm$. The lattice parameters for $x = 0$, $a = 2.817 \text{ \AA}$, $b = 6.185 \text{ \AA}$, $c = 10.594 \text{ \AA}$ and $V = 184.63 \text{ \AA}^3$. Figure 2.4 shows the powder diffraction data of CaYCuO where the shaded peaks are

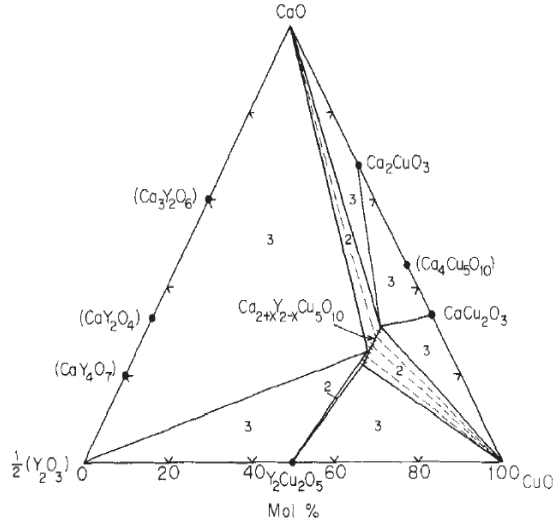


Figure 2.3: Phase diagrams for the CaO-Y₂O₃-CuO systems at 1000°C [22]

from incommensurate superstructures. That is because, contrary to NaCuO₂ whose available locations are occupied with Na, CaYCuO shows an incommensurate relationship between Ca/Y chain repeat distance and the Cu chain one. With Ca doping, the positions of the reflections corresponding to the orthorhombic subcell shifts to a lower angle which indicates a small increase in the size of the cell as the larger Ca ions are replaced for Y, but the shaded peaks in Fig. 2.4 undergo a large and systematic variation. The schematic structure of CaYCuO for $x = 2$ is shown in Fig. 2.5 where Y and Ca ions randomly occupy the same sites. The dotted line shows a unit cell which shows the ratio Ca ions to Cu ions is incommensurately 4 to 5.

The whole range of doped samples of CaYCuO ($0 \leq x \leq 2$) was synthesized successfully with high-pressure oxygen annealing in 1998 by Hayashi

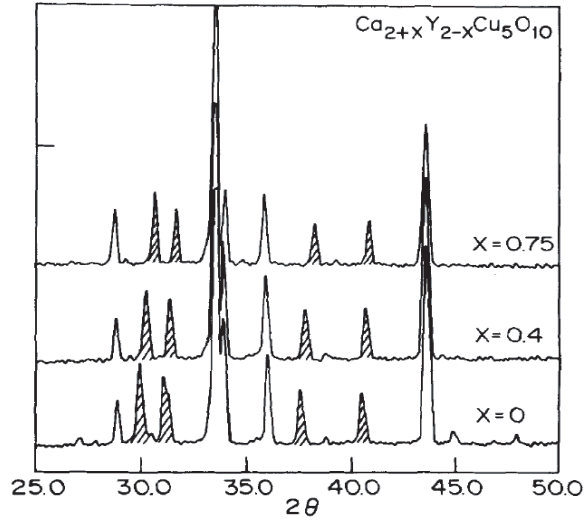


Figure 2.4: Powder x-ray diffraction pattern of CaYCuO . Incommensurate superstructure peaks shaded [22]

et al. [39]; this doping range allows the formal copper valences to change from 2.0 to 2.4. Thereafter these compounds have been revisited because of two big merits. One is that this system consists only of one-dimensional copper-oxygen chains without any other complex structures, such as ladders, which make analysis difficult. The other is this system is very hole-dopable not like many other spin-chain system including its isostructural compound NaCuO_2 . Replacing Ca^{2+} (1.0 Å) for Y^{3+} (0.9 Å), the variation of the subcell parameters in the solid solution is 1%, 2%, and 0.1% for the a , b , and c axes, respectively, as shown in Fig. 2.9. The increase along the b axis is due to the substitution of the larger ion (Ca) for the smaller ion (Y), and the decrease in a and c axes is because the effective hole doping decreasing the Cu-O-Cu bond length. The

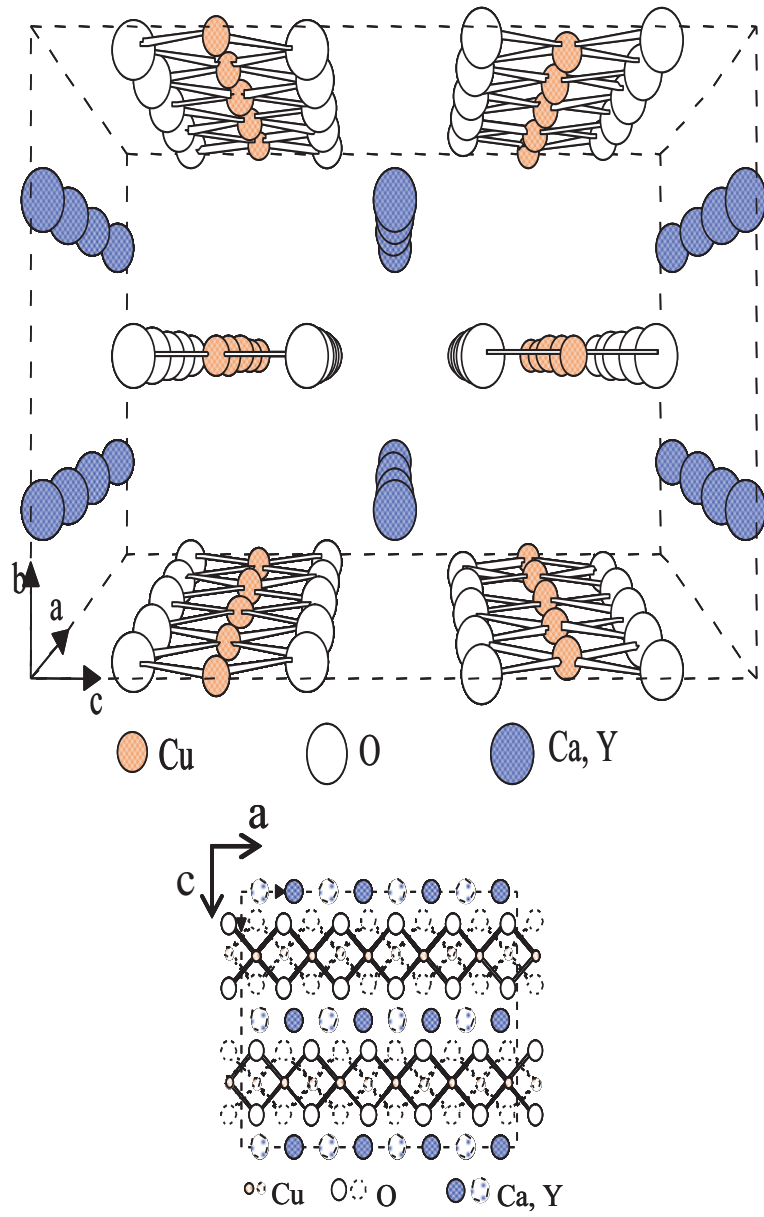


Figure 2.5: Structure of $\text{Ca}_{2+x}\text{Y}_{2-x}\text{Cu}_5\text{O}_{10-\delta}$ for $x = 2$

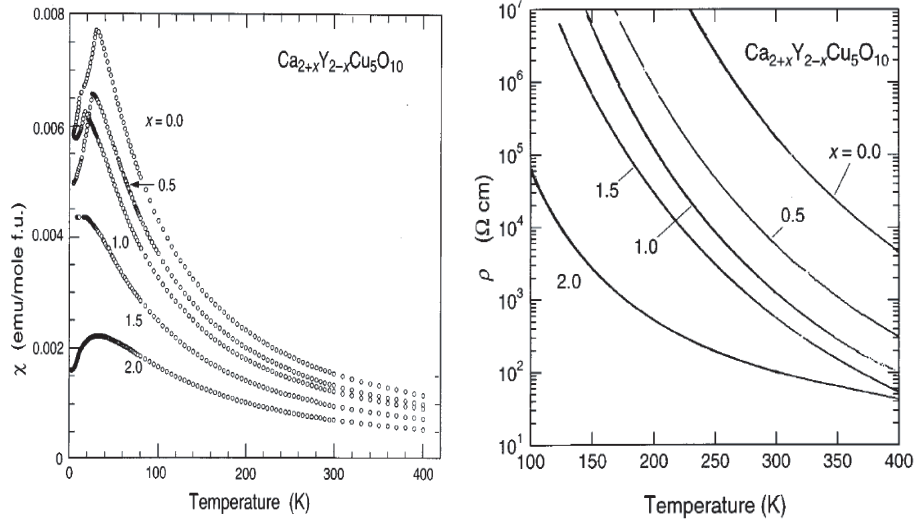


Figure 2.6: Temperature dependence of magnetic susceptibility and resistance of CaYCuO [39]

magnetic property of this system changes from long-range antiferromagnetic order to short-range order with increasing x as shown in the left side of Fig. 2.6. The holes induced with increasing Ca^{2+} content normally occupy the oxygen p orbital hybridized with the Cu d orbital. The spin from the hole in the oxygen orbital couples antiferromagnetically with the spin of the Cu ion, which makes the CuO_4 plaquette nonmagnetic (Zhang-Rice singlet [120]).

For $0 < x < 1$, the magnetic susceptibility data in Fig. 2.6 show a sharp cusp, which is typical of long-range order. As x increases, the Néel temperature decreases, with values of 28, 24, and 16 K for $x = 0, 0.5$, and 1, respectively. For above $x > 1.5$, the data shows broad maxima and its temperature T_{Max} increases with x increased up to 32 K for $x = 2$. The magnetic feature is

from the chain system with a high concentration of Zhang-Rice singlets, 4-5 of every ten CuO_4 plaquettes. Chabot *et al.* have proposed doping-induced magnetic dimensionality transitions based on these magnetic data [11]. That is, with an increasing concentration of doped holes, the magnetic behavior changes from 3D long-range order to 1D chain behavior and finally to cluster behavior. Even though doped holes induce enormous changes in magnetic ordering, the electric resistance doesn't change much. All samples in these system shows high resistivity and insulating features, that is, decreasing resistance with increasing temperature. The fully doped compound $\text{Ca}_4\text{Cu}_5\text{O}_{10}$ shows $\sim 40 \Omega\text{cm}$ which is about five orders of magnitude larger than that of metallic cuprates at similar doping levels. Long range antiferromagnetic order was confirmed at low temperature for the parent compound of $\text{Ca}_2\text{Y}_2\text{Cu}_5\text{O}_{10}$ by neutron powder diffraction where ferromagnetic intrachain alignment was revealed [29].

Figure 2.7 shows the NMR lineshape and relaxation times in the paramagnetic phase ($T > 250 \text{ K}$) [13]. Two or more large and broad peaks in the lineshape are evident, which is unusual in this region where a sharper and almost featureless resonance appears in many copper oxide compounds. This may be a result of the incommensurate structure between Ca/Y and CuO_2 chains. And the participation of Y ions in superexchange bridges between copper ions was proposed from the large shift ($\Delta H/H \approx 0.7\%$) and appreciable broadening ($\Delta\nu \approx 90 \text{ kHz}$) of the shape with temperature. The spin-lattice relaxation time (T_1) shows the minimum at $T = 275 \text{ K}$ where the spin-spin

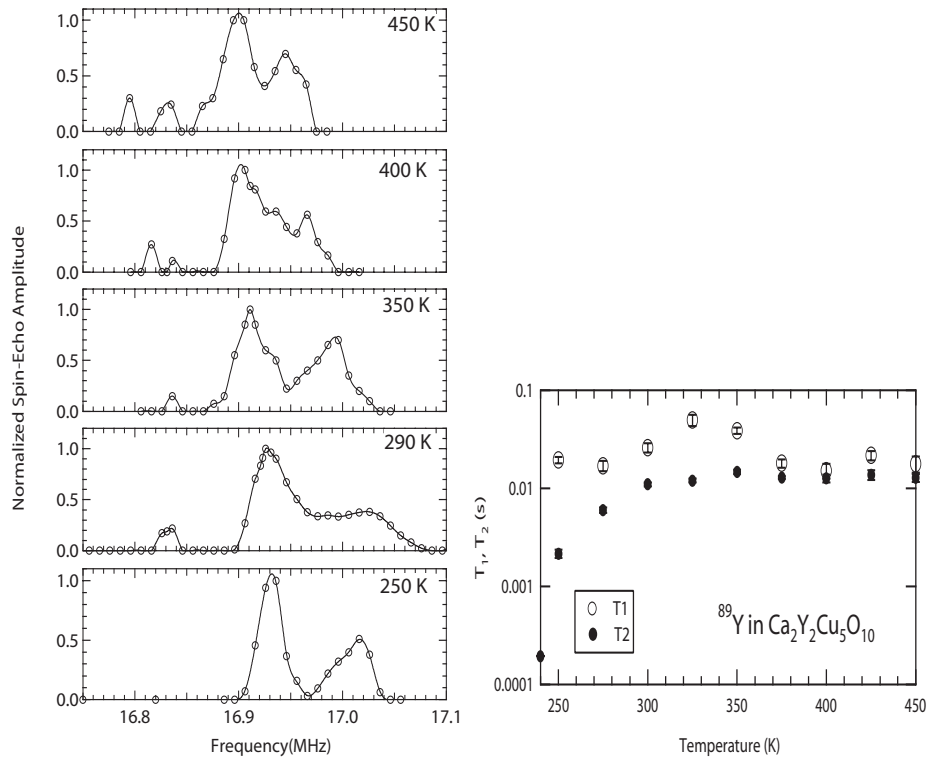


Figure 2.7: NMR lineshape and relaxation times of ^{89}Y in CaYCuO at various temperatures. [13]

relaxation time (T_2) start to decrease abruptly. The 100 times more shallow T_1 minimum than calculated for random Cu^{2+} dipolar fluctuations shows the existence of strong Cu^{2+} - Cu^{2+} spin correlations as well as proposed ^{89}Y - Cu^{2+} nuclear - electronic coupling. It is interesting to notice that this strong spin correlation exists far above the Néel temperature. The electronic correlation time at the T_1 minimum (275 K) is $\tau_e \approx 1/\omega_0 = 9.5 \times 10^{-9}$ s. And $\tau_e \approx 10^{-8}$ s at 235 K from T_2 . High frequency ESR measurements of the parent compound of CaYCuO were performed to confirm the long-range antiferromagnetic order and to find $g_{\parallel} = 2.31$ and $g_{\perp} = 2.03$ above 60 K [81]. And ESR data follows well antiferromagnetic resonance models of two-sublattices with an uniaxial anisotropy. The anisotropic field H_A is calculated to be 2.29 T and the exchange field H_E is 32.1 T. And also the spin-flop transition was expected at $H_c = 10.5$ T from $H_c = \sqrt{2H_A \cdot H_E}/(g/2)$.

Thermal conductivity measurements for the parent compound of CaYCuO shows two peaks, one sharp peak at 20 K and another broad peak around 90 K, as shown in Fig.2.8 [14]. This two-peak feature has appeared in low dimensional cuprates with strong intra-chain exchange coupling over 1000 K such as Sr_2CuO_3 ($J \approx 2650$ K) [96], SrCuO_2 ($J \approx 2500$ K) [98], or $\text{Sr}_{14}\text{Cu}_{24}\text{O}_{41}$ ($J \approx 1500$ K) [40, 93], or with spin-Peierls compounds such as CuGeO_3 ($J \approx 150$ K) [3]. Usually the low temperature peak is explained by ordinary phonon transport and the high temperature one is from magnetic excitations in an ordered ferromagnet, i.e., magnons [1]. Thus the observation of two peaks indicates that our ferromagnetic intrachain-coupled compound shows evidence

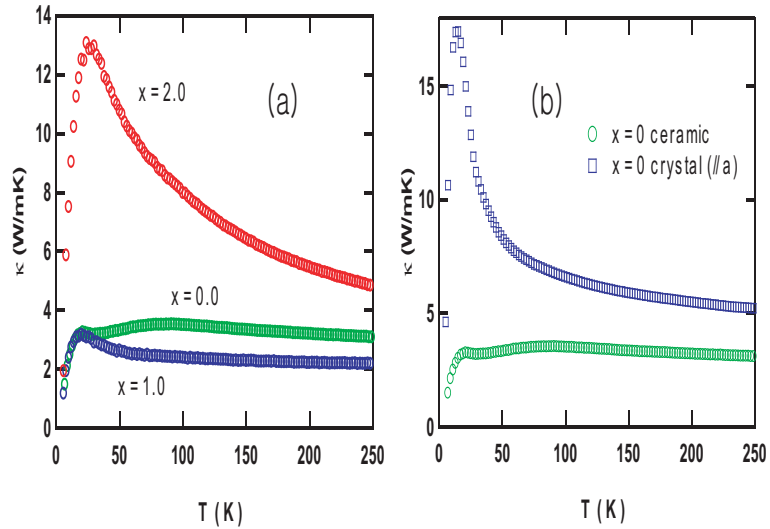


Figure 2.8: Thermal conductivity of CaYCuO

of magnon thermal transport. The high temperature peak is suppressed for $x = 1$ and $x = 2$ compounds, which is explained due to the strong scattering of magnons by induced holes. The enhanced thermal conductivity of the fully doped compound is due to the larger grain size of the compound. However the second peak is absent for a -axis data for a single crystal sample of the parent compound (Fig.2.8 b), which could indicate that the dispersion of magnons is in the the inter-chain direction, could be due to defect scattering of magnons (single crystals often contain more oxygen and other defects than polycrystal). This discrepancy is a good topic to study further.

After single crystals of CaYCuO were grown successfully by traveling-solvent floating-zone method in 2001 [61, 78], magnetic susceptibility and specific heat were measured with different Ca-doped samples to study the mag-

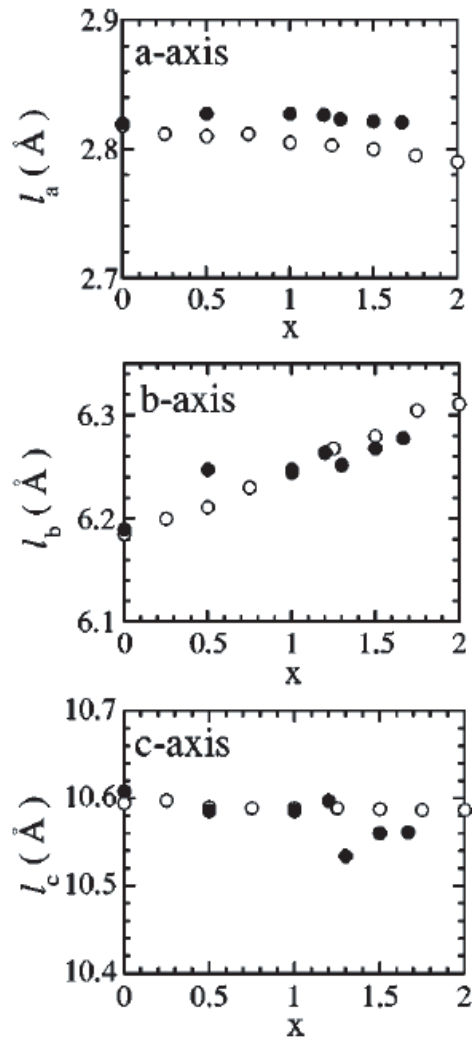


Figure 2.9: Lattice parameters of single crystal CaYCuO [61]. Open and closed circles represent data of the single crystal and powder sample [39], respectively

netic ground state in the edge-sharing CuO_2 chain [61]. CaYCuO series terminates in the fully Ca-doped compound $\text{Ca}_4\text{Cu}_5\text{O}_{10}$, and the similar compound $\text{Ca}_{1-x}\text{CuO}_2$ was proposed to show a coexistence of an antiferromagnetic order and a spin-gap state for $0.164 \leq x \leq 0.190$ [42]. This feature of $\text{Ca}_{1-x}\text{CuO}_2$ could be one example of an interesting spin state happening around the region where the Cu-O-Cu angle of the cuprate is between the ferromagnetic coupling (less than 95°) and the antiferromagnetic coupling (more than 95°) [75], because the angle of $\text{Ca}_{1-x}\text{CuO}_2$ (~ 93.27 [49]) is on the border of two different magnetic couplings. But the detailed scenario is not settled yet due to the difficulty in making single crystals of this compound. Therefore a study of CaYCuO is important because it enables us to test the coexistence of antiferromagnetic and spin gap states for CaYCuO whose Cu-O-Cu coupling angle is $\sim 91^\circ$ for $x = 0$ and $\sim 93.4^\circ$ for $x = 2$ [74]. And also due to the success in single crystal growth, all data from powder samples can be tested and confirmed.

As represented in Fig. 2.9, single crystal data shows the lattice parameter b is increasing with Ca doping, but a and c are slightly decreasing as for polycrystalline samples [39]. Figure 2.10 shows that the antiferromagnetic order CaYCuO has the b direction for its easy axis for $0 \leq x \leq 1.3$ at low temperature even though along the a and c axes, the magnetic susceptibility stay constant below the Néel temperature (T_N). For increasing Ca-doping, T_N decreases from 31, 29, 20, 15, and 12 K for $x = 0, 0.5, 1.0, 1.2,$ and 1.3 , respectively. For $x = 1.5$ and 1.67 , all axes show a small and broad shoulder

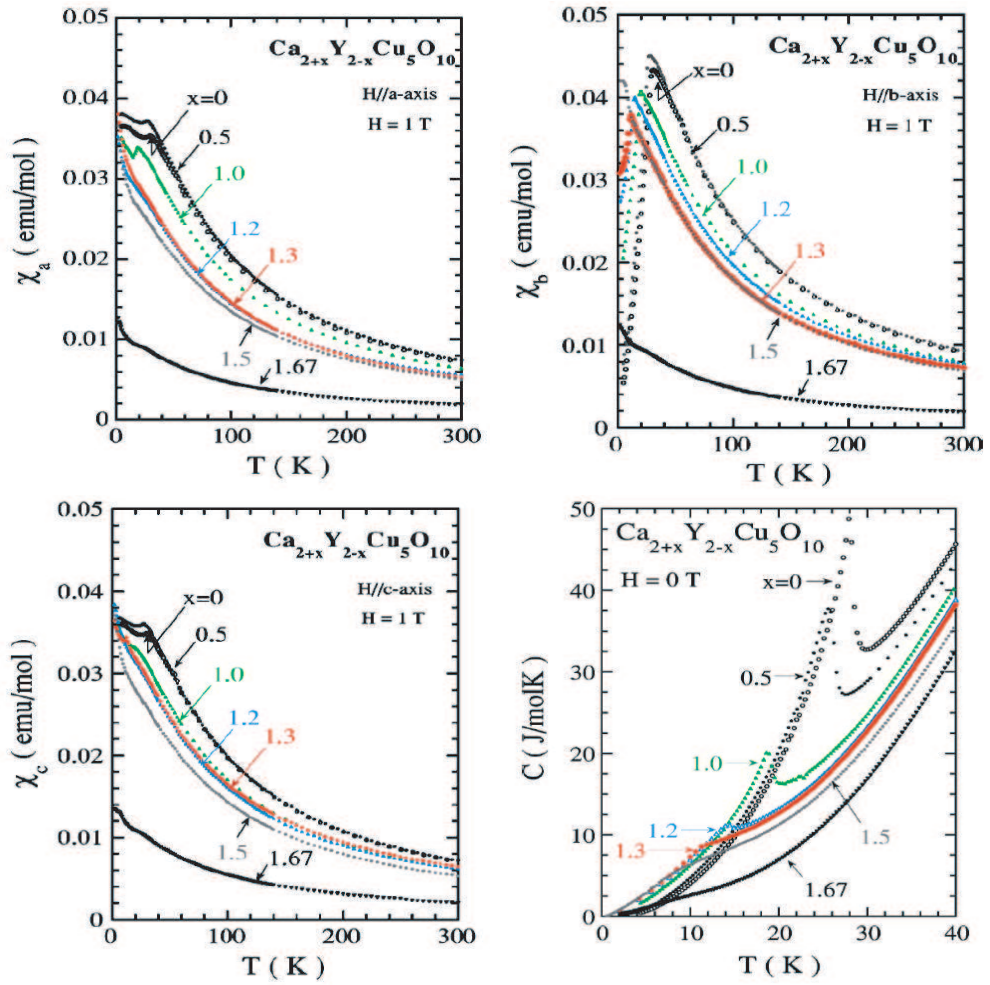


Figure 2.10: Magnetic susceptibility and specific heat of single crystal CaY-CuO [61].

which is not characteristic of antiferromagnetic order but instead of a spin-gap. And also a hysteresis in magnetic susceptibility is shown for $1.3 \leq x \leq 1.67$ indicating a possibility of a spin-glass state. The significantly small value of magnetic susceptibility at $x = 1.67$ was explained with the decrease of free spins per Cu to $1/3$ from 1 by making spin-singlets out of two Cu^{2+} spins located at the sides of the induced hole, which makes the next nearest coupling (J_2) antiferromagnetic, see Fig. 2.2. A λ -shaped peak is clear at $x = 0, 0.5, 1.0, 1.2$ and 1.3 which is characteristic of long-range antiferromagnetic order. This peak is smeared and shifted to the low temperature region with increasing hole doping. T_N is found from the peak to be 29, 26, 18, 15, and 12 K for the respective x numbers given above. For $x = 1.5$ and 1.67 , a broad peak was observed instead of the sharp λ -shaped peak, which was attributed to a short range-order similar to the spin-glass not from the spin gap state because the broad peak of $x = 1.67$ should be higher than that of $x = 1.5$ for spin gap, but it is not. The spin state for around $x = 1.6$ is considered a spin gap from the lowest peak of its specific heat data giving the minimum entropy consistent with the small number of free spins per Cu.

The left diagram of Fig. 2.11 shows the magnetic phase diagram of CaYCuO at zero field, as deduced from single-crystal data in ref. [61]. At low Ca-doping ($0 \leq x \leq 1.4$), CaYCuO is ordered in a long-range antiferromagnetic phase and the Néel temperature decreases with increasing x doping. Around $x = 1.5$, a spin-glass phase appears but the transition temperature is about 6 K regardless of the doping level. A spin gap shows up around

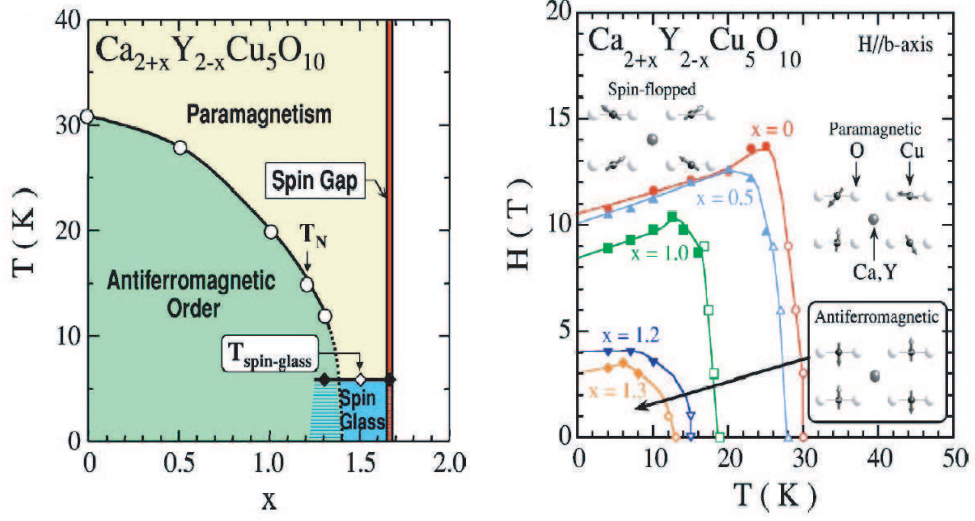


Figure 2.11: Magnetic phase diagram of single crystal CaYCuO [61].

$x = 1.6$ where more than half of the Cu ions build spin-singlet pairs. And at this spin-gap region, no evidence was found to explain the coexistence of an antiferromagnetic phase and the spin-gap phase contrary to the case of $\text{Ca}_{1-x}\text{CuO}_2$, even though the two compounds have similar hole concentrations and Cu-O-Cu angle ($\sim 93^\circ$). The intense modulation and the randomness of Ca/Y ions make holes move less and so they do not arrange suitably to form the phase coexistence. The right diagram of Fig. 2.11 shows the magnetic phase diagram of CaYCuO with $0 \leq x \leq 1.3$ as a function of magnetic field and temperature. The magnetic field is applied along the b -axis, and the typical spin arrangement along a is depicted, that is, along the CuO_2 chain. The spin-flop transition is observed below $x = 1.0$ along the easy axis (b), and its transition field is defined as the maximum point of the field derivative of

magnetization which is shown as a closed circle. And no spin-flop is found at $x = 1.2$ and 1.3 , and along the a and c axes.

Following a simple uniaxial mean-field model [118], the reason T_N decreases with increasing Ca-doping (or with increasing inducing holes) is not due to the decrease of J_1 (see Fig. 2.2) related to the exchange field (H_E) but to the decrease of the magnetic anisotropy along the b axis corresponding to the anisotropy field (H_A). This is because with changing x , H_E is constant as ~ 35 K but H_A is 1.6, 1.5, 1.0, 0.2, and 0.1 T for $x = 0, 0.5, 1.0, 1.2,$ and 1.3 , respectively. Neutron-scattering experiments confirm the ferromagnetic intra-chain coupling changes little with hole doping as well as temperature even though the interchain and anisotropic coupling are decreased [71]. And also the antiferromagnetic interchain interaction causes an anomalous broadening of spin-wave excitations along the chain for the parent compound CaYCuO [73]. These excitations were found to be softened and broadened with increasing temperature and hole-doping, regardless of Q (momentum) direction in the systematic neutron scattering experiments.

2.3 Oxygen deficiency in cuprates

Oxygen deficiency derives from vacant oxygen crystallographic lattice sites. This is because oxygen atoms associated with these sites are easily removed and reoccupied. Removal of oxygen changes the average copper valence and decreases the number of adjacent bonds. After finding high-temperature superconductivity in cuprates which are easily oxygen-deficient, the effects

of oxygen deficiency on the superconductivity has been a main topic in the physics of cuprates. The famous superconductor $\text{YBa}_2\text{Cu}_3\text{O}_{7-\delta}$ (YBCO) has been found to show superconductivity at 92 K for $\delta = 0$ but no superconductivity for $\delta = 0.6$. YBCO also makes a geometric transition from orthorhombic to tetragonal at $\delta = 0.6$ with increasing δ [86]. The critical dependence of superconductivity on oxygen deficiency has attracted a lot of attention and various high T_c cuprate compounds were fabricated to explore the effects of oxygen on other ions, or on the CuO plane.

$\text{RBa}_2\text{Cu}_3\text{O}_{7-\delta}$ (RBCO, R = rare earth) have two hole reservoirs; the superconducting CuO_2 plane and the metallic CuO chain. It is interesting to see how these planes and chains contribute to the physical properties of RBCO. Oxygen deficiency was used to separate these contributions [105]. The appropriate rare earth was chosen to optimize the hole doping concentration in the plane at the same for each experiment. In such optimal compounds, δ_{opt} increases with the mole fraction of rare earth, decreases with increasing rare-earth size, and is close to zero (≈ 0.02) at R = Nd [115]. The effects of oxygen vacancy in the CuO chain layer on the rare-earth ions' magnetic ordering and crystal symmetry in RBCO show their magnetic order changes from 3D long-range order to 2D short-range or other short range coupling [16].

Another famous superconducting cuprate, $\text{La}_{2-x}\text{Sr}_x\text{CuO}_{4-\delta}$ (LSCO) was also studied to observe the effect of oxygen deficiency on superconductivity [109]. High pressure annealing at different temperatures was used to obtain samples with different oxygen contents. From high frequency infrared

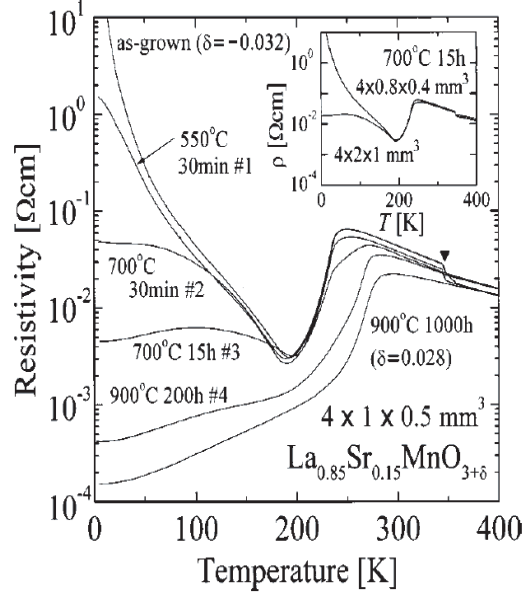


Figure 2.12: Variation in resistivity of LSMO single crystals [93].

spectrum 689 cm^{-1} studies [31], no oxygen vacancy was found for low Sr doped compounds because of the stability of the planar oxygen which is the vacant site in LSCO [87]. The oxygen vacancy starts to increase with increasing Sr content at $x \geq 0.2$. The 689 cm^{-1} peak disappears at low ($x \leq 0.15$) Sr-doping which is due to the screened effect of charge carriers in the CuO_2 plane. But oxygen vacancy makes Cu^{2+} localized, which cause the 689 cm^{-1} peak to reappear. Also the localized Cu^{2+} induced from oxygen deficiency was found to suppress the superconductivity in resistivity measurements [31]. In summary, the oxygen deficiency in LSCO causes an increase in resistivity, Curie constant, and reappearance of all the infrared bands at higher Sr doped compound ($0.5 \leq x \leq 1.20$) [99]. The similar compound $\text{La}_{2-x}\text{Sr}_x\text{MnO}_{4-\delta}$ (LSMO)

also shows a strong relation between oxygen deficiency and geometrical and electrical transitions [63, 89]. Around the metal-insulator transition range $x = 0.14 - 0.16$, increasing δ reduces the resistivity dramatically as shown in Fig. 2.12. A structural phase transition appears at $\delta < 0$ (solid triangle in the figure) and disappears at $\delta > 0$. And even from $\text{Bi}_2\text{Sr}_2\text{CaCu}_2\text{O}_{8-\delta}$ (BSCCO) [19], empirical expressions of the resistivity and thermoelectric power were suggested and their parameters on oxygen deficiency were claimed to be effective for other high T_c superconductors. That is, the resistivity $\rho(T) = \rho_0 T^a e^{\Delta/kT}$ and thermoelectric power $S(T) = A + BT$ where only A and Δ are sensitive to oxygen deficiency.

Oxygen reduction is necessary to create superconductivity in $\text{R}_{2-x}\text{Ce}_x\text{CuO}_4$ ($\text{R} = \text{Pr}, \text{Nd}, \text{Sm}, \text{Eu}$) where partially replacing the rare earth ions (R^{+3}) with Ce^{+4} induces electrons into the CuO_2 planes [108]. Oxygen annealing in a low pressure oxygen environment changes resistivity, the Hall effect and the Néel temperature. The role of oxygen vacancies in n-doped superconductors is explained in many different ways including decreasing impurity scattering, suppression of the long-range antiferromagnetic order in the CuO_2 plane, or changing the number of mobile charge carriers [41]. But the real site of oxygen vacancy is not clear among in the CuO_2 plane, in the PrO layer, or in the apical site located directly above the copper in the CuO_2 plane. Recently the oxygen deficiency has been clarified not to stimulate the electron carriers such as Ce doping, but to cause hole-type mobility on the CuO_2 plane, and the reducing oxygen annealing creates a vacancy in the CuO_2 plane [32] which

means perhaps the same mechanism can be applied both to hole-doped and electron-doped superconductors [56].

With changing oxygen content, the corner-shared spin chain system $\text{Sr}_2\text{CuO}_{3+\delta}$, which is not a typical 2D cuprate, shows superconductivity at $\delta = 0.1$ with high pressure synthesis [43]. And changing the apical oxygen occupancy by using annealing under 1 atm N_2 at low temperatures (150 K to 250 K), T_c could be increased from 70 K to 89 K up to 95 K [67].

However there has previously been no systematic research on the effects of oxygen deficiency on the CuO_2 plane of edge-sharing chains as far as we know. The oxygen-effect studies discussed above are not directed towards the oxygen in the CuO_4 plane because there are several sites allocated to oxygen in the previously-studied compounds, and it is not easy to figure it out which oxygen site is vacant. Even finding out which site the removable oxygen is from would be worthy of a Nature publication such as the case of electron-doped superconductors [56]. Usually oxygen in a CuO_2 plane, where superconductivity is believed to appear, are the last one that could be removed because of the stability of the site. So it is not easy to study the effects of oxygen deficiency directly on the plane. But the CuO_2 chain compound studied here can be a good substitute, because 1D study can give good insights into 2D effects. And it is also attractive because it can give a playground to test many theories of the spin dynamics, and it can be a good candidate to find new superconductors with a simple geometry. The CaYCuO system is one of most interesting spin chain systems. This system is hole-dopable by using

either Ca-ion or oxygen deficiency, which makes a direct comparison available between cation and oxygen effect on the Cu_2 chain.

Chapter 3

Experiments

3.1 Sample Preparation

All samples of $\text{Ca}_{2+x}\text{Y}_{2x}\text{Cu}_5\text{O}_{10-\delta}$, where $x = 0, 0.5, 0.75, 0.9, 1.0, 1.25,$ and 1.5 , were prepared in the form of a polycrystal with the conventional solid state reaction method. Each of the three initial ingredients CaCO_3 , Y_2O_3 , and CuO was predried at $100\text{ }^\circ\text{C}$, $900\text{ }^\circ\text{C}$, and $450\text{ }^\circ\text{C}$, for over 12 hours. The predried ingredients were measured precisely down to 10^{-4}g according to the chemical formula. They were mixed and ground in a deep-form agate mortar with a pestle for over 1 hour. Acetone might be added to help samples mix homogeneously. The mixed ingredients were put in an Al_2O_3 crucible and baked at 900°C for more than 12 hours to take the CO_2 out from CaCO_3 . This is the calcination procedure. After cooling the ingredients in air, they are mixed and ground again for 1 hour. And then the mixed ingredients are baked at 1000°C so they can undergo solid-state reaction. We repeated the mixing and baking procedure twice more to complete the reaction with good homogeneity. We noticed that one may feel, from the pestle, grains becoming less coarse after each mixing and grinding procedure.

Then each sample with the same cation doping up to $x = 1.0$ is divided

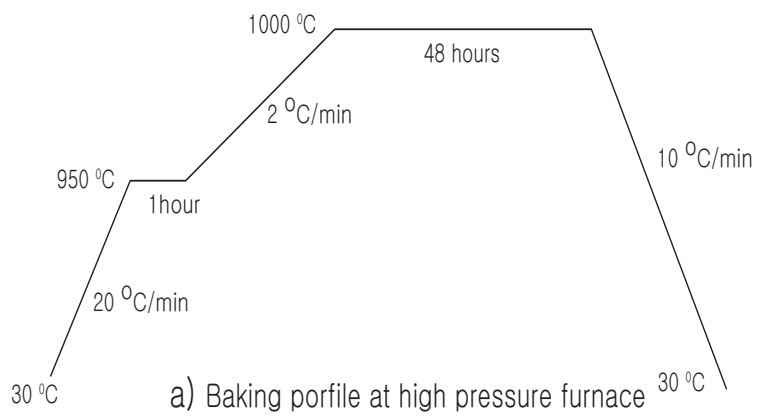
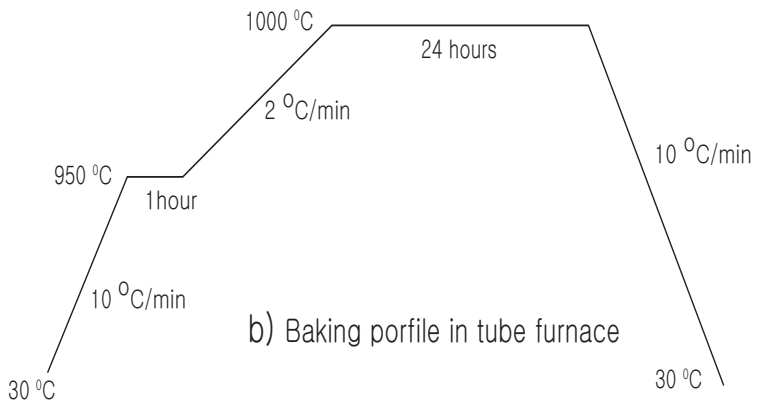
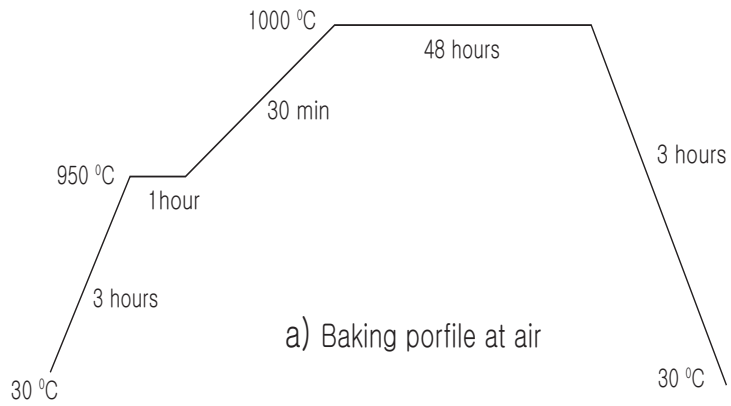


Figure 3.1: Baking profiles in three different furnaces

into three groups for different oxygen annealing procedures. The groups were as followed : the first group, the no oxygen annealed sample group, the second group, the 1 atm oxygen annealed group, and the last group, the 170 atm oxygen annealed group. No further annealing procedure was done for the first group. The samples in the second group, however, were put in a combustion boat and annealed twice for over 24 hours at 1000°C with 1 atm O₂ flow in a Lindberg Mini Mite tube furnace (Model 55035). A high-pressure oxygen furnace (Model HPS-3210P, Morris Research Co.) was utilized to make the sample fully oxygenated for the third group. The third group samples were annealed for 48 hours at 1000°C and 170 atm oxygen pressure. Careful attention is needed to check the increase of oxygen pressure. The oxygen pressure at room temperature could be more than doubled at 1000°C. For example, 8 atm at room temperature goes to 11 atm at 1000°C, 50 atm at room temperature goes to 101 atm at 1000°C, and 71 atm at room temperature goes to 152 atm 1000°C. For $x = 1.25$ and 1.5, several oxygen pressures were tested because the first two groups failed to make a single phase. The baking profile is summarized in Fig. 3.1.

3.2 Sample Analysis

The phase purity of each and every sample was investigated by x-ray diffraction experiments. Oxygen deficiency was determined with iodometric titration.

3.2.1 X-ray Diffraction [103]

Most solid materials can be described as crystalline. When x-rays interact with a crystalline substance, one gets a diffraction pattern. In 1919 A. W. Hull [48] wrote a paper titled, "A New Method of Chemical Analysis." Here he pointed out that "every crystalline substance gives a pattern; the same substance always gives the same pattern; and in a mixture of substances each produces its pattern independently of the others." The x-ray diffraction pattern of a pure substance is, therefore, like a fingerprint of the substance. The powder diffraction method is thus ideally suited for the identification and the quantification of polycrystalline phases. Nowadays x-ray diffraction is utilized to find crystallite size and its distribution for nanomaterials as well as to determine the structure of single crystals.

Scattered x-ray beams from planes of regularly arranged atoms interfere constructively when they satisfy a condition, called the Bragg law, which can be written as $2d\sin\theta = n\lambda$. Here d is the spacing of the planes, θ is the angle between the incident beams and the scattering planes, n is an integer, and λ is the wavelength of the x-rays. When such a beam is accumulated (over 10^3 or 10^5 planes), the Bragg-reflected beam becomes intensified and readily detected. We may also express this law as $\mathbf{k}' - \mathbf{k} = \Delta\mathbf{k} = \mathbf{G}$ or $2\mathbf{k} \cdot \mathbf{G} = G^2$, where $d(hkl) = 2\pi/|G|$, (e.g., $d^2 = a^2/(h^2 + k^2 + l^2)$ for a simple cubic lattice), and where \mathbf{k} and \mathbf{k}' are the wave vectors of the incoming and scattered beams, respectively, and $\mathbf{G} = h \mathbf{b}_1 + k \mathbf{b}_2 + l \mathbf{b}_3$ is a reciprocal lattice vector, and h, k , and l are integers. This law results from the periodicity of the lattice. For an

arbitrary crystal, we may need to consider the scattering amplitude for the case of a crystal with a basis, that is, an arrangement of atoms, for each lattice atom. For a crystal of N cells, it can be written as $F_{\mathbf{G}} = NS_G = N \sum_j f_j \cdot \exp[-i\mathbf{G} \cdot \mathbf{r}_j]$ where S_G is the structure factor and f_j is the atomic form factor. Assuming $\mathbf{r} = \mathbf{x} + \mathbf{y} + \mathbf{z}$, $S_G = \sum_j f_j \cdot \exp[-i2\pi(h \times x_j + k \times y_j + l \times z_j)]$. From the structure factor, we may find from which set of (hkl) the bright peak comes.

All experiments were performed with a Phillips Powder Diffractometer at a Texas Materials Institute facility which is located on 9th floor of the ETC building. When electrons with around 30 - 45 kV are collided into Cu metal, both continuous and characteristic radiations are emitted. To extract Cu K_α ($\lambda = 1.5418 \text{ \AA}$), which is the x-ray source of our experiment, from all radiation, a LiF single crystal is used as a monochromator aligned with 22.5° to the beam line and Ni foil is used to absorb Cu K_β ($\lambda = 1.3922 \text{ \AA}$). $20 \mu\text{m}$ -Ni foil can reduce the intensity of Cu K_β up to 99%, but the intensity of Cu K_α is reduced only 58 %. The scattered beams from the sample are monitored with a scintillation detector made with a NaI crystal.

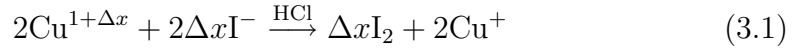
10 - 20 mg of powder samples were prepared on a sample slide coated with a drop of amyl acetate. The data with the range of $10^\circ \leq 2\theta \leq 80^\circ$ were collected for 3 seconds with 0.05° step size. So it takes around 1 hour 10 minutes to complete 1 data set. Basically, intensity and 2θ are recorded as a mdi file format, which is analyzed with the Jade 7.0 program. At first, we subtract background, and identify peak index and angle of the peaks. By using this information, we may identify samples or calculate the lattice parameters.

A data base is used to identify samples collected by "the International Center for Diffraction Data", which had over 300,000 single phase profiles by 2003.

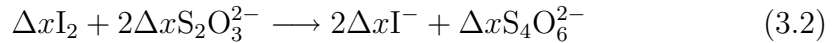
3.2.2 Iodometric Titration

Oxygen deficiency can be found using various techniques including iodometric titration [4, 37, 44, 77], thermogravimetric analysis [53], neutron diffraction [28, 35] and photoemission [95] spectroscopy etc. Among those, iodometric titration is relatively simple, economical and accurate. For example, a typical accuracy is 1/100 of an oxygen per formula unit of most compounds. For the YBCO-123 system, the accuracy is better than 1/20 of that of thermogravimetric analysis. However the oxygen deficiency determined from titration can't be applied for a system with defects or multiphases because this technique assume the specimen is stoichiometric and single phased.

Basically, this technique consist of two titrations. See Appendix A for the details of the procedures. In the first procedure, the sample is dissolved in an HCl/KI solution under argon before titration,



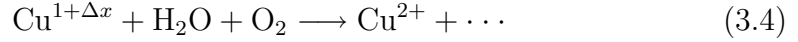
The amount of free iodine evolved is measured by performing a titration using sodium thiosulfate, $\text{Na}_2\text{S}_2\text{O}_3$ and starch indicator, and determines the charge in excess of +1 per copper ion, here called Δx or $(1+p)$.



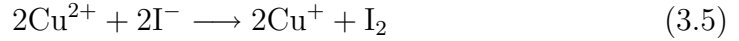
Here Δx is the mole number of the titrant per mole of copper and also is the number of electrons to turn $\text{Cu}^{1+\Delta x}$ in Cu^+ . Therefore,

$$\Delta x = \frac{\text{mole number of the titrant}}{\text{mole of copper}} = \frac{C_{t1} \cdot V_1}{n \cdot W_1/W_m} \quad (3.3)$$

where C_{t1} is the molarity of the titrant, V_1 is the volume of the titrant used in the first titration, n is the number of coppers in a formula unit, and W_m is the molar weight of the sample. This quantity Δx is normalized by a second titration on a separate specimen: the sample is dissolved in HCl and heated in air to convert all copper to Cu^{2+} .



Then KI solution is added under argon before titration.



Here the mole number of the titrant is equal to that of copper ions, $C_{t2} \cdot V_2 = n \cdot W_2/W_m$. Therefore, this procedure gives the formula weight when there is difficulty determining it due to the uncertainty of the oxygen content. Then,

$$\Delta x = \frac{\text{mole number of the titrant}}{\text{mole of copper}} = \frac{C_{t1} \cdot V_1}{n \cdot W_1/W_m} = \frac{W_2 \cdot C_{t1} \cdot V_1}{W_2 \cdot C_{t2} \cdot V_2} \quad (3.6)$$

Moreover, if the same titrant solution is used for both titrations ($C_{t1} = C_{t2}$), the concentration of the titrant doesn't need to be known exactly. For $\text{Ca}_{2+x}\text{Y}_{2-x}\text{Cu}_5\text{O}_{10-\delta}$, the oxygen deficiency is given by $\delta = 1/2 \cdot (x - 5\Delta x + 5)$ from a charge balance, $(2+x) \cdot (+2) + (2-x) \cdot (+3) + 5 \cdot (1+\Delta x) + (10-\delta) \cdot (-2) = 0$. And for Y123, $\delta = (4 - 3 \cdot \Delta x)/2$. Performing the two titrations precludes any need to calibrate the various solutions which could be a tedious process, and avoids many systematic errors.

3.3 Magnetic Properties

Magnetic measurement were performed with a Quantum Design Magnetic Property Measurement System (MPMS). The principal components of this system are a temperature control system (2 K \sim 400 K), a magnetic control system (-5 T \sim 5 T), a Superconducting Quantum Interference Device (SQUID) amplifier system (the heart of magnetic moment detection system), a sample handling system (step samples up and down smoothly), and a computer operating system (all operations are under automated computer control). Several different superconducting components are included in the system such as a superconducting magnet to generate large magnetic fields, a superconducting detection coil which couples inductively to the sample, a superconducting magnetic shield surrounding the SQUID as well as a SQUID connected to the detection coil.

Magnetic measurements are performed in the system by moving a sample through a superconducting detection coil, which induces an electric current in the coils. The current makes a change in the persistent current in the closed circuit consisting of a detection coil, the connecting wires, and the SQUID input coil, which is proportional to the change in magnetic flux. As the SQUID, a most sensitive device, functions like a highly linear current-to-voltage converter, the current change produces a corresponding voltage change in the SQUID output voltage which is proportional to the magnetic moment of the sample. The detection coil is wound in a set of three coils configured as a second-order (second-derivative) gradiometer, which is located outside of the

sample space within the liquid helium bath. The configuration is adapted to reduce noise in the detection circuit caused by fluctuations in the large magnetic field of the superconducting magnet, and to minimize background drifts in the SQUID detection system caused by relaxation in the magnetic field of the superconducting magnet.

For polycrystal powders, we usually hold a sample in a #4 gelatin capsule with cotton and make holes on the top and bottom of the capsule to prevent the deformation of the capsule upon pumping to vacuum. We may use a polycarbonate capsule in the case that the gelatin capsule does not work because it melts in water (nanoparticles are often mounted from solution samples). The capsule with a sample is put into translucent plastic drinking straws (DIXIE co.) with 0.22 in. diameter and 7 3/4 in. length, holes are made on the straws more than 3 cm away from the sample, and one end of the straws is blocked with a 3/4 inch wide polyimide tape (kapton tape - 3M Tape 5413) to avoid sample loss. We move a sample through the superconducting detection coil for 4 cm and perform a measurement at each of 32 position (for a given temperature and magnetic field) to get a data point. The minimum total moment limit of the system is around 10^{-7} emu, the moment signal from the sample holder (capsule, cotton and straw) is around 10^{-6} emu at 1000 Oe applied field and the moment signal from the sample (20 mg \sim 100 mg of CYCO) is around $10^{-4} \sim 10^{-3}$ emu at 1000 Oe applied. The typical values for the core ionic diamagnetic behavior (in units of $\times 10^{-6}$ emu/mole) are $\text{Ca}^{2+} = -8$, $\text{Y}^{3+} = -12$, $\text{Cu}^{1+} = -11$, $\text{Cu}^{2+} = -12$, $\text{O}^{2-} = -12$. Then for an

example of diamagnetism correction values, $\text{Ca}_3\text{Y}_1\text{Cu}_5\text{O}_{10-\delta}$ has -2.11×10^{-4} emu/mole.

The molar susceptibility was calculated from the measured magnetic moment M with the equation,

$$\chi_M = \frac{M \cdot m_W}{m \cdot H} \quad (3.7)$$

For 34 mg of $\text{Ca}_3\text{Y}_1\text{Cu}_5\text{O}_{10-\delta}$, we determined the molar magnetic susceptibility to be

$$\chi_M(\text{per Cu mole}) = \frac{0.00160 \text{ emu} \cdot 680.96 \text{ g/mole}}{5 \text{ per Cu} \cdot 0.0340 \text{ g} \cdot 1000 \text{ Oe}} = 0.00644 \text{ (emu/Oe/mole of Cu)} \quad (3.8)$$

Therefore, the data ($0.00644 \times 5 = 0.0322$ emu/mole) has a less than 1% diamagnetism correction.

3.4 Heat Capacity

3.4.1 Review of Measurement Techniques

As many other techniques have been introduced to measure specific heat, I want to focus on three popular ones including adiabatic, AC temperature, and relaxation methods [6, 96]. Input power and its temperature response of each method are illustrated in Fig. 3.2. Adiabatic calorimetry comes from the classical definition of the specific heat (per unit mass)

$$c_p(T) = \lim_{\Delta T \rightarrow 0} (\Delta Q / \Delta T)_P / M \quad (3.9)$$

ΔQ is the heat energy input given by a pulse which increases temperature by ΔT in a specimen of mass M . The specimen is contained in an addenda consisting of the specimen support system, thermometer, resistive heater, and wires. The assembly of specimen and addenda is isolated thermally from the surroundings, which is why this technique is called adiabatic calorimetry. The heat input is calculated by measuring current, voltage, and the duration of the heat pulse. The temperature is monitored as a function of time, and ΔT is the difference between the initial and final temperatures of the pulse after extrapolating to correct any heat exchange with environment, which should be small, typically around $T/10$. When using this technique, the specimen should be at thermal equilibrium with its surroundings before and after each heat pulse, which is different from continuous heating calorimeters. The adiabatic method works well with a high accuracy for specimens with a mass greater than about 20 mg and up to several tens of grams, in the temperature range from 0.3 K to 30 K. It is not suitable for temperatures below about 0.3 K because a heat switch, commonly used to cool the calorimeter, injects a significant amount of heat energy into the calorimeter at the lowest temperature. Thermal isolation of the specimen may become difficult for a specimen mass below 20 mg, as heat leaks may become large when compared to the experimental heat input. And the heat capacity of the addenda may become the largest portion, 80% or 90% of the measured heat capacity for a small specimen; such large addenda corrections limit the accuracy of the heat capacity determination.

AC-temperature calorimetry was introduced by Sullivan and Seidel[102]

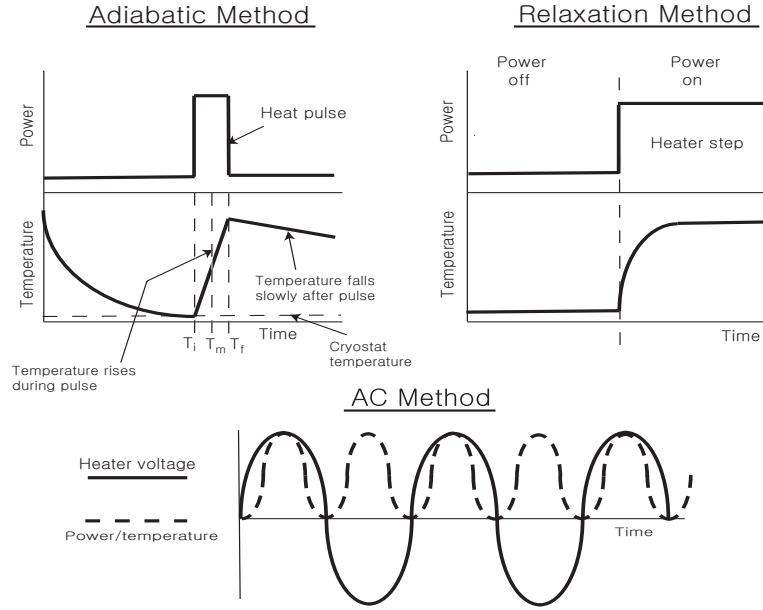


Figure 3.2: Three methods of low temperature calorimetry

in 1968 for smaller specimen whose mass is below a lower limit of the classical adiabatic calorimeter. Specimens with below around 200 mg can not be used in the classical adiabatic calorimetry because of the difficulty in achieving excellent thermal isolation and the minimization of stray heat leaks. In AC-calorimetry, ac-current of angular frequency $\omega/2$ is applied through the resistance heater to heat a specimen, and ac temperature response, T_{ac} is measured by monitoring the voltage across a resistance thermometer at frequency ω using a lock-in amplifier. Then the total heat capacity can be calculated from

$$T_{ac} = \frac{\dot{Q}_0}{2\omega C_P} \left[1 + \frac{1}{\omega^2 \tau_1^2} + \omega^2 \tau_2^2 + \frac{2K_b}{3K_s} \right]^{-1/2} \quad (3.10)$$

where \dot{Q}_0 is the amplitude of the sinusoidal heat flux, τ_1 is the specimen to

bath relaxation time, τ_2 is the combined response time of the specimen, heater and thermometer to the heat input, K_b is the thermal conductance of the specimen to the bath, and K_s is the thermal conductance of the specimen. With a choice of experimental conditions such as $\tau_2 \ll 1/\omega$, $\tau_1 \gg 1/\omega$ and $K_s \gg K_b$, the expression for C_P becomes simple,

$$C_P \simeq \frac{\dot{Q}_0}{2\omega T_{ac}} \quad (3.11)$$

Sullivan and Seidel measure a 9 g specimen of indium using 10 Hz ac temperature modulation with a peak-to-peak value of 4 mK. Their relaxation time corections were $\tau_1 = 2.5 \pm .1$ sec, $\tau_2 = (0.7 \pm 0.3) \times 10^{-3}$ sec. Due to the ability to detect small changes in heat capacity, from 10^{-8} to 10^{-12} J/K, the ac-calorimetry has become known as microcalorimetry or nanocalorimetry. And also it can be used up to the melting point of refractory metals, not just at low temperature, which is the reason it is referred as 'Modulation Calorimetry'.

Another technique for small samples (1 mg to 100 mg) is thermal relaxation calorimetry, which can be used over a wide temperature range (below 1 K to 300 K). Physical Properties Measurement System (PPMS) of Quantum Design has adapted this technique because of its simple cryostat design and specimen mounting, and the availability of improving the signal to noise ratio using signal averaging. In this method, the specimen is connected to a constant temperature bath (T_0) by a weak thermal link. The temperature of the sample is raised by a small amount (ΔT , typically $\Delta T/T \approx 1\%$), and then it is allowed to decay exponentially down to the the bath temperature. The

temperature of the specimen, T_s , is described by

$$T_s = T_0 + \Delta T \exp(-t/\tau_1) \quad (3.12)$$

where t is time and τ_1 is the specimen to bath time constant. The heat capacity, C_P , is determined from

$$C_P = \tau_1 K \quad (3.13)$$

where K is the thermal conductance of the weak thermal link. We may use a thermal link whose thermal conductance is already known, for example, pure gold (25 mm long and 0.076 mm in diameter) has 5×10^{-4} W/K, and gold alloyed with 7 at.% copper with the same dimensions has 5×10^{-6} W/K. And also it can be determined using the heater power, P , from $K = p/\Delta T$. This method becomes the adiabatic method for the limit where K is very small. Sometimes we need to consider so called ' τ_2 effects' which occur when τ_1 and τ_2 are comparable (normally $\tau_1 \gg \tau_2$). This effect makes the temperature of the specimen different from that of the thermometer, which can be noticed by an overshoot in the thermometer and a non-exponential shape in the decay rate.

3.4.2 Semi-adiabatic calorimetry

The calorimeter in this work was constructed by Dr. Michelle Chabot based on the adiabatic technique [12]. The sample is mounted to one side of the addenda which is made of a 0.005 inch (.125 mm) thick by .25 inch (6.35 mm) diameter sapphire disk with 1 mg Apiezon N-grease. See Fig.3.3. The

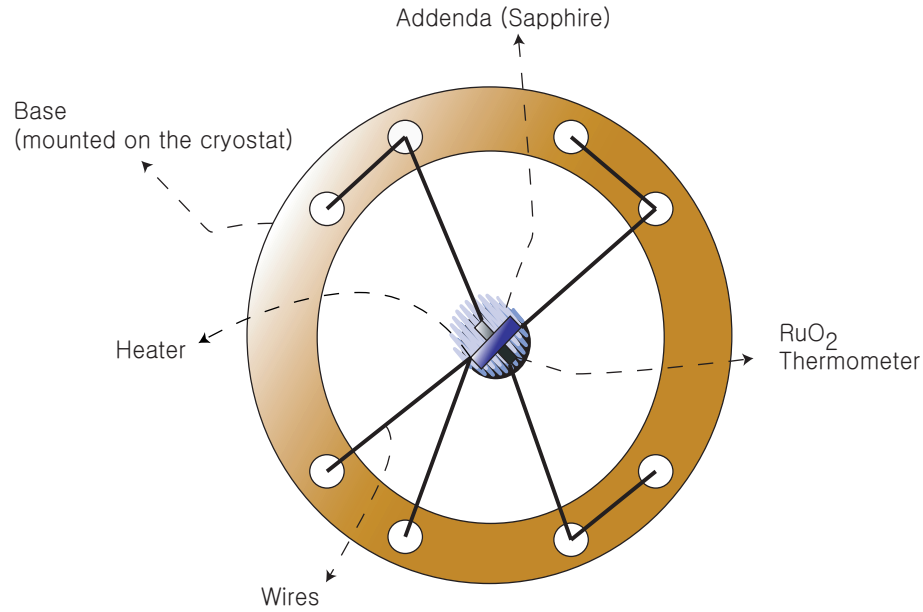


Figure 3.3: The base and addenda of the semi-adiabatic calorimeter.

average mass of samples is 25 mg. A heater and a thermometer are attached to the other side of addenda through 4 copper solder pads. The heater is a thin film chrome strip, 0.02 inch (0.5 mm) wide by .12 inch (3 mm) long, which has 120Ω of resistance at room temperature. And the thermometer is a RuO_2 nude thermometer whose resistance is $77.40 \text{ k}\Omega$ at room temperature. The addenda is suspended at the center of the header, which is a copper ring connected to the base mounted on the cryostat. The electric wires are used to suspend the addenda as well as to connect electrically the thermometer and the heater to the base. The wires are made of bare CuNi clad NbTi with a diameter of 0.0032 inches. Three wires were used as heater leads instead of two wires. This is because heat from the lead wires flows into the heater

and into the addenda with the same amount for each. Two wire leads would overestimate the power delivered by the heater because they would consider all resistance from the leads, and four wire leads would underestimate it because they would not consider the voltage drop in the leads.

The calorimeter is plugged into the experimental stage surrounded by a copper radiation shield can in the cryogenic probe as in Fig. 3.4. Lakeshore temperature controller (model 93CA) was used to control the base temperature with a RuO₂ thermometer (10 k Ω at room temperature) and a heater (6.2 Ω at room temperature) made of a constantan wire (60% Copper and 40 % Nickel alloy). The temperature of the calorimeter was measured with a Linear Research AC LR-400 resistance bridge at 16 Hz whose full-scale output is 2 V DC. The LR-400 output is sent to Keithley model 199 digital multimeter (DMM). A home-made current pulse generation box sends a pulse current to the heater via a manual switch and shows the output of the current reading and the time of the pulse on its LED panel. The voltage across the heater is measured by another DMM 199 to find the total heat power. The box also generates a trigger for two DMM's to start to measure and to save data some time (0.9 s) after it sends a pulse to the heater. All data are saved to files through a LabView program.

Two cans are used for thermal and electric isolation. The inner can is made of copper, and the outer can is made of stainless steel. One layer of indium wire is used to seal the outer can, which makes it possible for the sample area to get down to a vacuum of 10^{-6} torr. After flushing the dewar

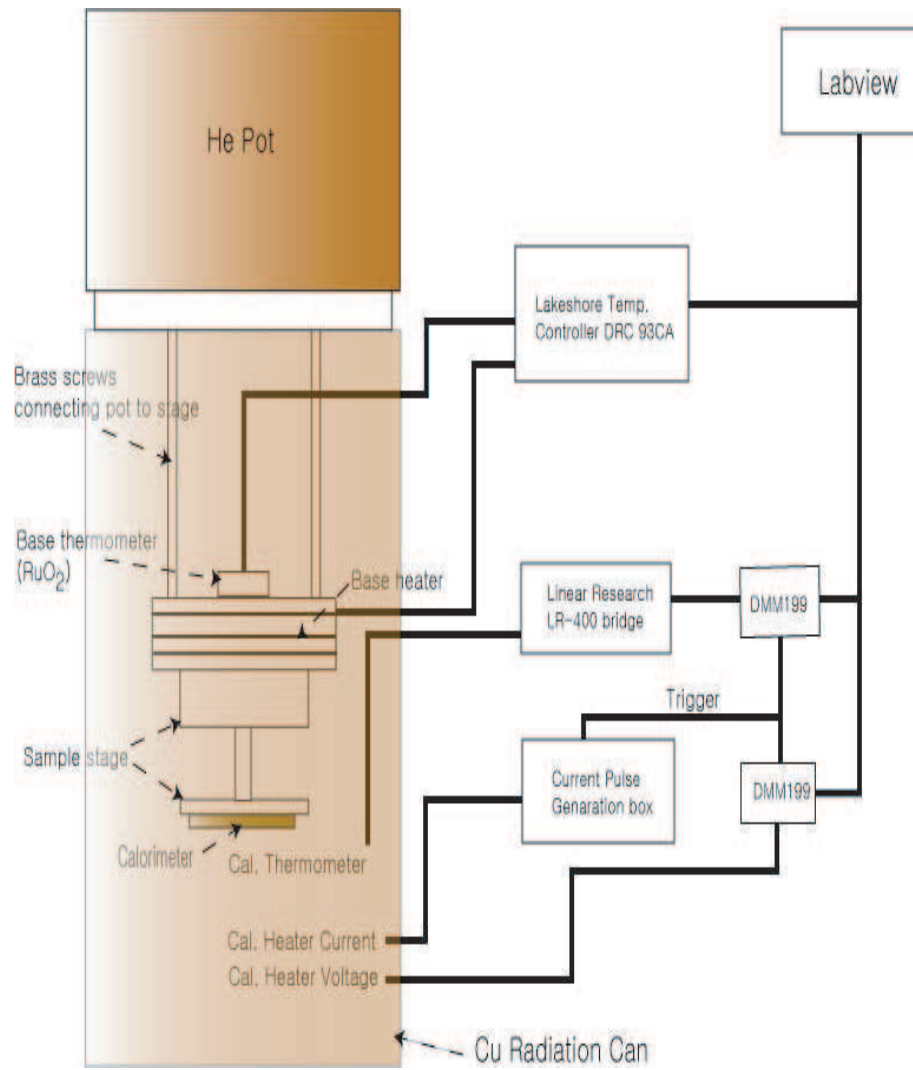


Figure 3.4: Schematic diagram and electronic setup for calorimetry.

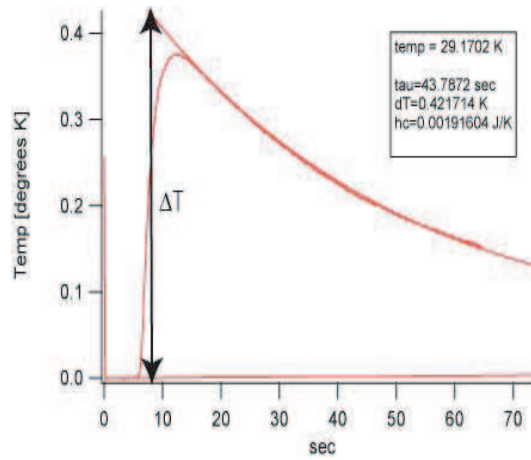


Figure 3.5: Raw data and exponential fitting to find temperature deviation and probe three or four times by using He gas, the probe is put into the dewar. Liquid nitrogen is first transferred into the outer jacket, and into the dewar. With a 250 mtorr exchange nitrogen gas in the probe, it takes around 5 hours to cool the probe down from room temperature to 77 K. The left over liquid nitrogen is removed from the dewar with overpressure He gas. Right after that, liquid He is transferred to the dewar to cool down to around 8 K, which takes around 6 hours. It takes more time to lower the temperature if it is below 10 K. After reaching around 8 K or the target temperature, the turbo pump turns on and it should be kept on during experiments, which makes the temperature rise by 1 – 3 K.

3.4.3 Data Acquisition

Basically we measure a series of resistances from a 82 k Ω RuO₂ thermometer attached to an addenda during several seconds at a fixed base temperature. Then, we convert them into temperatures to see their variation during that time by this equation,

$$T = a_1 + a_2[\ln(r/r_0)]^{0.4} + a_3[\ln(r/r_0)] + \cdots + a_n[\ln(r/r_0)]^{n-2}, \quad (3.14)$$

where T is the temperature in K, r_0 is the resistance at room temperature in units of Ω , 77408 Ω for $x = 0.5$ samples, and $a_1 = 0.2700714$, $a_2 = 0.07323249$, $a_3 = 1.0219809$, $a_4 = -1.9558035$, $a_5 = 3.4889894$, $a_6 = -4.4175955$, $a_7 = 3.6976856$, $a_8 = -1.7871035$, and $a_9 = 0.3821843$. The resistance is measured right before the heat pulse is fed in order to get the base temperature. After subtracting the base temperature from the raw data, we make an exponential or linear fit to find the temperature deviation from the heat pulse. Figure 3.5 shows the raw data and the temperature deviation. From the classical definition of specific heat, Eqn. 3.9, we can find the specific heat of the sum of addenda and sample. Figure 3.6 shows typical data of addenda and the specific heat of the sum of addenda and samples.

Finally we need to think of the error sources of the data. The most important one is the heat loss due to wiring and to the vacuum conditions. The heat loss from wires, which are made of three 0.0032-inch diameter CuNi clad NbTi, is given by [113]

$$\dot{Q}_{wire} = k \cdot A \cdot \frac{\partial T}{\partial x} \quad (3.15)$$

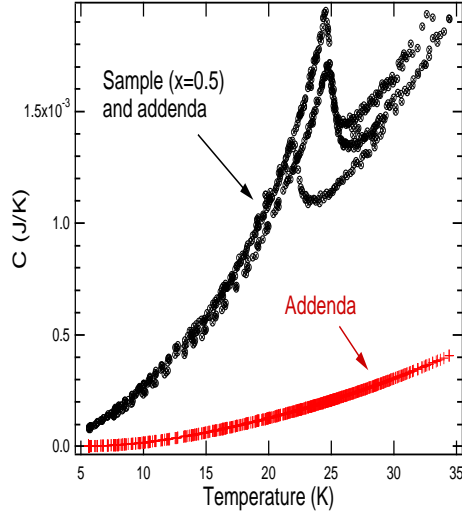


Figure 3.6: Heat capacities of the sum of addenda and samples (dots), and addenda only (crosses)

where k is the thermal conductivity of the wire approximately 100 W/mK, A is the cross section of the wire, which is $25 \times 10^{-9} \text{ m}^2$ (5 wires $\times 5 \times 10^{-9}$), the temperature increase of the sample due to the heat pulse is usually around 0.1 K, and the length of wire which makes the temperature gradient is about 1 cm. Then the heat loss is

$$\dot{Q}_{wire} \approx 2.5 \times 10^{-5} \text{ W}. \quad (3.16)$$

The thermal conductivity of a gas at normal pressures is given by [113]

$$k = \frac{1}{3} \cdot \rho \cdot l \cdot \bar{v} \cdot C_v \quad (3.17)$$

where ρ is the density, l is the mean free path, \bar{v} is the mean velocity, and C_v is the specific heat. From $l \propto 1/p$, the thermal conductivity looks independent

from the pressure. It increases monotonically with increasing temperature as T^n where n is an experimental value which is in the range from 0.6 to 0.9 for hydrogen, helium, nitrogen, and oxygen. But at low temperature and at low pressure where the mean free path is longer than the separation length between the surfaces at two temperatures, the thermal conductivity becomes a function of pressure and the heat loss is given by [113]

$$\dot{Q}_{gas} = \text{constant} \cdot p \cdot A \cdot \Delta T \text{ W/m}^2, \quad (3.18)$$

where the constant is 0.11 for a clean metallic (copper in our case) surface exposed to helium gas, the pressure in the sample space is assumed to be at most 10^{-5} torr which is 0.001333 N/m^2 , the area A is the inside surface of the copper can which is 50 cm^2 , and a typical temperature deviation $\Delta T = 20 \text{ K}$. Then the heat loss through the He gas is also

$$\dot{Q}_{gas} \approx 1.5 \times 10^{-5} \text{ W}. \quad (3.19)$$

Typical power used in this experiment is $3 \times 10^{-4} \text{ W}$ which is more than the wiring power loss or the vacuum power loss by 10 times.

Chapter 4

Fe magnetism in single-crystal LiFePO_4 and in Fe_2O_3 nanoparticles

4.1 Anisotropy in the magnetic properties of single crystal LiFePO_4

4.1.1 Background

From early research on Li-ion batteries [76], Sony Corporation introduced the first commercial four-volt cells in 1990 where a lithiated-carbon negative electrode and a LiCoO_2 positive electrode were used. Ever since, LiCoO_2 has been used worldwide especially in laptop computers and cellular telephones. However, this material is relatively expensive. In 1997, LiFePO_4 was first reported as a candidate for a substitute by John Goodenough and co-worker [82]. In addition to low cost, this compound was found to have several merits as a Li-ion battery cathode material including high specific heat, high cycle life, high thermal stability, and non-toxicity. But, this high specific heat can not be transferred effectively due to its inherently low electronic conductivity (10^{-10} to $\sim 10^{-5}$ S/m) [15, 102, 112]. Cation-doped LiFePO_4 was reported to enhance the electronic conductivity but its origin is still unclear between the substitution of Li^{+3} by cations [15] and the grain-boundary impurity [92]. To understand this enhancement, a pure, single crystal is required

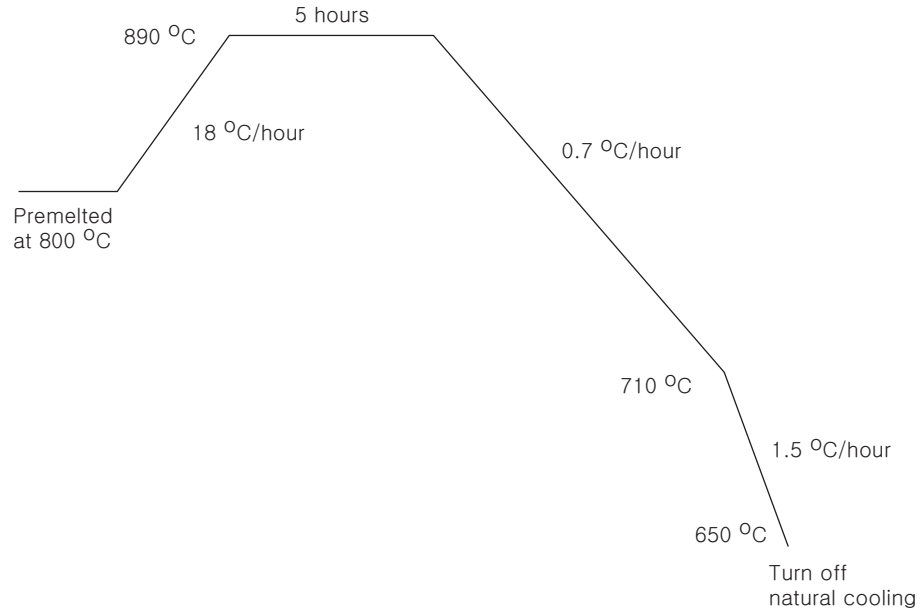


Figure 4.1: Baking profile of LiFePO₄ by using a flux method

whose size is large enough to measure its electronic and magnetic properties ($> 10 \text{ mm}^3$). Single crystals of LiFePO₄ were grown using a standard flux method with high purity FeCl₂ (99.999 % Aldrich) and Li₃PO₄ (99.999 % Aldrich). LiCl was used as a flux in Ar gas following the reaction



The growth was performed in sealed platinum crucibles with $50 \mu\text{m}$ diameter holes to release the high pressure LiCl using the baking procedure shown in Fig. 4.1. These single crystals displayed irregular shapes and dark green color with volumes up to 300 mm^3 and masses up to 1.0 g.

From single crystal x-ray diffraction experiments, the crystal is found

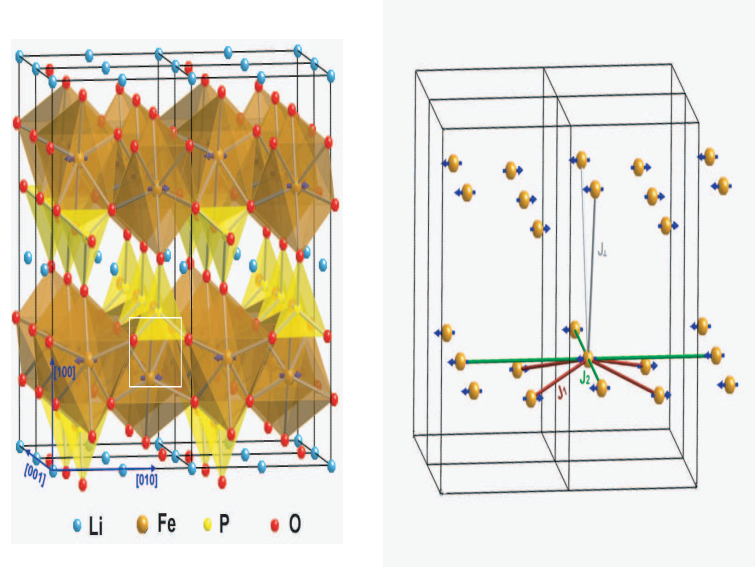


Figure 4.2: Structure diagram of LiFePO₄ (left) and magnetic interaction of Fe²⁺ ions (right).

to have orthorhombic structure with space group *Pnma* (No. 62) and lattice parameters: $a = 10.3172(11)$ Å, $b = 6.0096(8)$ Å, and $c = 4.6775(4)$ Å. Figure 4.2 shows the olivine structure of single crystal LiFePO₄, the alignment of its Fe²⁺ magnetic ions, and the primary coupling due to exchange interactions. The cations are located in three different positions which are an octahedron (Fe) site in orange, a tetrahedron (P) site in yellow and an octahedron (Li) site. The Li ions are located at the inversion centers of the highly distorted LiO₆ octahedra, which makes an edge-sharing chain along the *b*-axis [0 1 0] direction. Figure 4.3 shows the results of powder x-ray diffraction experiments in the range of $15^\circ \leq 2\theta \leq 65^\circ$, which confirm the obtained structure and no impurity.

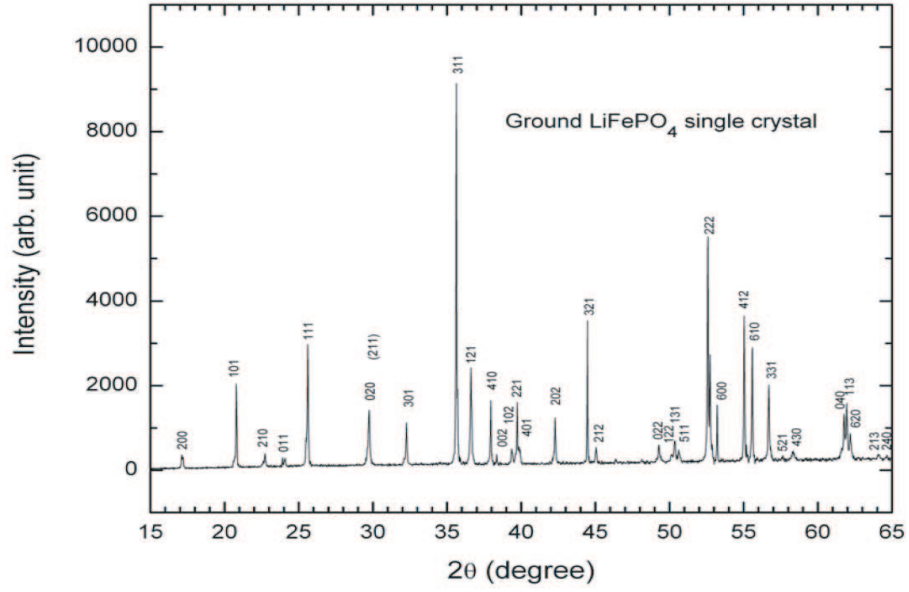


Figure 4.3: X-ray pattern of ground single crystal LiFePO_4 .

4.1.2 Results and Discussion

After confirming a high-purity single crystal, magnetic properties were measured along each direction; these results are shown in Fig. 4.4. The average $\chi(T)$ is defined as $\chi_{\text{avg}} = \frac{1}{3}(\chi_{//} + \chi_{\perp,a} + \chi_{\perp,b})$. From this graph, LiFePO_4 shows antiferromagnetic long-range order with Néel temperatures (T_N), from the peak susceptibility, of 55 K when the magnetic field is along the easy axis (b -axis) and 51 K when the magnetic field is along either the a -axis or c -axis. The enlarged figure around the transition temperature is shown in Inset (a) in Fig. 4.4. As an alternative way to quantify the transition point, we may use the peak point of $d(\chi T)/dT$ versus temperature as shown in Inset (b) in Fig 4.4. With this technique, we found Néel temperatures along all axes of 47

K which is denoted by T_N^* in Table 4.1 to distinguish between the T_N of inset (a).

The susceptibility curve along each axis in Fig. 4.4 shows a large anisotropy both below T_N (antiferromagnetic order) and above T_N (paramagnetic region) [65]. Below T_N , the susceptibility along b -axis decreases to almost zero with decreasing temperature which shows that the b -axis is an easy axis. However, the susceptibilities along a - and c -axes remain almost constant with decreasing temperature below 30 K. The big difference between the susceptibility along and perpendicular to the easy axis is normal, and can be explained with the standard two-sublattice mean field theory with uniaxial anisotropy [60]. But, the difference in susceptibilities between the two perpendicular axes to the easy axis shows another anisotropy between these two axes which cannot be explained by the simplest theory. Moreover, the anisotropy among all axes is found to persist above T_N as evidenced by the difference between the susceptibilities in the axes, which contradicts the theory. The three different curves in $\chi(T)$ in the paramagnetic regime show an anisotropy in the Curie constant, which means again an anisotropy in the Lande g -factor (g), effective magnetic moment and Curie temperature (θ).

Now we suggest a model Hamiltonian to explain these anisotropies based on the theoretical approach for single crystal FeF_2 by Homma [45] and Lines [66] and on the neutron scattering measurement by Li [64]

$$H = H_0 + H_f = \sum_i H_i. \quad (4.1)$$

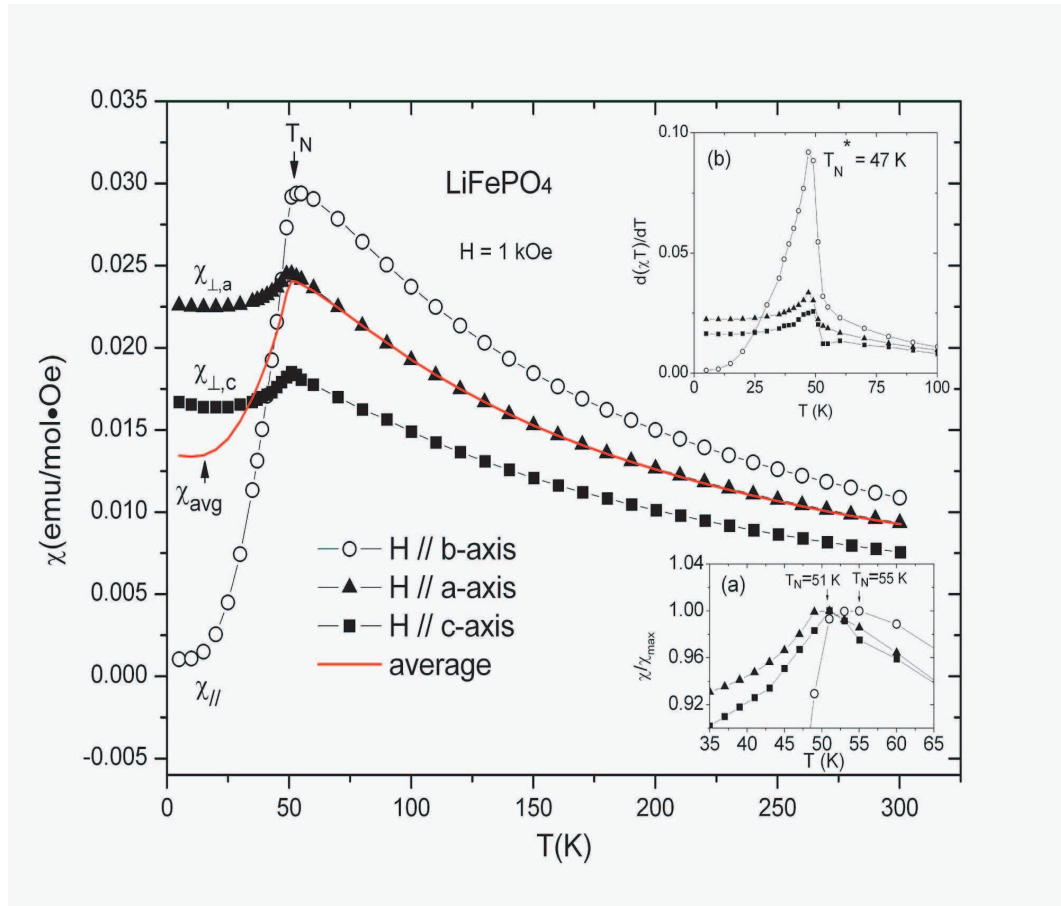


Figure 4.4: Magnetic susceptibilities of single crystal LiFePO_4 along each axis with average susceptibility. Inset (a) shows the enlarged transition temperature region. Inset (b) shows $d(\chi T)/dT$ versus temperature noting the exact Néel temperature.

Here,

$$H_0 = -J_1 \sum_{i,\delta} (\mathbf{S}_i \cdot \mathbf{S}_{i+\delta}) - J_2 \sum_{i,\xi} (\mathbf{S}_i \cdot \mathbf{S}_{i+\xi}) - J_\perp \sum_{i,\eta} (\mathbf{S}_i \cdot \mathbf{S}_{i+\eta}) + D \sum_i (S_{iz})^2, \quad (4.2)$$

where J_1 is the intralayer nearest-neighbor (NN) superexchange (SE) parameter, J_2 is the intralayer next-nearest-neighbor (NNN) super-super exchange (SSE), J_\perp is the interlayer NNN SSE parameter, and D is the single-ion anisotropy parameter [64] shown in the right part in Fig. 4.2. From neutron scattering experiments, all exchange parameters are determined after fitting the spin wave dispersion relation: $J_1 = -0.662$ meV, $J_2 = -0.27$ meV, $J_\perp = -0.021$ meV, and $D = -0.37$ meV. The number of Fe^{2+} ($S=2$) spin neighbors, z_i , corresponding to the same spin exchange parameter J_i , are $z_1 = 4$ for J_1 , $z_2 = 4$ (2 along b -axis and 2 along c -axis) for J_2 , and $z_\perp = 2$ for J_\perp .

$$H_f = \sum_i [-\mu_B (g_{\perp,a} S_{ix} H_x + g_{\perp,c} S_{iy} H_y + g_{//} S_{iz} H_z) - \mu_B^2 (\Lambda_{\perp,a} H_x^2 + \Lambda_{\perp,c} H_y^2 + \Lambda_{//} H_z^2)] \quad (4.3)$$

where

$$g_\alpha = 2(1 - \lambda \Lambda_\alpha) \quad (4.4)$$

$$\Lambda_\alpha = \sum'_n \frac{|\langle 0 | L_\alpha | n \rangle|^2}{E_n - E_0}. \quad (4.5)$$

Here, λ is the spin-orbit coupling constant, L_α ($\alpha = 1, 2, 3$) are the orbital angular momentum component operators, and $|n\rangle$ refers to orbital states with energy E_n . For LiFePO_4 , $g_\alpha > 2$ because λ is negative when a transition metal ion has more than five d electrons [55].

Now we can use these equations to obtain the magnetic susceptibility. For $T > T_N$, that is in the paramagnetic phase state, the molecular-field Hamiltonian for the i th spin is given, for the case with a magnetic field applied parallel to the easy axis, or b-axis (z-axis) that is $H = H_z$,

$$H_i = -(z_1 J_1 + z_2 J_2 + z_\perp J_\perp) \bar{S} S_{iz} + D S_{iz}^2 - g_{//} \mu_B S_{iz} H - \mu_B^2 \Lambda_{//} H^2. \quad (4.6)$$

For the case of a weak magnetic field applied perpendicular to the a -axis (x -direction), considering $\bar{S}_y = 0$ and $\bar{S}_z = 0$, the Hamiltonian is

$$H_i = -(z_1 J_1 + z_2 J_2 + z_\perp J_\perp) \bar{S}_x S_{ix} + D S_{ix}^2 - g_\perp \mu_B S_{ix} H_x - \mu_B^2 \Lambda_\perp H_x^2. \quad (4.7)$$

Following Lines [66] and Honma [45], we can get the susceptibilities in the form of the Curie-Weiss law (see the appendix for the details). With the magnetic field applied parallel to the easy axis,

$$\chi_{//}(T) = \chi_{b0} + \frac{C_{//}}{T - \theta_{//}}, \quad (4.8)$$

where $\chi_{b0} = 2N\mu_B^2 \Lambda_{//}$. The Curie constant (C) and Curie-Weiss temperature (θ) are given by

$$C_{//} = S(S+1)N g_{//}^2 \mu_B^2 / 3k, \quad (4.9)$$

$$\theta_{//} = -\frac{1.4D}{k_B} + \frac{S(S+1)}{3k_B} \sum_i z_i J_i, \quad (4.10)$$

where $S = 2$ for Fe^{2+} . For the magnetic field applied perpendicular to the easy axis

$$\chi_{\perp,a}(T) = \chi_{a0} + \frac{C_{\perp,a}}{T - \theta_{\perp,a}}, \quad (4.11)$$

$$\chi_{\perp,c}(T) = \chi_{c0} + \frac{C_{\perp,c}}{T - \theta_{\perp,c}}, \quad (4.12)$$

where $\chi_{a0} = 2N\mu_B^2\Lambda_{\perp,a}$ and $\chi_{c0} = 2N\mu_B^2\Lambda_{\perp,c}$. The Curie constants and Curie-Weiss temperatures are given by

$$C_{\perp,a} = S(S+1)Ng_{\perp,a}^2\mu_B^2/3k, \quad (4.13)$$

$$C_{\perp,c} = S(S+1)Ng_{\perp,c}^2\mu_B^2/3k, \quad (4.14)$$

and,

$$\theta_{\perp} = \theta_{\perp,a} = \theta_{\perp,c} = \frac{0.7D}{k_B} + \frac{S(S+1)}{3k_B} \sum_i z_i J_i. \quad (4.15)$$

It is interesting to see that the average value of these three θ 's is

$$\theta_{avg} = \frac{1}{3} \sum_{\alpha=1}^3 \theta_{\alpha} = \frac{S(S+1)}{3k_B} \sum_i z_i J_i. \quad (4.16)$$

For $T < T_N$, that is the antiferromagnetic state, as $T \rightarrow 0$

$$\chi_{//}(0) = 2N\mu_B^2\Lambda_{//}. \quad (4.17)$$

We may connect the magnetic susceptibility of a polycrystal to a single crystal if we consider a polycrystal sample composed of many small single crystals. Then χ_{poly} is

$$\chi_{poly} = \frac{1}{3}(\chi_{//} + \chi_{\perp,a} + \chi_{\perp,c}) = \chi_{avg} \quad (4.18)$$

$$= \chi_0 + \frac{C_{poly}}{T - \theta_{poly}}, \quad (4.19)$$

where

$$\chi_0 = \frac{1}{3}(\chi_{bo} + \chi_{a0} + \chi_{c0}) = \chi_{avg,0} \quad (4.20)$$

$$C_{poly} = \frac{1}{3}(C_{//} + C_{\perp,a} + C_{\perp,c}) = C_{avg} \quad (4.21)$$

$$\theta_{poly} = \left(1 - \frac{C_{//}}{3C_{avg}}\right)\theta_{\perp} + \left(1 - \frac{C_{\perp,a} + C_{\perp,c}}{3C_{avg}}\right)\theta_{//}, \quad (4.22)$$

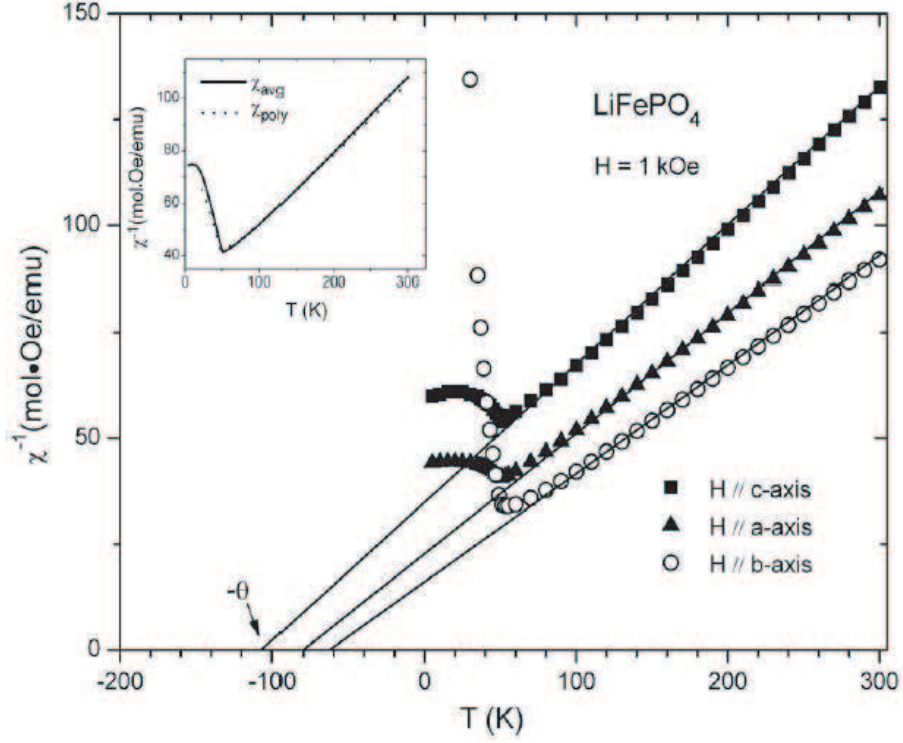


Figure 4.5: The inverse susceptibility (χ^{-1}) versus temperature along fitted to Curie-Weiss law. The inset shows the average of the magnetic susceptibilities of all axes with the polycrystal data [90].

where $\theta_{poly} = \theta_{avg}$ only when $\theta_{\perp} \neq \theta_{//}$. Also, we have

$$C_{avg} = S(S+1)Ng_{avg}^2\mu_B^2/3k_B, \quad (4.23)$$

$$g_{avg}^2 = (g_{//}^2 + g_{\perp,a}^2 + g_{\perp,c}^2)/3, \quad (4.24)$$

and the effective magnetic moment is given by

$$\mu_{eff,avg} = (8C_{avg})^{1/2}. \quad (4.25)$$

The anisotropy in the g -factor and the Curie-Weiss temperature, θ , was

Table 4.1: Néel temperature and fitting parameters from the Curie-Weiss law for LiFePO₄. Here the Curie constant C has units (emu K/mole).

Axis	T_N (K)	T_N^* (K)	C	θ (K)	g	Λ (cm)	μ_{eff} (μ_B)
$b(//)$	55	47	3.685	-59.7 ± 1.7	2.22	0.00138	5.43 ± 0.02
$a(\perp, a)$	51	47	3.412	-80.9 ± 1.3	2.13	0.00085	5.22 ± 0.02
$c(\perp, c)$	51	48	3.058	-105.7 ± 1.5	2.02	0.00012	4.95 ± 0.01
Aver.	51	47	3.371	-78.0 ± 1.5	2.12	0.00076	5.19 ± 0.01

examined by comparing the measured magnetic susceptibility with a theoretical calculation. Figure 4.5 shows the temperature dependence of the inverse susceptibilities of all axes and their fittings with the modified Curie law given by Eqn. 4.8 and Eqn. 4.11. The fitting was done for each axis in the temperature range of $70 \text{ K} \leq T \leq 300 \text{ K}$, shown as the solid lines in Fig. 4.5. The values of the g 's and Λ 's from the fitting were used to confirm the calculated numbers from Eqn. 4.5 and Eqn. 4.17. The value of $\chi_{//}(0)$ is obtained from fitting the $\chi_{//}(T)$ data to $\chi_{//}(T) = a + bT^2$ in the range of $5 \text{ K} \leq T \leq 20 \text{ K}$ because the spin-wave theory of antiferromagnetism predict a T^2 dependence of $\chi_{//}(T)$ at low temperature[61]. We use $S = 2$ to calculate the g -factor from the Hund's rule ground state (5D_4) of free $\text{Fe}^{2+}(d^6)$ ions. The fitting results are summarized in Tab. 4.1.2. From these results, the g -factor and the Curie temperature, θ , are expected to show a strong anisotropy.

The results of the magnetic anisotropy of single crystal LiFePO₄ can be compared with those from Creer *etal.* [18]. The effective magnetic moments are within 7% deviation, and their $\theta_{//} = -68 \text{ K}$ is about 10% lower than ours (-80.9 K). But $\theta_{\perp,a} = -129 \text{ K}$ and $\theta_{\perp,c} = -155 \text{ K}$ are substantially lower (\sim

40 - 50%) than ours ($\theta_{\perp,a} = -80.9$ K and $\theta_{\perp,c} = -105.7$ K). The polycrystal data from Santoro [90] can be compared with our average data of all three axes as shown in the above calculations. The inset of Fig. 4.5 indicates the perfect match of those demonstrating the relationship $\chi_{avg}(T) = \chi_{poly}(T)$. The fitting parameters of the average data with Eqn. 4.18 are also listed in Table 4.1. The fitting value of $\theta_{poly} = -78.6 \pm 1.5$ K is almost the same as the value (-81.1 K) calculated from Eqn. 4.18 using the fitting results of each axis. The effective moment ($5.19 \mu_B$) from the fitting is closer to the spin-only value ($4.90 \mu_B$) for the Fe^{2+} (d^6) ion, $S = 2$, than the value from the total angular momentum $J = L + S$ ($6.71 \mu_B$) [60], which indicates that the Fe ions in the crystal are divalent and their orbital moments are strongly quenched by crystal field. This effective moment is in excellent agreement with those of Fe ion in other compounds including FeO ($5.33 \mu_B$), FeF_2 ($5.59 \mu_B$), FeCl_2 ($5.38 \mu_B$), FeS ($5.24 \mu_B$), KFeCl_3 ($5.50 \mu_B$), and $\text{BaLa}_2\text{FeS}_5$ ($5.41 \mu_B$) [25, 36, 47, 58, 107].

We can test the exchange coupling constants J_1 , J_2 , J_{\perp} and the anisotropy parameter D if we use the estimated values from the neutron scattering experiments [64]. That is, $J_1 = -0.662$ meV, $J_2 = -0.27$ meV, $J_{\perp} = -0.021$ meV, and $D = -0.37$ meV, and using Eqns. 4.10, 4.15, and 4.16 give $\theta_{//} = -79.5$ K and $\theta_{\perp} = (\theta_{\perp,a} + \theta_{\perp,c})/2 = -88.5$ K, and $\theta_{avg} = -85.5$ K, respectively. Here $\theta_{//}$ is more negative by 19.8 K than the fitting's value (-59.7 K). But the θ_{\perp} and θ_{avg} calculated using these values of Js and D are well matched with the values ($\theta_{\perp} = -93.3$ and $\theta_{avg} = -82.1$ K) from the fitting.

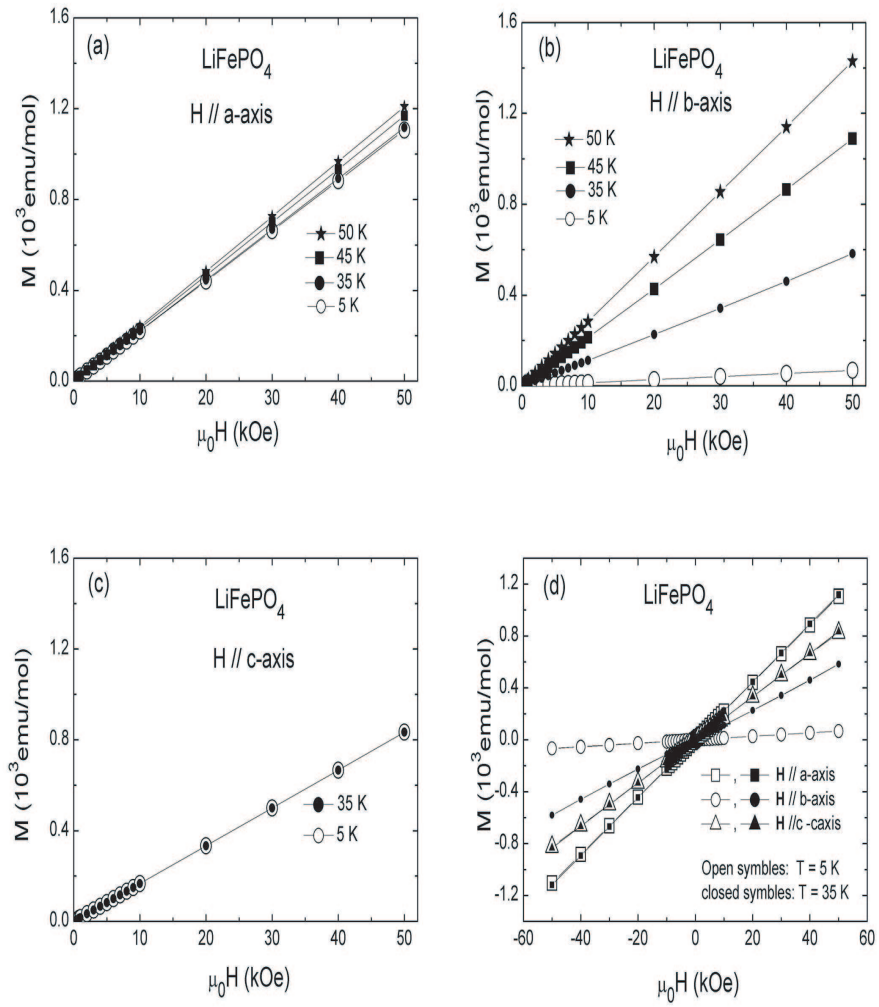


Figure 4.6: Field dependence of magnetization of each axis for different temperatures (a)-(c), and hysteresis of each axis at 5 K and 35 K (d)

Figure 4.6 (a) to (c) show the field dependence of magnetization for each axis for different temperatures below T_N from 0 to 50 kOe. We found from their linear dependence on the field that spin-flip or spin-flop does not appear in the antiferromagnetic phase in fields up to 50 kOe. Figure 4.6 (d) represents the hysteresis test of the magnetization for all axes at 5 K and 35 K. The measurement was performed varying the field from 0 Oe to 50 kOe to -50 kOe to 50 kOe. We found no hysteresis, which is consistent with the observed linearity in $M(H)$ curves of the other graph in the figure.

In conclusion, we have built a mean-field theory on the anisotropy in magnetic susceptibilities to analyze the strong anisotropy in g -factor, paramagnetic Curie temperature, and effective moment of a LiFePO_4 single crystal. The calculated values from this theory are found to match well with the values calculated from parameter obtained in neutron scattering experiments.

4.2 Effects of Au/Silica double coating on the properties of Fe_2O_3 magnetic nanoparticles

4.2.1 Background

Superparamagnetic iron oxide (SPIO) particles have been used in magnetic resonance imaging (MRI) more than gadolinium chelates, the previous MRI contrast agent, and in other biomedical applications including drug delivery. This is because they provide the most change in signal per unit of metal, especially on transverse relaxivity (T_2^*), their biodegradable iron is biocompatible so it can be reused and recycled by the cell, they are easy to link

with functional groups and ligands from their surface coating, usually dextran, they are easily detectable by light and electron microscopy, and their magnetic properties change according to size [8]. However SPIO nanoparticles (NP) disperse stably in aqueous solutions only in highly acidic or basic media. So, SPIO NPs are coated with silica to get an excellent biocompatibility and a homogenous dispersion in aqueous solutions with a wide range of pH [100, 103, 115]. Silica coated SPIO NPs are used in the MRI diagnosis of cells or tissues suffering from defects due to diseases such as cancers. However, the nanoparticles need further coating in order to be used in curing diseases. Here, gold is an attractive material because its nanoshells have strong wavelength tunable absorbance in the near-infrared region. That means it can be used in localized photothermal therapy because it can mediate strong plasmon-induced heat flux upon absorption of the near-infrared radiation. Moreover, its NPs are easy fabricate and link with other ligands and they have good biocompatibility. So, Au/SiO₂ double coated γ -Fe₂O₃ NPs could be made a bi-functional, that is, diagnostic and therapeutic, if Au NPs can be coated on the surface of silica coated NPs. It was synthesized successfully [51] and its magnetic properties are reported here.

Figure 4.7 shows the fabricated Au/SiO₂ doubly coated γ -Fe₂O₃ NPs (a) and its enlarged image (b). The average size of silica spheres, which are the large spherical particles, is measured around $D_{silica} = 81.5$ nm. The average diameter of Au particles is $D_{Au} = 6.0$ nm, which are shown as the smaller dark particles distributed on the silica spheres. The coated Au are found to

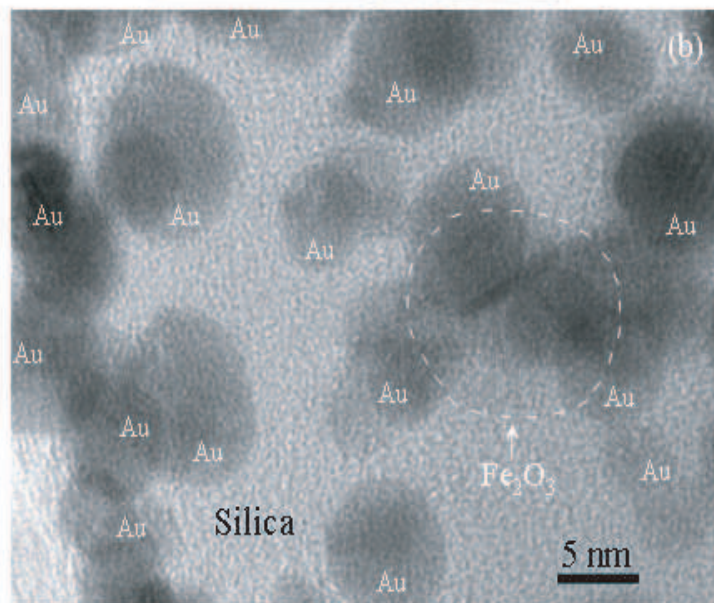
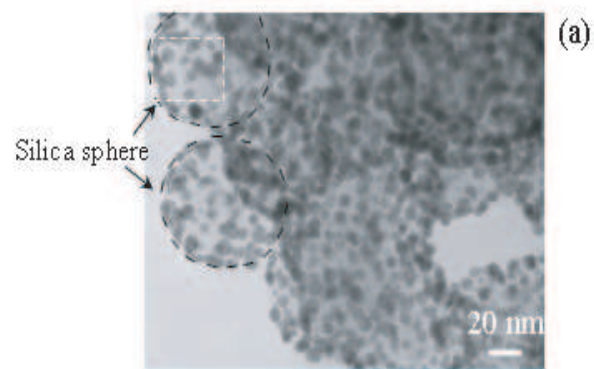


Figure 4.7: (a) Typical TEM image of Au/SiO₂ doubly coated γ -Fe₂O₃ nanoparticles. (b) Enlarged image of the rectangular area in the upper silica sphere shown by the white dashed loop.

form only particles on the silica surface not a continuous Au layer, as shown in Fig. 4.7 (b). Fe_2O_3 particles are embedded inside of the silica sphere and their average size is 12 nm, which is larger than the Au particles.

Magnetic susceptibilities of pure and coated NPs, in the form of dried powders, were measured with a Quantum Design MPMS SQUID magnetometer. Pure Fe_2O_3 particles were put in a size-#4 gelatin capsule purchased from Capsuline.com with a small amount of cotton to fix the particles. The amount of nanoparticles coated with Au and Si was too small and the powder was too brittle to be transferred, so they were dissolved in the original container with 500- μ liter distilled water and transferred with a micropipette to a polycarbonate capsule (instead of a gelatin capsule which is dissolvable with water). A size-#4 polycarbonate capsule was used, which was purchased at Unipecc Inc. from Rockville, MD. Transferred liquid-type particles were left to be evaporated in air with a Kimwipe tissue covered for over 4 days in the capsule and were confirmed to be dry enough to see a separable powder form. Magnetic measurements were performed after finding the mass of particles in the same capsule and adding a small amount of cotton to hold them fixed. The mass of particles were measured carefully down to 0.1 mg to be 3.0 mg for pure particles and 0.6 mg for the coated ones.

A typical background signal is shown at the top of Fig. 4.8. Both the polycarbonate capsule and Au/SiO₂ show magnetic moment below 3×10^{-5} emu. Above 60 K, both magnetic susceptibilities represent diamagnetic behavior independent of temperature. The bump around 50 K is from the residual

oxygen which can be reduced by many purging procedures. With temperature going down to 5 K from 40 K, the magnetic susceptibility increases due to the paramagnetic impurity of the capsule, which is seizably different for every capsule. The two middle figures show the field dependence of the background signal, which is also a typical behavior of diamagnetism except at 5 K in the case of the polycarbonate capsule alone. The nonlinear behavior comes from the combination of the diamagnetic signal and the paramagnetic background signal, but for Au/SiO₂ the diamagnetic behavior is dominant even at 5 K. The bottom graph of Fig. 4.8 shows the raw data from the Au/SiO₂ coated γ -Fe₂O₃. The signal is almost 100 times bigger than the background, and the pure γ -Fe₂O₃ NP signal is even bigger than the coated ones. Therefore, we consider the background for the coated one only.

4.2.2 Results and Discussion

Figure 4.9 shows zero-field-cooling (ZFC) and field-cooling (FC) magnetization for pure, SiO₂ coated, and Au/SiO₂ doubly coated γ -Fe₂O₃ NPs with temperatures varying from 5 K to 300 K and applied magnetic field of 10 Oe for pure γ -Fe₂O₃ NPs and 500 Oe for all other NPs [85]. All data shows irreversibility between ZFC and FC below the irreversible temperature T_{irr} where two data from ZFC and FC at the same temperature start to be different. T_{irr} is above 300 K for 10 Oe applied field but is around 300 K for the pure NPs with 500 Oe applied field and 150 K for both coated NPs with 500 Oe fields. From the 500 Oe data, the overall magnetization per gram decreases

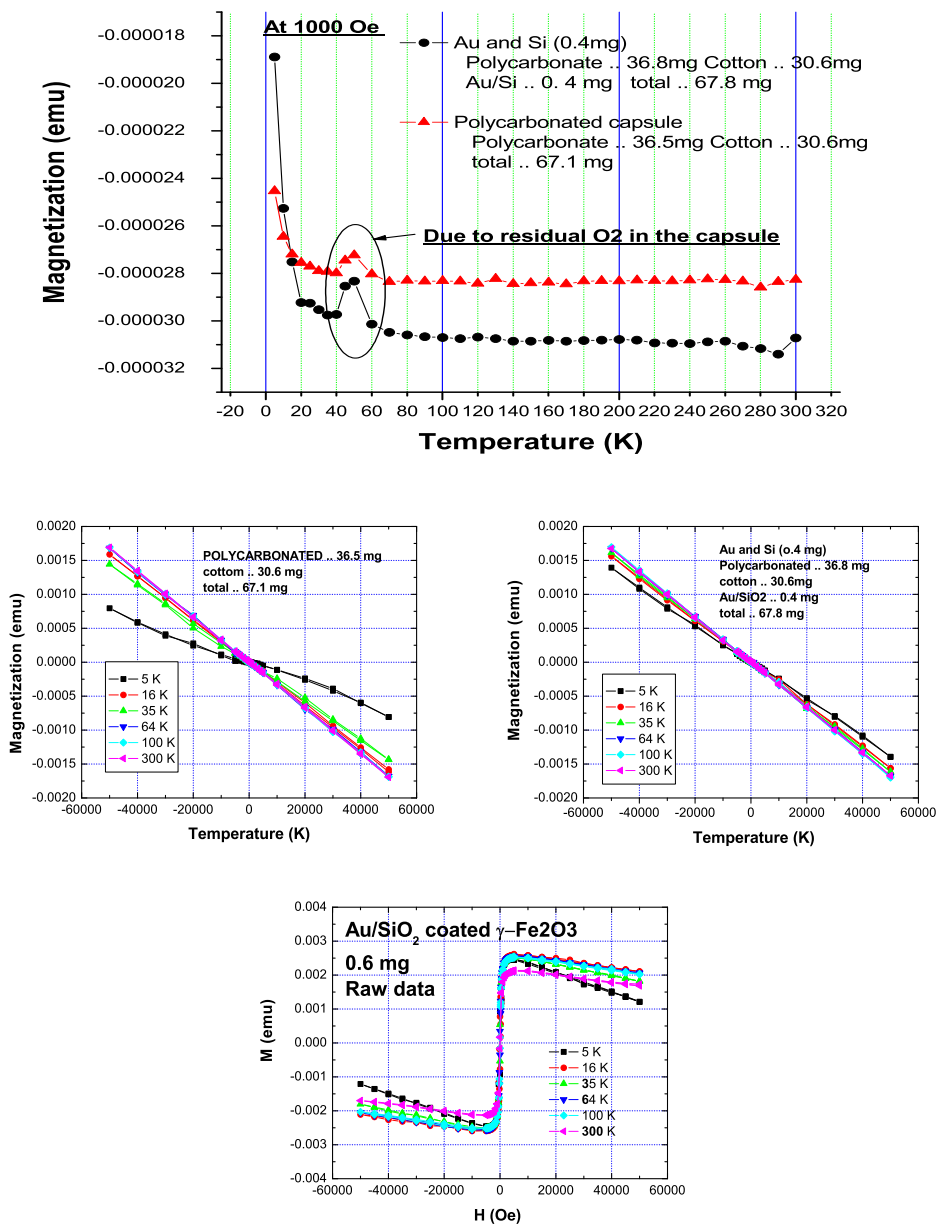


Figure 4.8: Background data of magnetic susceptibility measurements. M-T graph at the top, M-H graphs at the middle and the raw data from the Au/SiO₂ coated γ -Fe₂O₃ at the bottom.

with coating, which means that the average amount of magnetic moment of each NP becomes smaller as the diamagnetic coated mass is added. Except for the 10 Oe data, all ZFC magnetizations with 500 Oe show a broad peak, called the blocking temperature, with varying temperature. The blocking temperature of pure $\gamma\text{-Fe}_2\text{O}_3$ NPs is 160 K, but for the SiO_2 coated $\gamma\text{-Fe}_2\text{O}_3$ NPs is around 75 K, and for Au/ SiO_2 doubly coated $\gamma\text{-Fe}_2\text{O}_3$ NPs is around 85 K.

With increasing applied field from 10 Oe to 500 Oe, both T_{irr} and T_B decrease for the pure NPs (see the first two figures in Fig. 4.9). Similar behavior is observed in other $\gamma\text{-Fe}_2\text{O}_3$ NPs with almost same particle size NPs [5] and with other size NPs [20, 76]. The relation between the blocking temperature and the applied field is explained [26, 27] by

$$T_B = T_{B0} \left(1 - \frac{CH^2}{T_{B0}} \right), \quad (4.26)$$

where T_{B0} is the blocking temperature at zero field and C is a field-independent parameter.

The blocking temperature (160 K) of pure NPs is different from other data (120 K) of Jeong [50] because the average diameter of our NPs is 12 nm compared to their smaller size of 5 – 8 nm. The dependence of the blocking temperature (T_B) on NP size is given [5, 50] as

$$T_B = \frac{KV}{25k_B}, \quad (4.27)$$

where $V(= \frac{1}{6}\pi D_{avg}^3)$ is the average volume of the NPs, K is the uniaxial anisotropic constant and k_B is the Boltzmann constant. This equation shows

the proportional relation between the blocking temperature and the average volume, and is effective for both Jeong's and our NPs. The proportional constant ($\Delta T_B/\Delta D_{avg}$) is normally between 15 K/nm and 80 K/nm [50, 69]. Our case with Jeong's (40 K / 4 nm = 10 K/nm) is below this range.

The decrease of T_B from 160 K to 80 K with the diamagnetic material coating is shown in Fig. 4.9. This decrease due to the coating is attributed to the following two factors. First, the reduction of the average effective volume of the γ -Fe₂O₃ core, and second, the decrease in strength of the dipole-dipole interactions between the γ -Fe₂O₃ cores. From the above TEM data, the SiO₂ nanoshells with the 35 nm thickness coated on γ -Fe₂O₃ spheres and the Au NPs ($D_{avg} \approx 6$ nm) are dispersed in a thin layer near the outer surface of the SiO₂ nanoshells. This means the Fe ions at the outer core can interact only with SiO₂ ions not with Au. Therefore, there is no big change in the magnetic behaviors between SiO₂ coated γ -Fe₂O₃ and Au/SiO₂ doubly coated γ -Fe₂O₃. The interaction of the outer Fe ions with SiO₂ induces a thin layer of misaligned or disordered Fe spins near the surface of γ -Fe₂O₃ core. This layer cannot give an effective contribution to the total magnetization, M , and therefore it should be excluded in calculating the effective volume, V , in Eqn. 4.27. That is, if the average thickness of the disordered layer is t , the effective volume for the γ -Fe₂O₃ core in the Au/SiO₂ coated NPs is defined as

$$V_{eff} = \frac{\pi(D_{avg} - 2t)^3}{6}. \quad (4.28)$$

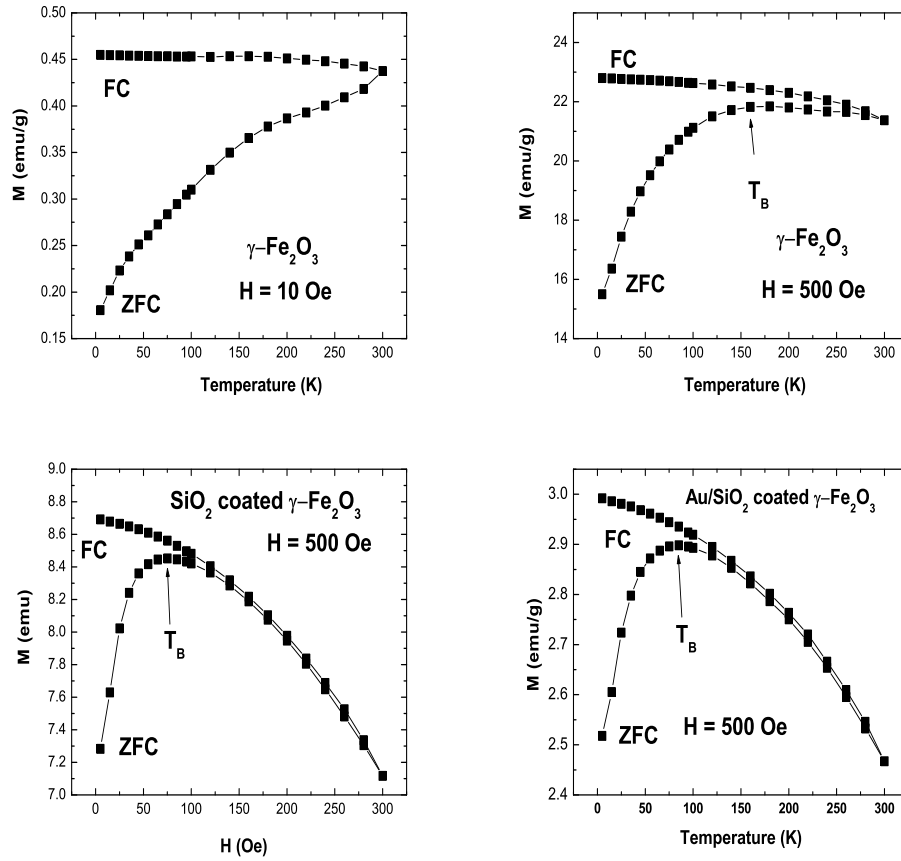


Figure 4.9: Field cooling (FC) and zero-field-cooling (ZFC) of magnetization graph for the pure $\gamma\text{-Fe}_2\text{O}_3$ with 10 Oe and 500 Oe, for the SiO_2 coated $\gamma\text{-Fe}_2\text{O}_3$ with 500 Oe, and for Au/SiO_2 coated $\gamma\text{-Fe}_2\text{O}_3$ with 500 Oe. The blocking temperature are expressed as an arrow.

Then, Eqn. 4.27 should be changed to

$$T_B = \frac{KV_{eff}}{25k_B} = T_B(0)\left(1 - \frac{2t}{D_{avg}}\right)^3, \quad (4.29)$$

where $T_B(0)$ is the blocking temperature without the disordered layer. The value of t for the γ -Fe₂O₃ NPs embedded in an amorphous SiO₂ matrix was measured to be 1.25 ± 0.07 nm using a Faraday rotation technique [89]. Moreover, this value is not changed significantly for all γ -Fe₂O₃ NPs with the average diameter in the range $6.2 \text{ nm} \leq D_{avg} \leq 21.8 \text{ nm}$ where our NPs' diameter (12.4 nm) falls. Applying Eqn. 4.29 with $T_B(0) = 160$ K, $D_{avg} = 12.4$ nm, and $t = 1.25$ nm, the blocking temperature of Au/SiO₂ doubly coated γ -Fe₂O₃ NPs is 81 K, which is in excellent agreement with the experimental data 85 K. The second reason for the decrease in T_B with coating is the reduction of the strength of the magnetic dipole-dipole interaction. From a Monte Carlo simulation, it was found that the T_B is proportional to the strength of the dipole-dipole interaction. This dipole-dipole interaction is proportional to the magnitude of dipole moments and inversely proportional to the distance between the related dipoles. The decrease of dipole moments for the coated NPs is easy to understand because the coating induces the disordered layer at the surface of the γ -Fe₂O₃ core. The Au/SiO₂ coating also makes the distance between magnetic cores farther. Thus, the dipole-dipole interaction becomes weaker with the diamagnetic coating, and it causes the blocking temperature to decrease.

The field dependence of magnetization of pure γ -Fe₂O₃ and Au/SiO₂ coated NPs is shown in Fig. 4.10. The field changed from 0 T to 5 T to

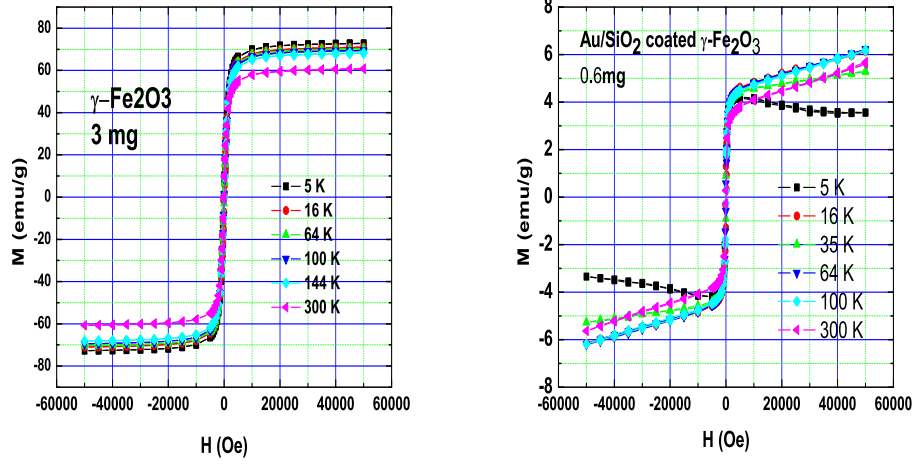


Figure 4.10: Field dependence of magnetization of pure and Au/SiO₂ coated γ -Fe₂O₃ at various temperatures.

–5 T and to 5 T again. The coated one is obtained after background subtraction from the raw data. The raw data and the corresponding background data can be found in Fig. 4.8. Overall, magnetization of pure NPs is bigger than coated ones for each temperature, and the saturation field of pure NPs decreases monotonically with increasing temperature as expected. The saturation magnetic moment at 5 K is 73 emu/g with 5 T applied field which corresponds to $2.07 \mu_B$ per formula unit (f.u.) or $1.04 \mu_B/\text{Fe}^{3+}$. This value is about 83% of the resultant moment ($1.25 \mu_B/\text{Fe}^{3+}$) of the bulk γ -Fe₂O₃ [9]. The apparent (high-field) saturation magnetization decreases from 73 emu/g to 61 emu/g with decreasing temperature from 5 K to 300 K. For the coated one, the M_{sat} is about 5.6 emu/g at 300 K and 5 T, which is about 7.7% of pure one. This decrease is obviously from the increase in mass due to dia-

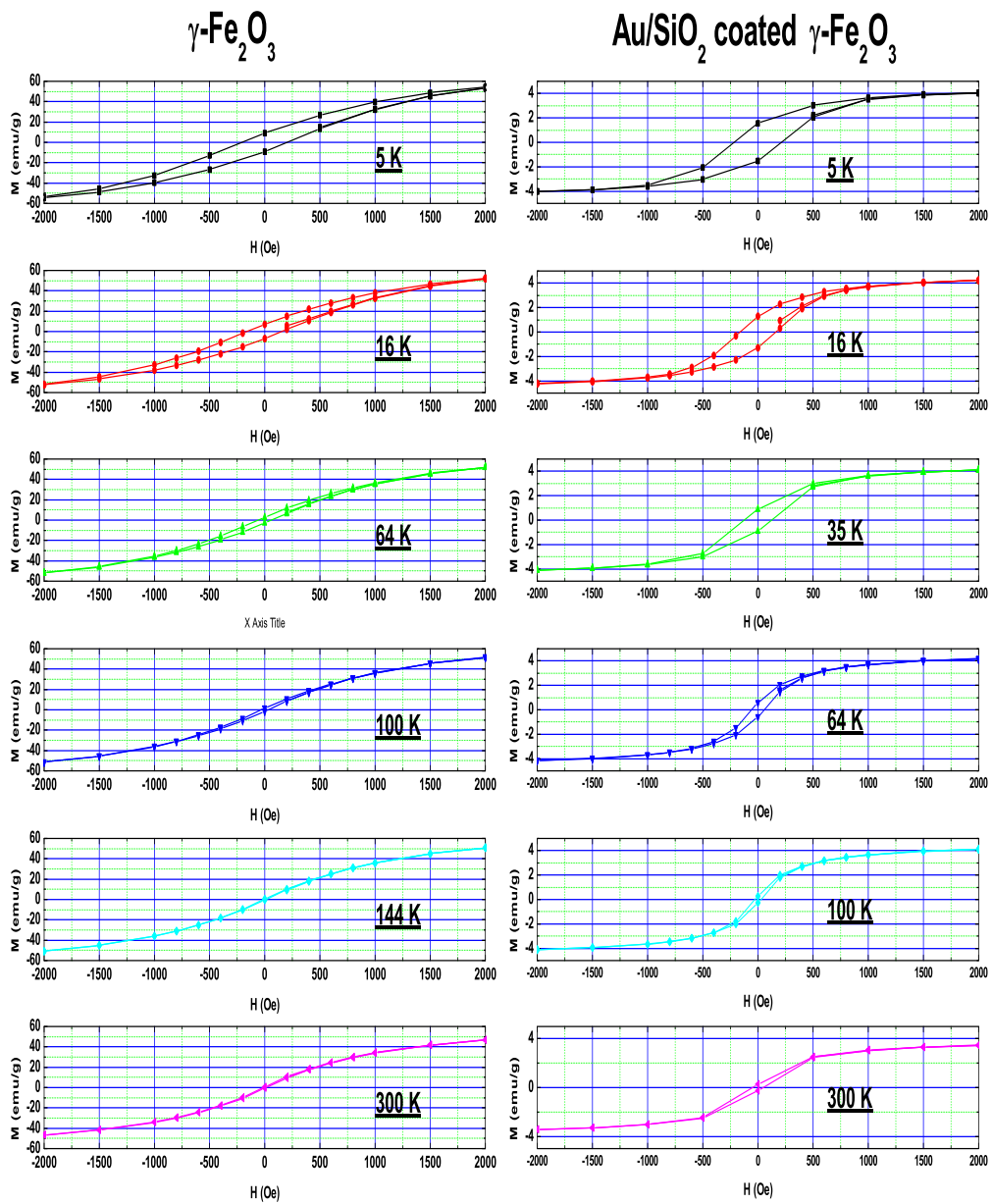


Figure 4.11: Field dependence of magnetization of pure and Au/SiO₂ coated $\gamma\text{-Fe}_2\text{O}_3$ at various temperatures.

magnetic coating materials, Au and SiO₂. However, this saturation moment does not change monotonically with temperature, because the measurements were not performed at the same time. That is, the measurements at 5 K, 35 K and 300 K were done first and the others followed next after a few other measurements, which made the SQUID parameter different for the two sets of measurements. However, if we see each set of data, the saturation magnetization decreases with increasing temperature, and even after background subtraction the magnetic moment at 5 K decreases with increasing applied field, which shows diamagnetic behavior. This could be from the difficulty in finding the exact background signal due to the paramagnetic defect of the capsule which is different for each capsule.

To see the hysteresis more clearly, Fig. 4.10 is enlarged in Fig. 4.11 with the applied field in the range between -2000 Oe to 2000 Oe. The irreversibility was not found above 2000 Oe or below -2000 Oe. From Fig. 4.11, the magnetization of pure NPs is found to be totally reversible and superparamagnetic only for the temperature range above 100 K, but the coated one has a very small hysteresis even at 300 K whose magnitude is around ± 50 Oe. The source of this hysteresis could be from the SQUID magnet or from the diamagnetic coating, but we need more data at the range to make a clear determination. Another effect of coating is the decrease in H_{irr} , which is defined as the magnetic field where the irreversibility starts. For example, H_{irr} at 5 K is about 2000 Oe for the pure one but it reduced to 1000 Oe for the coated one.

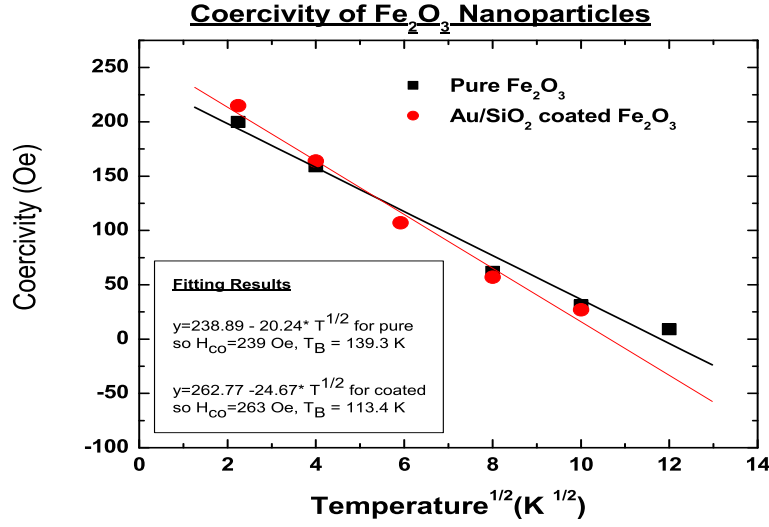


Figure 4.12: Coercivity versus Temperature^{1/2} for pure and coated NPs. The solid and dotted line shows fits with Equ. 4.30.

The coercivity is known to be proportional to the square root of temperature as [50, 103]

$$\frac{H_C}{H_{C0}} = 1 - \left(\frac{T}{T_B}\right)^{1/2}, \quad (4.30)$$

where H_{C0} is the coercivity at 0 K. Figure 4.12 shows the plot of the coercivity of pure and coated NPs versus the square root of temperature where the coercivity was found from the hysteresis graph of Fig. 4.11. Fits were done using Eqn. 4.30 and added to the figure. The data looks slightly off the fitting line but it is clear that the slope of coated one is steeper than the pure one, and such a deviation from linearity has been observed for SiO₂ coated γ -Fe₂O₃ NPs [107]. We found $H_{C0} = 239$ Oe and $T_B = 139$ K for the pure NPs and $H_{C0} = 263$ Oe and $T_B = 113$ K for the coated ones. The fitting shows the

blocking temperature decrease with coating which is consistent with the result of ZFC magnetization curve in Fig. 4.9. It is interesting to note that H_C is increased by the coating only below 50 K but above 50 K, H_C of the coated NPs is slightly smaller than that of the pure ones.

In summary, the coating of γ -Fe₂O₃ NPs with Au/SiO₂ decreases the blocking temperature from 160 K to 80 K. This is explained well with the reduction of the effective volume of the γ -Fe₂O₃ core. From the hysteresis graph, the uncoated NPs are found to be superparamagnetic and the coated NPs are found to be almost superparamagnetic above 100 K. The coercivities of the pure and the coated γ -Fe₂O₃ decrease linearly with the square root of temperature, and H_C for the pure NPs is found to go down faster than for the coated ones, which confirms the blocking temperature for the pure NPs is larger than for the coated ones.

Chapter 5

Results and Discussion of $\text{Ca}_{2+x}\text{Y}_{2-x}\text{Cu}_5\text{O}_{10-\delta}$

5.1 Sample analysis

5.1.1 x-ray diffraction

The phase of all samples was identified by a powder x-ray diffraction method with Cu $K\alpha$ radiation. The first graph of Fig. 5.1 shows the x-ray patterns of the parent compounds for different oxygen annealing procedures. The samples with no oxygen annealing and with 1 atm oxygen anneal show a good single phase of $\text{Ca}_2\text{Y}_2\text{Cu}_5\text{O}_{10-\delta}$, but a small (less than 5%) multi-phase signal from $\text{Cu}_2\text{Y}_2\text{O}_5$ appears for the 170 atm O_2 anneal (circles). A similar impurity was found during a previous experiment with high pressure (215 atm) oxygen annealing [39]. The impurity causes a lower-temperature peak in a magnetic susceptibility data which will be discussed in the next section. Ca-doped samples with $x = 0.5, 0.75, 0.9,$ and 1.0 show a single phase even though they were annealed under different oxygen pressures up to 170 atm. X-ray patterns of the samples with $x = 0.75$ and 1.0 are illustrated in the second and the third graph of Fig. 5.1, respectively. From the figure, we can not see a big difference in these peaks for the different Ca-doping values and oxygen pressures, which mean Ca-doping and oxygen deficiency induce no structural transition.

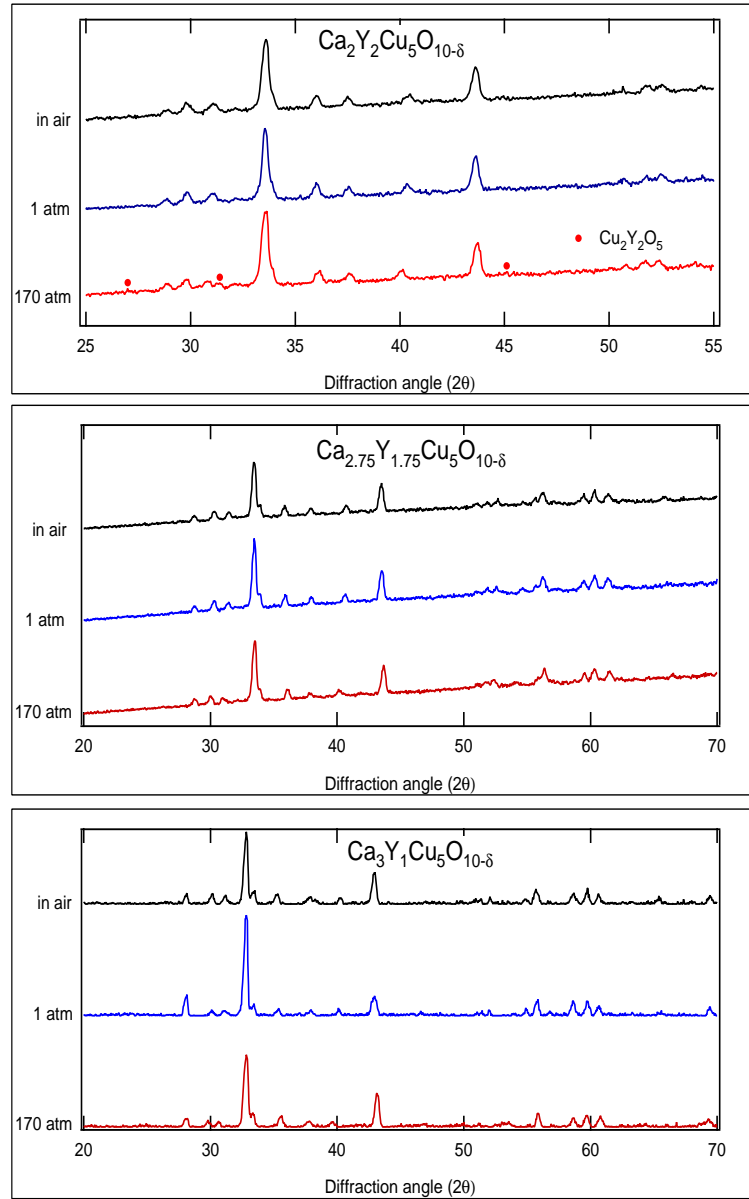


Figure 5.1: X-ray diffraction patterns of $\text{Ca}_{2+x}\text{Y}_{2-x}\text{Cu}_5\text{O}_{10-\delta}$ for $x = 0, 0.75$ and 1.0 , for different oxygen annealing procedures. The raw data for $x = 0$ and 0.75 , and the data after a smooth background subtraction for $x = 1.0$. The impurity signal from $\text{Cu}_2\text{Y}_2\text{O}_5$ is marked with circles.

For higher doped samples of $x = 1.25$ and 1.5 we failed to make a single phase without oxygen annealing nor with 1 atm oxygen annealing in the tube furnace. Also a single phase was not obtained for those samples under the oxygen pressure more than 217 atm. Signals due to defects can be seen in Fig. 5.2 for the samples annealed at oxygen pressures below 1 atm and above 217 atm. These results are contrary to those of Hayashi *et al* [39] where a single phase was reported under 215 bar oxygen pressure. This may be because our sample, which was not wrapped with Au foil, interacts with the Al_2O_3 boat at high oxygen pressures and at high temperatures. However, the oxygen pressure in the annealing procedures is confirmed to be critical in making single phases of this system from both results, specifically for samples with $x \geq 1.25$.

From the x-ray data, the lattice parameters were calculated using Jade 7.0 software. Figure 5.3 summarizes the lattice parameters for the different Ca-dopings and the oxygen deficiencies. The oxygen deficiencies are determined from iodometric titration (detailed procedures are explained in Appendix A), the results are summarized in Table 5.1. All lattice parameters were indexed on the basis of an orthorhombic Fmmm subcell. The averages of lattice parameters were found to be $a \sim 2.82 \text{ \AA}$, $b \sim 6.22 \text{ \AA}$, and $c \sim 10.58 \text{ \AA}$, which are similar to the results from the previous experiments [39, 61].

The parameter b increases with increasing Ca-doping, which was also seen in the previous data [39, 61]. This increase is due to the larger Ca^{2+} (ionic radius = 0.99 \AA compared to Y^{3+} , which has a radius of 0.92 \AA) increasing the

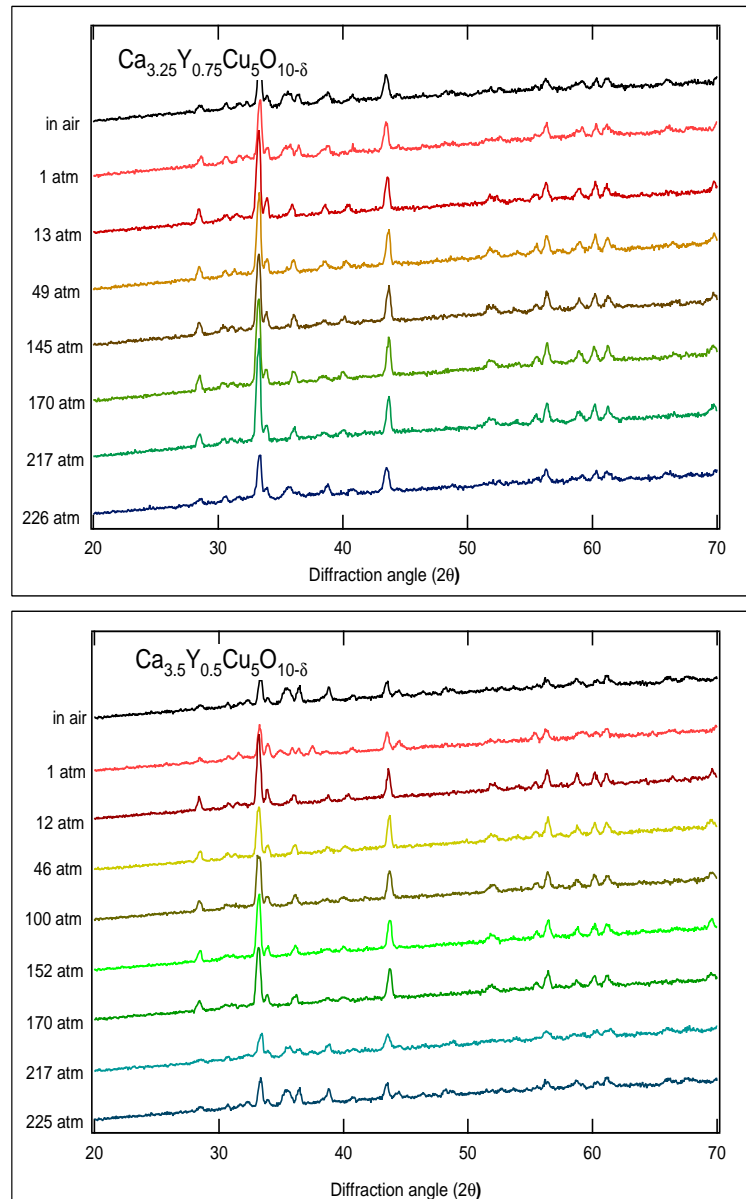


Figure 5.2: X-ray diffraction patterns of $x = 1.25$ and 1.5 for different oxygen annealing procedures.

Lattice Parameters a, b, and c of $\text{Ca}_{2+x}\text{Y}_{2-x}\text{Cu}_5\text{O}_{10-\delta}$

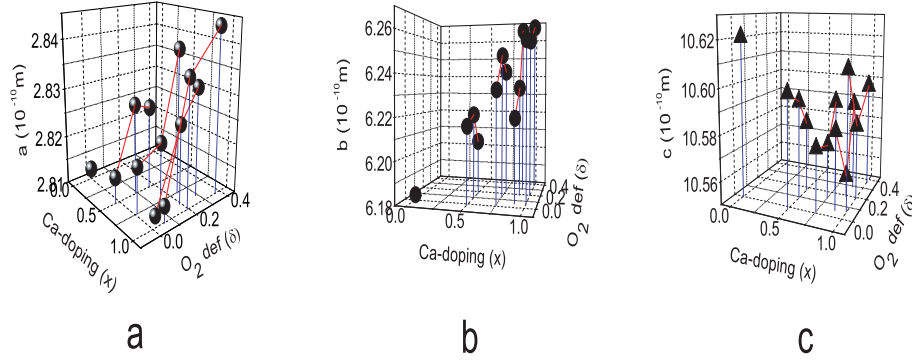


Figure 5.3: Dependence of lattice parameters on Ca-doping and oxygen deficiency.

distance between the planes where the CuO_2 chains are embedded. However, the parameter a , interestingly, increases with increasing oxygen deficiency because the vacancy induced with oxygen deficiency makes Cu-O-Cu bond angle wider and adds electrons to bonds.

5.1.2 Iodometric titration

Iodometric titration was utilized to find the oxygen content of each sample, and the results are summarized in Table 5.1. First, we can see that increasing the oxygen pressure during the annealing procedure reduces the oxygen deficiency for each Ca-doped sample, as anticipated. It is interesting to note that the oxygen deficiency increased for the Ca doped samples from $x = 0$ to $x = 1.0$ with no oxygen annealing procedure, that is, from $\delta = 0$ for $x = 0$ to $\delta = 0.37$ for $x = 1.0$. This is because the Ca ion doped hole loosens one

Table 5.1: Titration results for $\text{Ca}_{2+x}\text{Y}_{2-x}\text{Cu}_5\text{O}_{10-\delta}$.

	air 1 atm		O_2 1 atm		O_2 170 atm	
	δ	p	δ	p	δ	p
$x = 0$	0	0	\times^1		\times^1	
$x = 0.5$	0.17	0.16	0.09	0.32	-0.02 ²	0.54
$x = 0.75$	0.24	0.27	0.14	0.47	0.01	0.73
$x = 0.9$	0.29	0.32	0.19	0.52	0.05	0.80
$x = 1.0$	0.37	0.26	0.19	0.62	0.04	0.92
$x = 1.25$		\times^1		\times^1	0.08	1.09
$x = 1.5$		\times^1		\times^1	0.06 ²	1.13

¹ Failed to make a single phase

² Annealed at 176 atm

of the oxygen-copper bonds, thus the oxygen ion can be removed more easily from the chain. The increase in oxygen deficiency with increasing hole doping was also found in other hole-dopable compounds such as $\text{La}_{2-x}\text{Sr}_x\text{CuO}_{4-\delta}$ [31, 95] and $\text{La}_{1-x}\text{Sr}_x\text{MnO}_{3-\delta}$ [93]. The pattern of oxygen deficiency in the samples with no annealing procedure could be applied to the oxygen annealed samples with 1 atm O_2 and 170 atm O_2 pressures, respectively. That is, the more the Ca-doping the more the oxygen deficiency, as shown in Table 5.1. [83]

5.2 Magnetic susceptibility

The temperature dependence of magnetic susceptibility for all $\text{Ca}_{2+x}\text{Y}_{2-x}\text{Cu}_5\text{O}_{10-\delta}$ (CaYCuO) is shown in Fig. 5.4. For the parent compounds ($x = 0$) with different oxygen deficiencies, a two-peak feature in the magnetic susceptibility becomes clear, as the oxygen pressure increases. The lower peak is found, with the help of x-ray diffraction data, to come from the magnetic

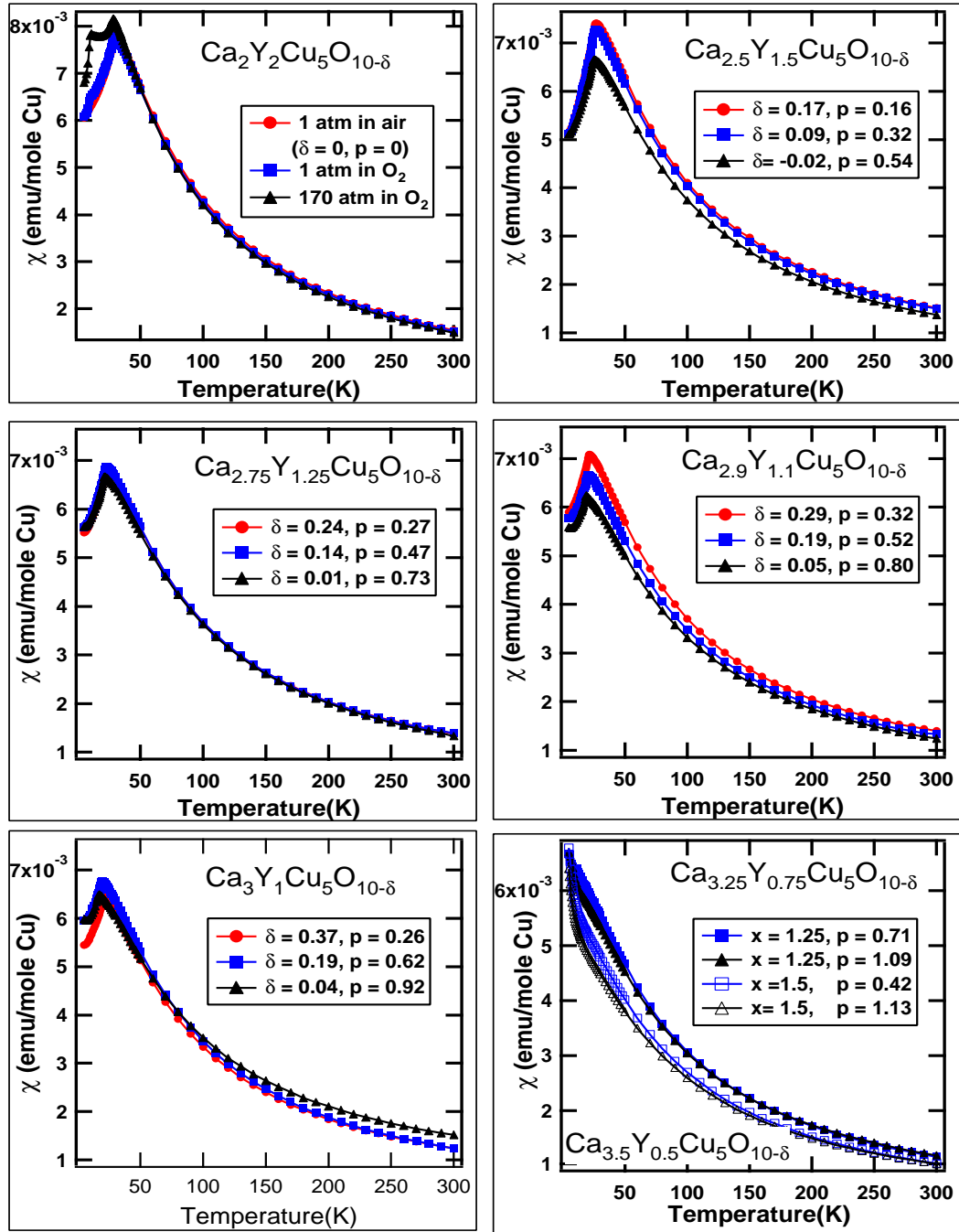


Figure 5.4: Temperature dependence of magnetic susceptibility for all samples

defect $\text{Cu}_2\text{Y}_2\text{O}_5$. Even though this peak is small (less than 5%) at 170 atm, the highly magnetic defect can have a large effect on the magnetic signal. An analogous signal was reported for the same compound; it was only a 1% magnetic defect [39]. So, the parent compounds are found to be over-oxygenated and, from the magnetic susceptibility data, begin to fail to make a single phase at 1 atm oxygen pressure.

The samples with $x = 0.5$ through $x = 1.0$ show a typical 3D long-range antiferromagnetic phase transition. For the fully oxygenated samples with different x , Néel temperatures shift lower and the height of the peaks generally decreases with increasing the Ca-doping level (x). For a fixed x , the Néel temperature and the overall magnitude of the magnetic susceptibility decreases with decreasing oxygen deficiency. The Néel temperatures are summarized in Table 5.2. The low temperature downturn of magnetic susceptibility disappears for the sample with $x = 1.25$ and the susceptibility shows an upturn for the sample with $x = 1.5$, which shows that these systems are not 3D long-range antiferromagnets any more.

Figure 5.5 shows the magnetic susceptibilities of $x = 1.25$ and 1.50 samples with various oxygen pressures. The multiphase samples of both $x = 1.25$ and 1.50 have a relatively small magnitude of magnetic susceptibility and show a downturn at around 20 K. From the enlarged figure of the single phase, $x = 1.25$ sample, the magnetic susceptibility shows a downturn around 8 K, for the sample with 45 atm of oxygen pressure, and this downturn disappears above 145 atm of oxygen pressure. All single phase data for $x = 1.50$ samples,

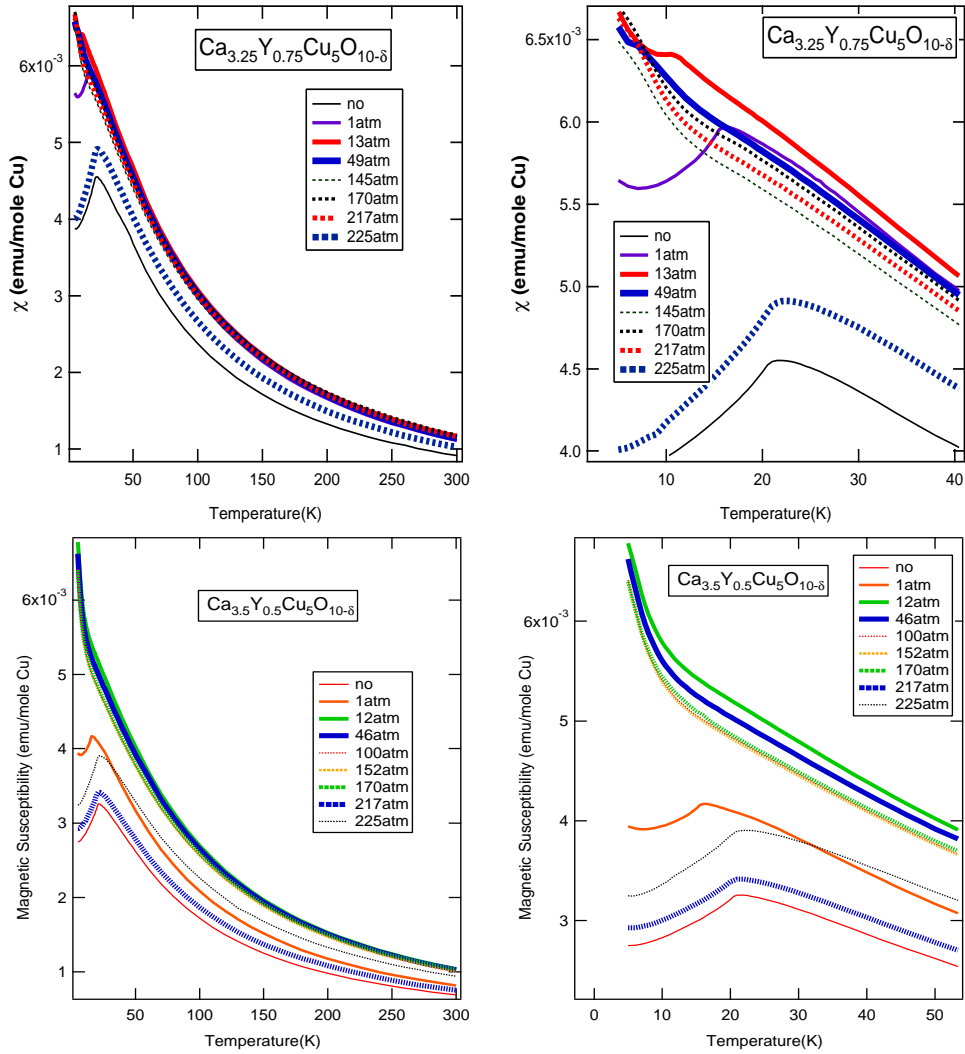


Figure 5.5: Magnetic susceptibilities and their enlargements of $x = 1.25$ and 1.5 samples with different oxygen annealing pressures.

Table 5.2: Magnetic parameters of $\text{Ca}_{2+x}\text{Y}_{2-x}\text{Cu}_5\text{O}_{10-\delta}$ including Néel temperature, effective magnetic moment, and the Curie-Weiss temperature.

		$T_N^*(\text{K})^1$	$T_N(\text{K})^2$	$\mu_{eff}(\mu_B)$	$ \Theta (\text{K})$
$x = 0$	$p = 0$	29.5	28.9	2.29	39.8
	$p = 0.16$	27	24.8	2.26	43.9
$x = 0.5$	$p = 0.32$	26	24.5	2.21	41.9
	$p = 0.54$	25.5	23.4	2.18	45.6
	$p = 0.27$	23.5	21.9	2.09	41.2
$x = 0.75$	$p = 0.47$	23	21.5	2.07	39.0
	$p = 0.73$	21.5	20.5	2.15	47.2
	$p = 0.32$	21.5	20.1	2.08	39.4
$x = 0.9$	$p = 0.52$	20.5	19.4	2.01	39.6
	$p = 0.80$	19	17.7	2.07	48.7
	$p = 0.26$	21	19.8	2.01	42.2
$x = 1.0$	$p = 0.62$	19.5	18.3	2.09	43.9
	$p = 0.92$	17	16	2.05	49.8
$x = 1.25$	\times	10.5	13	1.96	46.4
	$p = 1.09$	\times	10	2.00	53.6
$x = 1.5$	\times	\times	\times	1.87	51.4
	$p = 1.13$	\times	\times	1.85	55.4

¹ From the downturn the magnetic susceptibility data

² From the downturn the heat capacity data

which were annealed under 12 atm through 170 atm pressure, show an upturn around 13 K.

Therefore, we find that the long-range antiferromagnetic transition disappears between $x = 1.0$ and $x = 1.25$, but we need to know the temperature dependence of specific heat to understand the details of the transition.

The Curie-Weiss temperatures and effective magnetic moments can be

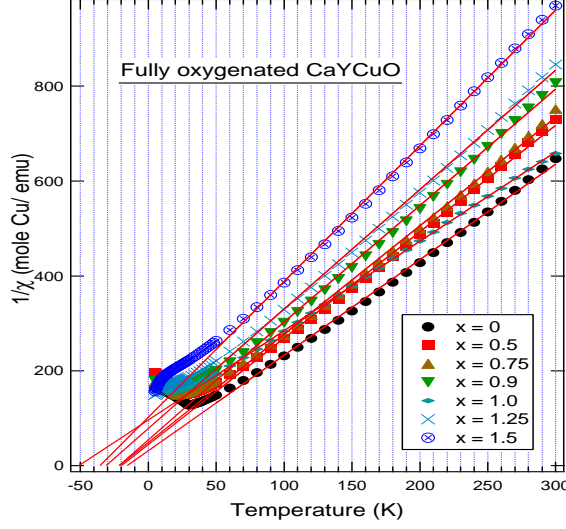


Figure 5.6: Inverse of magnetic susceptibility versus temperature for the fully oxygenated samples. Solid lines are from the fitting with Curie-Weiss law above 75 K.

found from fitting to the Curie-Weiss law,

$$\chi = \chi_0 + \frac{N_A \mu_{eff}^2}{3k_B(T - \Theta)}, \quad (5.1)$$

where N_A is Avogadro's number, k_B is Boltzmann's constant, Θ is the Curie-Weiss temperature, and the effective magnetic moment is $\mu_{eff} = g\sqrt{S(S+1)}\mu_B$.

Figure 5.6 shows the temperature dependence of the inverse of magnetic susceptibility for the fully oxygenated samples. The straight lines represent the fit with Eqn. 5.1 for the data above 75 K. From this graph, we find that CaY-CuO follows the Curie-Weiss law well for the temperature range, even though holes are induced into the CuO_2 chain by substituting Ca^{2+} for Y^{3+} . Figure 5.7 shows the fitting results with the data sets in the temperature ranges starting

from 50 K, 75 K, 100 K, 125 K and 150 K to 300 K. The Curie-Weiss law explains the magnetic behavior in the paramagnetic phase and thus it should be applied for temperatures higher than the Néel temperature. However, the small amount of data at high temperatures can distort the magnetic behavior so we need to consider a good amount of data to get a reasonable fit and the data should be from temperatures high enough to be in paramagnetic region.

Effective magnetic moments of fully oxygenated samples generally decrease with increasing hole doping (see the data connected with solid lines in Fig. 5.7). Ca^{2+} ions that have displaced Y^{3+} ions induce holes onto O^{2-} ions where the spin of the hole is coupled to the spin of the electron of Cu^{2+} antiferromagnetically. This coupling, which is called Zhang-Rice singlet, reduces the average effective magnetic moment of the system. The oxygen deficiency (δ) for a given cation doping (x) is often assumed to reduce the hole doping (p) according to $p = x - 2\delta$, and so it reduces the effective magnetic moment. However, the dependence of effective magnetic moment on oxygen deficiency is not clear from Fig. 5.7. It is interesting to note that for a given hole doping (p), the more Ca-doped samples show less effective magnetic moment. That is, the induced hole from Ca-doping reduces the average magnetic moment more effectively than from oxygen deficiency. The Curie-Weiss temperature ($|\Theta|$) shows negative numbers for all samples regardless of oxygen deficiency. For the fully oxygenated samples, $|\Theta|$ generally increases with increasing hole doping level. As oxygen deficiency is increased, $|\Theta|$ shows a decreasing trend for a given x .

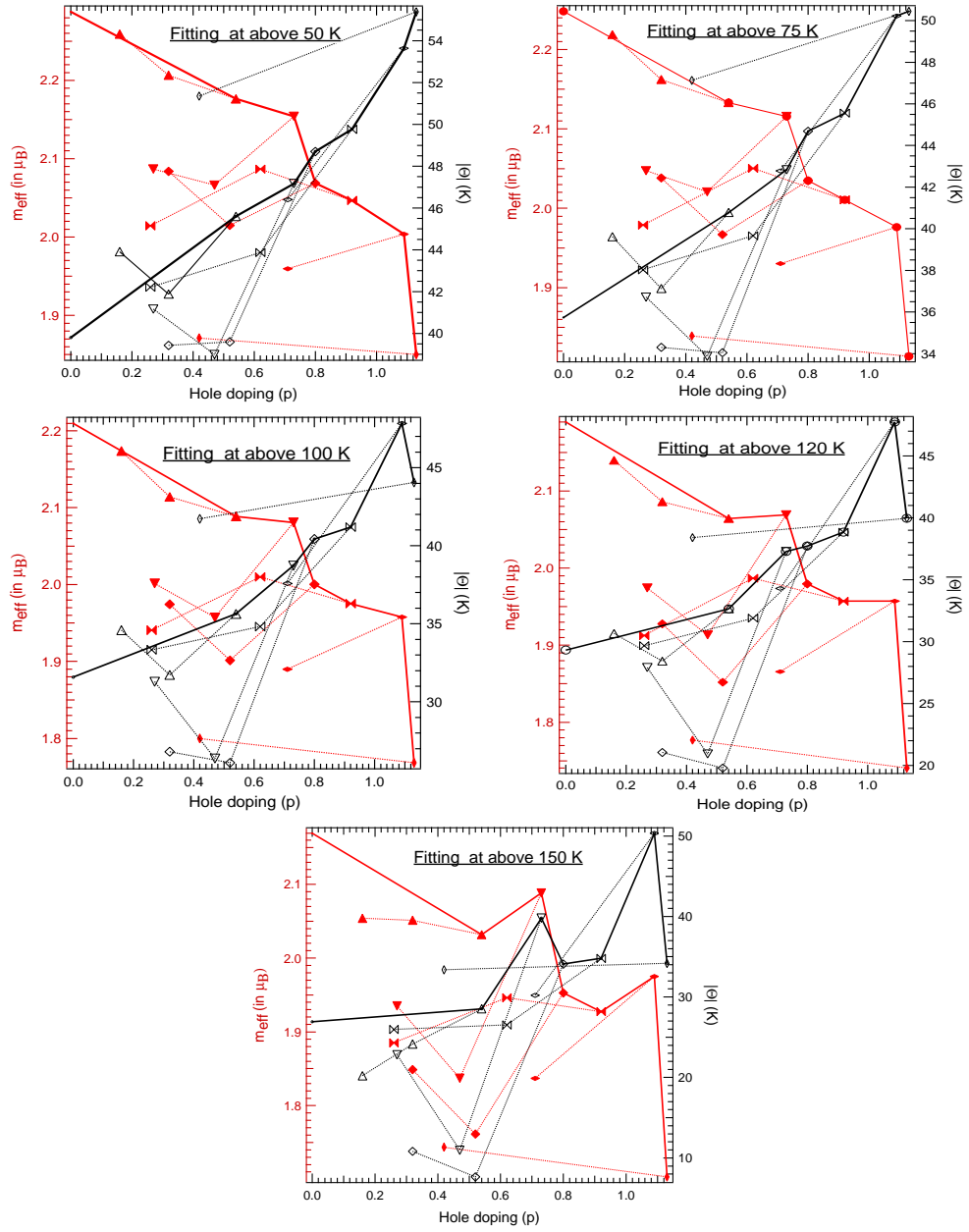


Figure 5.7: Effective magnetic moments and the Curie-Weiss temperatures using Eq. 5.1 at different temperature ranges. The data connected with the solid lines are from fully oxygenated samples. The data from oxygen deficient samples are connected by dotted lines.

The effective magnetic moment and the Curie-Weiss temperature of the parent compound ($x = 0$) were obtained in previous work using both single crystal and polycrystal samples at high temperature data ($T \geq 150K$): $\mu_{eff} = 1.95$, $|\Theta| = 4.5$ [39], $\mu_{eff,a} = 2.00$, $\mu_{eff,b} = 2.19$, $\mu_{eff,c} = 2.02$, $|\Theta_a| = 13.7$, $|\Theta_b| = 13.7$, $|\Theta_c| = 16.2$ ($\mu_{eff,avg} = 2.07$, $|\Theta_{avg}| = 14.5$) [117], $\mu_{eff,a} = 1.84$, $\mu_{eff,b} = 2.07$, $\mu_{eff,c} = 1.82$ ($\mu_{eff,avg} = 1.91$ and $|\Theta_{avg}| = 8$) [61] (the effective moment (μ_{eff}) in units of μ_B , and the Curie-Weiss temperature ($|\Theta|$) in K). The values are smaller than our fitting results even for the 150 K temperature data set (see the last graph of Fig. 5.1). For reference, the calculated magnetic moments of Cu^{2+} ion, whose configuration is $3d^9$ and basic level is $^2D_{5/2}$, are 3.55 using $g\sqrt{J(J+1)}$ and 1.73 using $g\sqrt{S(S+1)}$ [60].

5.3 Specific heat

The temperature dependence of specific heat is shown in Fig. 5.8 for the samples of CaYCuO . To clarify the effects of oxygen deficiency, the samples with different oxygen deficiencies were displayed on the same graph for the same Ca-doping. A λ -shaped peak is clear for all the samples with $x = 0$ through 1.0 that were annealed in air, which indicates the 3D long range antiferromagnetic order. The peak is smeared and shifted to lower temperatures with increased Ca-doping as in the previous data [61]. For fully oxygenated samples with different Ca-doping's, the overall magnitude of specific heat is smaller than the oxygen deficient samples. The peak is also shifted to the left and it changes to a broad bump at $x = 1.0$ and finally disappears at $x = 1.25$.

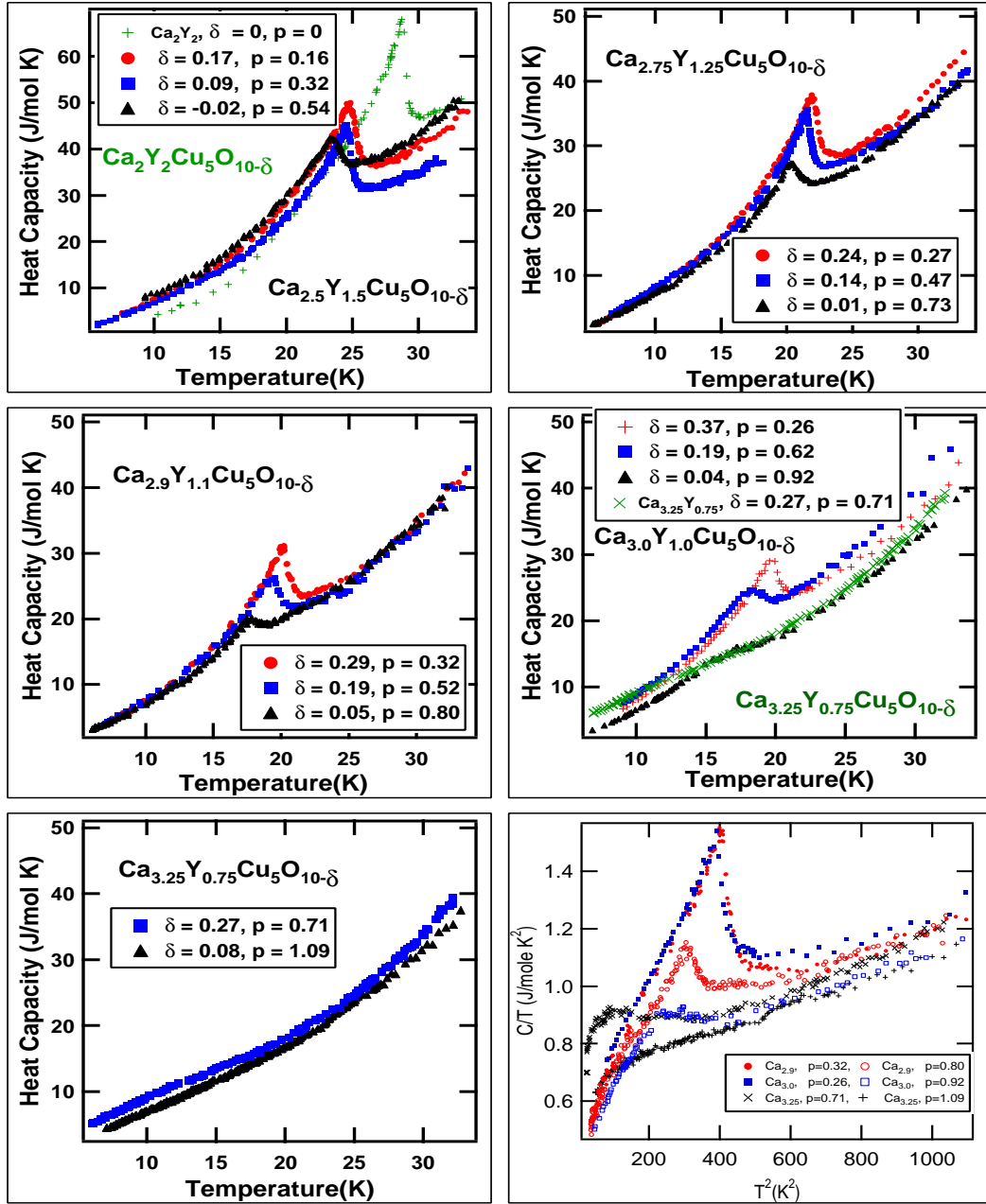


Figure 5.8: Temperature dependence of the specific heat of CaYCuO for different oxygen deficiencies. The last figure shows C/T versus T^2 of $x = 0.9, 1.0$ and 1.25 .

Also, the peaks for the samples with the same Ca-doping (the same x value) show the same feature with decreasing oxygen deficiency as expected from the often-assumed relation $p = x - 2\delta$. Therefore, the oxygen deficiency is also found to change the magnetic interaction in the same way as Ca-ion doping. This kind of feature is typical in systems where a long range 3D interaction changes to a lower-dimensional and short-range interaction [91]. The peak temperatures are summarized in Table 5.2. The last graph of Fig. 5.8 shows C/T vs. T^2 to illustrate the relationship between the peak shape and the hole doping. The suppression of the peak is clear for hole-doping using either Ca-doping or oxygen deficiency.

To find the contribution of magnetic excitations to the specific heat, we subtract the phonon contribution from the measured data assuming the phonon contribution follows $C_{phonon} = \beta T^3$ where $\beta = 0.001$ J/mol/K⁴ [11], shown in Fig. 5.9. We try to fit the spin contribution to the specific heat with the dimer, Ising, and Heisenberg chain models to find the exchange coupling constant. We used the following equations for each fitting: dimer [10]

$$C(T/J) = A * \frac{12R(J/k_B T)^2 * \exp(J/k_B T)}{(1 + 3 * \exp(J/tp))^2}, \quad (5.2)$$

Ising [10]

$$C(T/J) = A * \frac{(-J/T)^2}{(\cosh(-J/T))^2}, \quad (5.3)$$

Heisenberg chain [54]

$$C(T/J) = 0.75 * \left(\frac{3}{16(T/J)^2} P_{(9)}^{(6)}(T) - F(T) \right), \quad (5.4)$$

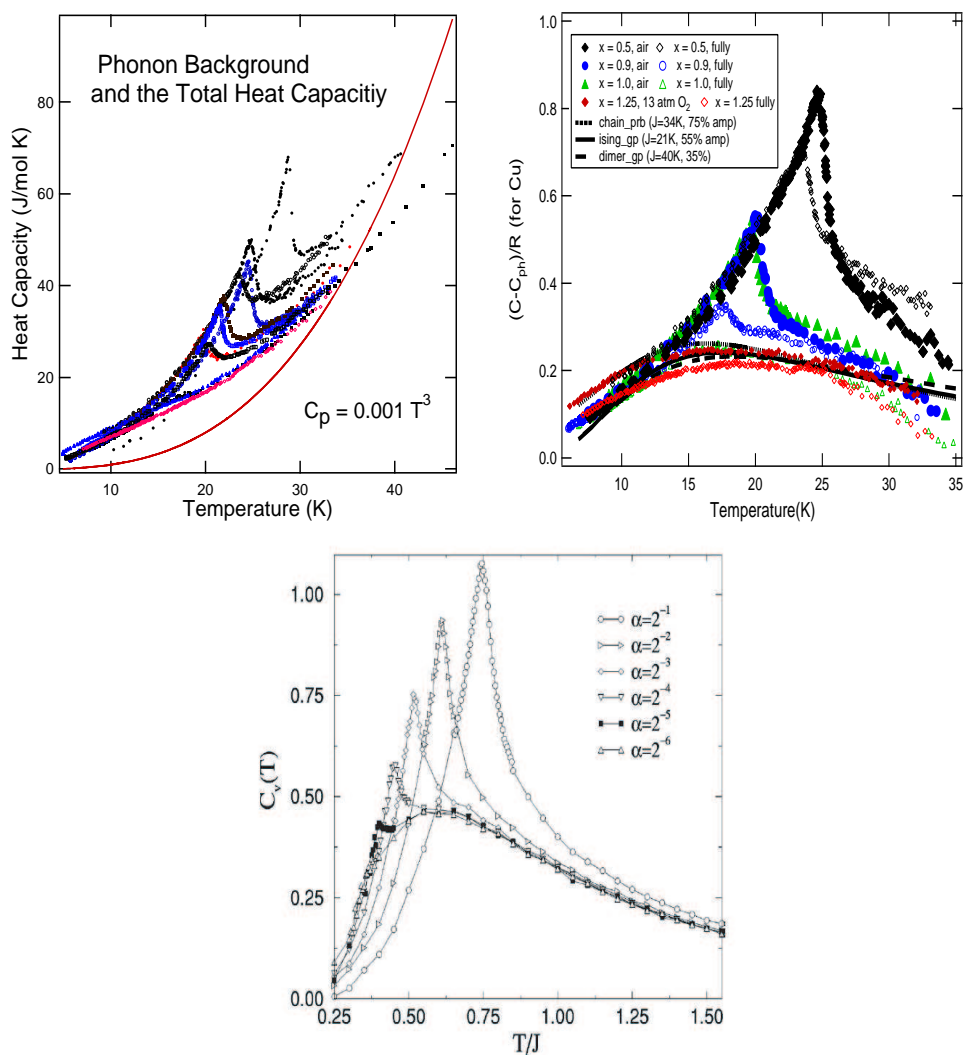


Figure 5.9: Specific heat of two contributions, phonon and spin. The red line in the first graph shows the phonon contribution. The second graph shows the spin contribution with fits using dimer, Ising, and Heisenberg chain models. The last graph shows Quantum Monte Carlo simulation results for the dimensional transition from 3D to 2D of specific heat where $\alpha = J_{\perp}/J_{plane}$ [91]

where

$$P_{(9)}^{(6)}(T/J) = \frac{1 + [\sum_{n=1}^6 N_n/(T/J)^n]}{1 + [\sum_{n=1}^6 D_n/(T/J)^n]}$$

$$F(T/J) = a_1(T/J) \sin\left(\frac{2\pi}{a_2 + a_3(T/J)}\right) e^{a_4(T/J)} + a_5(T/J) e^{a_6(T/J)}$$

Here the fitted parameters used are: $N_1 = -0.018891$, $N_2 = 0.024710$, $N_3 = -0.003709$, $N_4 = 0.003016$, $N_5 = -0.000379$, $N_6 = 0.000043$, $D_1 = -0.518891$, $D_2 = 0.596576$, $D_3 = -0.151173$, $D_4 = 0.074445$, $D_5 = -0.002480$, $D_6 = -0.000536$, $D_7 = 0.000820$, $D_8 = -0.000108$, $D_9 = 0.000012$, $a_1 = -0.000016$, $a_2 = 0.013021$, $a_3 = 0.004328$, $a_4 = 49.422168$, $a_5 = 0.000402$, $a_6 = 325.22706$.

We found $J = 21$ K from the Ising model, 40 K from the dimer model, and 34 K from the Heisenberg chain model for the $x = 1.25$ sample annealed under 13 atm oxygen pressure. Neutron scattering experiments [71] claimed $J = 80$ K for all x , with other exchange coupling constants in addition to the nearest neighbor's exchange coupling J . These explain the 3D behavior of the samples with low x . This 3D behavior changes to 2D or 1D with hole doping, and the specific heat behavior of the 3D to 2D coupling transition is illustrated by using a Quantum Monte Carlo simulation as shown in Fig. 5.9 [91].

5.4 Discussion

From the results of magnetic susceptibility and of heat capacity measurements, a magnetic phase diagram was created in Fig. 5.10, where the hole doping includes both Ca-doping and oxygen deficiency effects. The upper

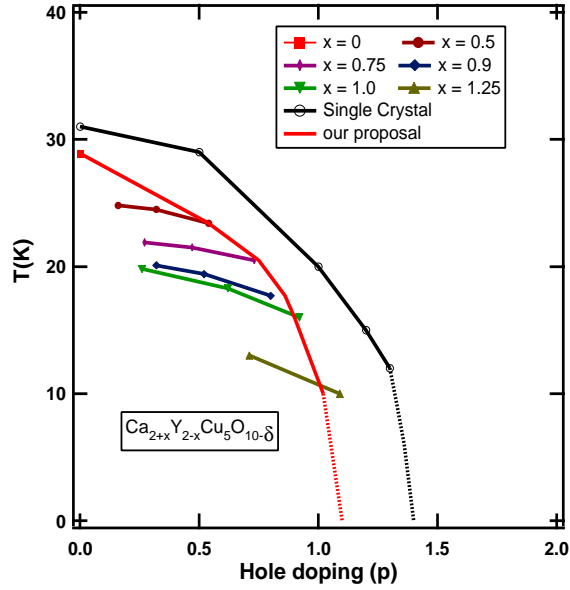


Figure 5.10: Magnetic phase diagram where hole doping dependence considers both Ca-doping and oxygen deficiency. Single crystal data from prior experiment [61].

(right) solid line shows a previous phase diagram from single crystals measurements [61], and the lower (left) solid line is proposed from our experimental results. Apparently, single crystal data was obtained from oxygen deficient samples where hole doping was overestimated. Therefore, the phase diagram of CaYCuO should be shifted to the left for the fully oxygenated samples (red line), and the antiferromagnetic transition is fully suppressed around $p = 1.0$ (not around $p = 1.4$, as previously proposed).

Each colored line on the graph shows the dependence of Néel temperature on oxygen deficiency for a given Ca-doping level (x). The Néel tem-

perature changes even for samples with the same amount of Ca-doping due to the effects of oxygen deficiency. This is expected, because the hole doping (p) is related by two factors, Ca-doping (x) and oxygen deficiency (δ), often assumed to simply obey the charge-counting relation $p = x - 2\delta$. However, the Néel temperature (T_N) is not the same for the same hole doping (p). For example, for $p = 0.5$, $T_N = 24.1, 21.6, 19.8,$ and 19.2 for each sample $x = 0.5, 0.75, 0.9,$ and 1.0 , respectively. That is, the Néel temperature decreases with increasing oxygen deficiency even for the same hole doping. Therefore, oxygen deficiency reduces the Néel temperature more than Ca-doping.

The decrease of Néel temperature may be due to the decrease in the magnetic moments, the decrease in the magnetic coupling or the changes in magnetic ordering from 3D long-range order to short-range order or all of these. The classical mean field theory [60] predicts that the Néel temperature follows

$$T_N = \frac{2JzS(S+1)}{3k_B} \sim Jz\mu_{eff}^2, \quad (5.5)$$

where J is the exchange coupling, z is the number of the nearest neighbors, and S is the spin (here, $1/2$).

Figure 5.11 shows the Néel temperature, the Curie-Weiss temperature, and the effective magnetic moment of CaYCuO samples for $x = 0$ through 1.0 with different oxygen deficiencies. The solid marks describe the data from the fully oxygenated samples. From the first and the fourth graphs, T_N and $T_N/|\Theta|$ are proportional to μ_{eff}^2 and p for the fully oxygenated samples, respectively. The second and the third graphs show that T_N/μ_{eff}^2 and T_N decrease with

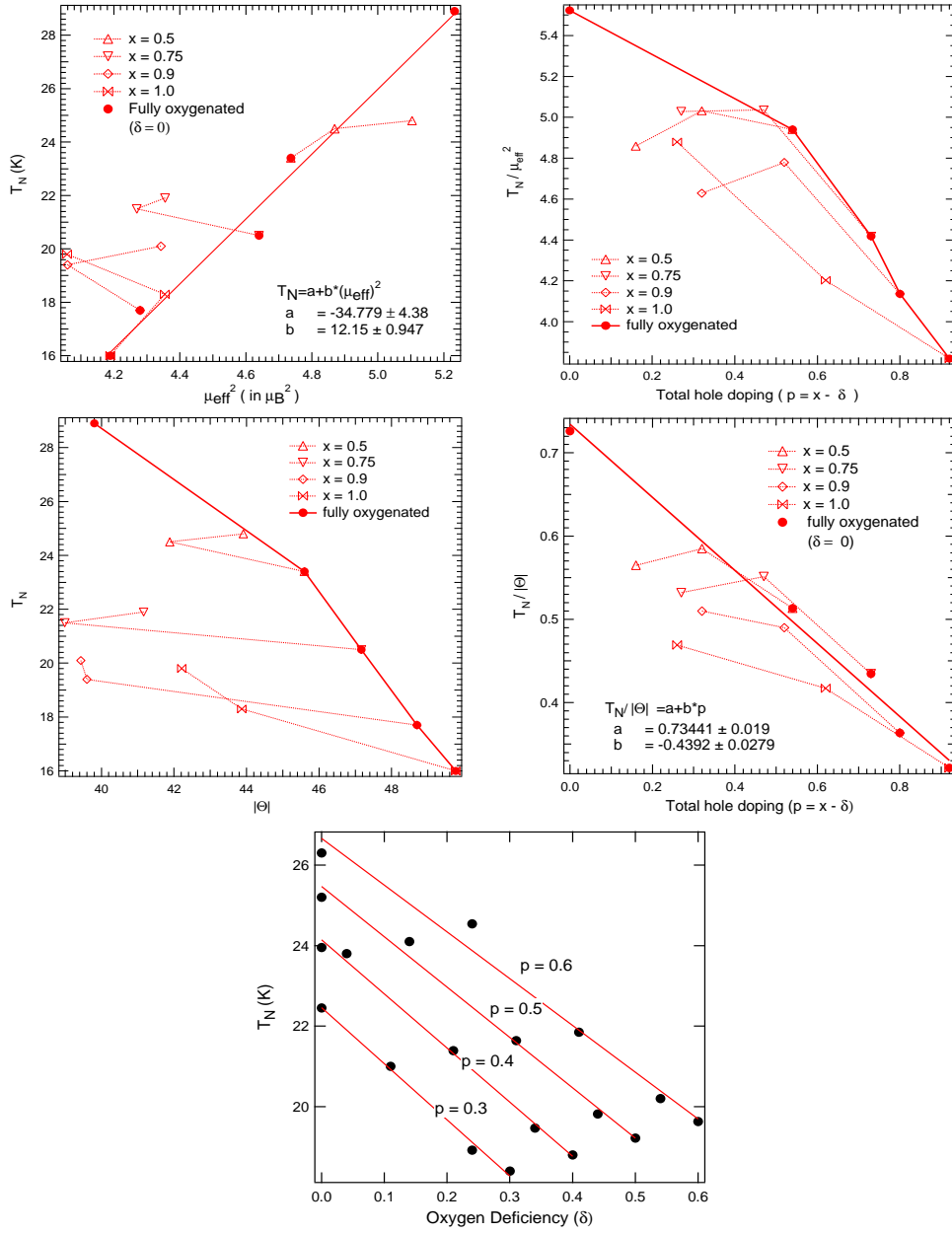


Figure 5.11: Néel temperature, Curie-Weiss temperature, and effective magnetic moments of CaYCuO . The last figure shows the oxygen deficiency dependence of Néel temperature for each hole doping.

increasing p and $|\Theta|$, respectively. Also, from the last graph T_N was found to decrease linearly with oxygen deficiency regardless of the hole doing.

Based on Eqn. 5.5, the main difference between Ca-doping and oxygen deficiency is from the number of the nearest neighbors for the same total hole doping. If the hole doping is fixed, the effective magnetic moment should be the same for both Ca-doping and oxygen deficiency. The exchange coupling constant is given

$$J \sim b^2/U \sim l^{-7}/U^2 \quad (5.6)$$

where b is the exchange integral, U is the coulomb energy, and l is the distance between Cu^{2+} and O^{2-} . Because the change in l is less than 2% from the oxygen deficiency from Fig. 5.3, the exchange coupling constant J can be assumed not to change very much with both Ca-doping and oxygen deficiency. However, the number of the nearest neighbors is directly connected with the oxygen deficiency (δ) because the oxygen ions are mediated by two copper ions. We can set $z \sim (N - \delta)$ where N is an unknown constant and it is confirmed from the last graph of Fig. 5.11. Therefore, the oxygen deficiency decreases the Néel temperature more than Ca-hole doping by reducing the number of nearest neighbors as well as decreasing the average effective magnetic moment.

Oxygen is commonly thought to affect magnetic ordering in cuprate samples by hole doping through the relation $p = x - 2\delta$ and this relation is perfectly matched for $\text{La}_{2-x}\text{Sr}_x\text{CuO}_{4-\delta}$ (LaSrCuO)[77] where δ has negative numbers because this material normally has excess oxygen. If this relation

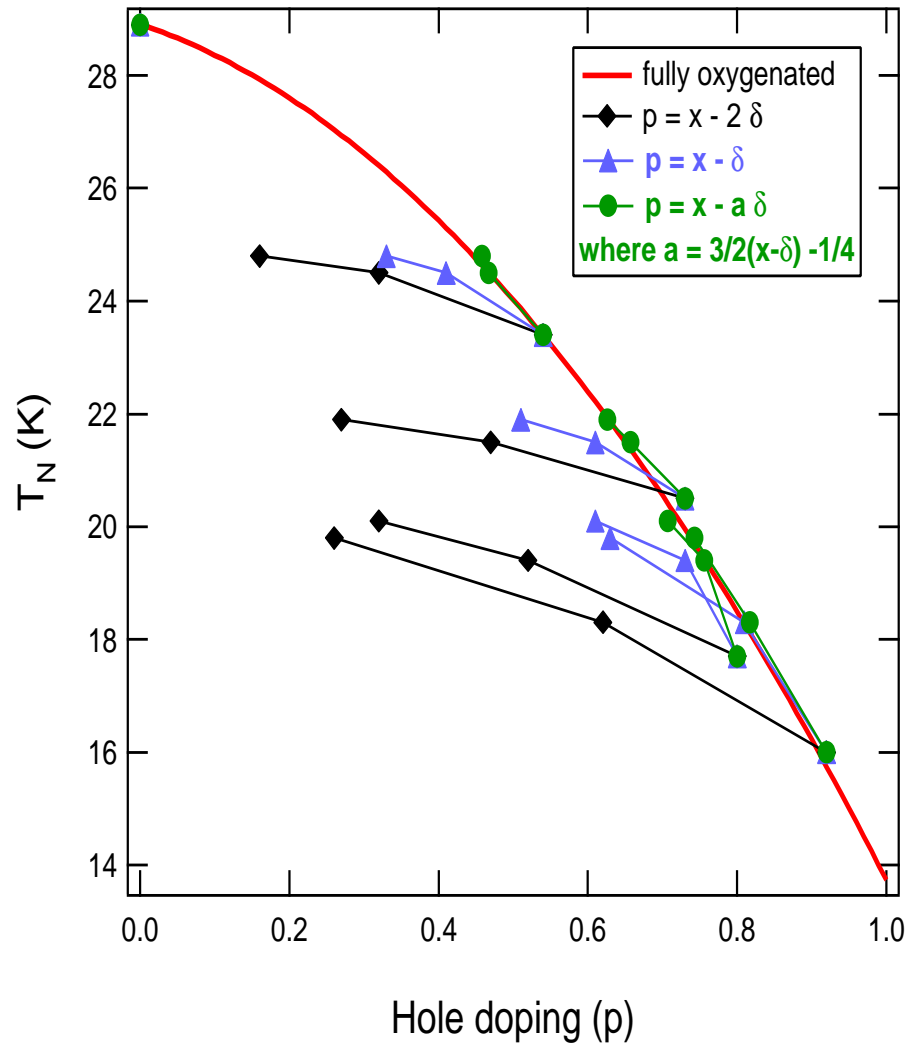


Figure 5.12: Phase diagram with different hole doping relations

could be applied for CaYCuO too, oxygen deficient sample's Néel temperature should be the same as that of fully oxygenated sample for a given hole number. However, this is not the case as seen in Fig. 5.12. The main difference between LaSrCuO and CaYCuO is where the excess/deficient oxygen is located. CaYCuO has oxygen site only on the CuO₄ square but LaSrCuO has several candidate sites. The oxygen on the square is most stable and believed to be hardest one to be removed. CaYCuO become oxygen deficient only when oxygen ion bonding is weak enough due to holes from cation doping. To understand this behavior, we need another equation describing the relation among hole, Ca doping, and oxygen deficiency. Fig. 5.12 shows phase diagram with different equations for effective hole doping (p_{eff}). $p_{eff} = x - a\delta$ where $a = 2/3(x - \delta) - 1/4$ shows a perfect matching of Néel temperatures of oxygen deficient samples to those of fully oxygenated sample. However due to its nonlinear property, it has a difficulty in explaining its meaning. After careful fitting procedures, we found simpler equation for this relation which is shown in Fig. 5.13. $p_{eff} = x - (2/3)\delta = x - 2\delta + (4/3)\delta$. Therefore, We found oxygen content decreases Néel temperature three times less than cation doping or we may say oxygen deficiency on the spin chain induces holes $(4/3)\delta$ more than cation effectively.

To explain the differences in cation doping and changing oxygen content, we need to make a model. Here is the ingredients for the effective hole doping for the two cases. For cation doping (x), doped holes are located at O²⁻ site to make Zhang-rice singlet, which reduces the average effective magnetic

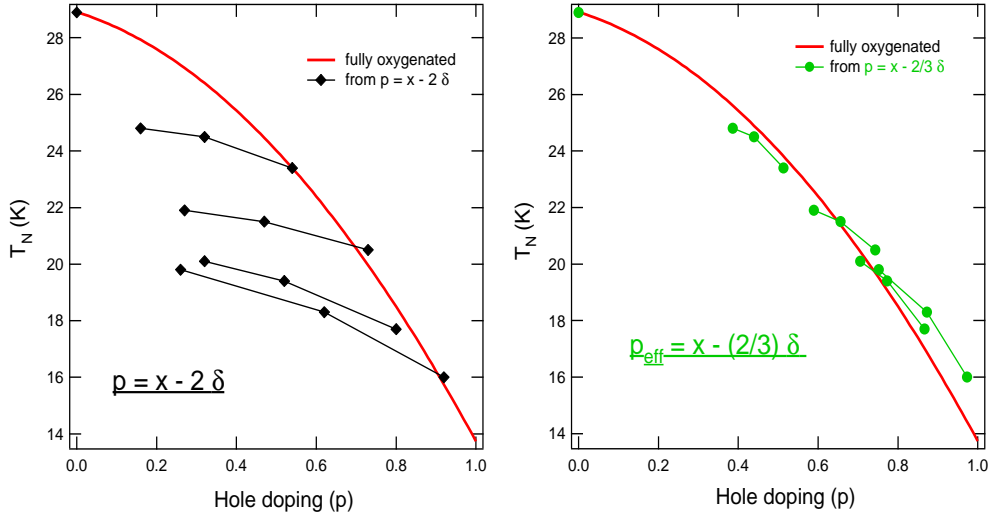


Figure 5.13: Phase diagram with different relations for hole doping, cation doping and oxygen deficiency

moment. The lattice parameters do not change in CuO_4 squares which makes no change in exchange coupling constant J . Oxygen deficiency makes electron doping effectively. For CaYCuO , oxygen deficiency on the chain is induced only after holes are doped from cation, and increases with increasing doped holes. The superexchange coupling (J) between copper ions is made by oxygen ion, therefore removing the oxygen ion cuts the coupling itself to reduce the number of nearest neighbor (z). Also the parameter a along the chain direction increases with oxygen deficiency to make Cu-O-Cu angle wider, which results in the decrease in the exchange coupling constant (J). The change in the number of the nearest neighbor and in the exchange coupling constant makes the difference between cation ion doping and oxygen deficiency in the chain.

Chapter 6

Summary and Future work

Oxygen deficiency effects on the magnetic interaction in the spin chain system $\text{Ca}_{2+x}\text{Y}_{2-x}\text{Cu}_5\text{O}_{10-\delta}$ (CaYCuO) were studied. Samples were made using the conventional solid state reaction method. Annealing under different oxygen pressure was utilized to produce samples with various oxygen deficiencies. X-ray diffraction and iodometric titration were used to characterize the samples. As expected, oxygen deficiency was reduced with increasing environmental oxygen pressure. For increasing Ca-ion doping (x), the oxygen deficiency increased even though the fabrication conditions were the same, and a single phase could not be produced in air when $x \geq 1.25$. On the contrary, the parent compound ($x = 0$) could be made single phased only in air.

Magnetic susceptibility and specific heat were measured to determine the magnetic properties. A λ -shaped peak at 29 K in the specific heat measurement was observed in the parent compound, and the peak was shifted to lower temperatures with increasing Ca-doping as well as decreasing oxygen deficiency. Finally, the peak was totally suppressed for fully oxygenated $x=1.00$ samples and even for somewhat oxygen deficient sample with $x = 1.25$. This change in the peak shows a magnetic transition from 3D long range an-

tiferromagnetic ordering to a short-range ordering. The noticeable difference between Ca-doping and reduced oxygen deficiency was observed in the Néel temperature data. Oxygen deficiency (δ) was previously considered as another method to dope holes (p) in the CuO_2 chain like Ca-doping (x); thus the popular equation $p = x - 2\delta$. But, at the same hole doping level (same p), oxygen deficiency decreases the Néel temperature more than Ca-doping. The reason, suggested by mean field theory, is that oxygen deficiency reduces the number of the nearest neighbors as well as the average effective magnetic moment. A new relation for the effective hole doping was proposed to explain both contributions from Ca-doping and from oxygen deficiency: $p = x - a\delta$ where $a = 2/3(x - \delta) - 1/4$, or the simple version $p = x - (2/3)\delta$.

Fe magnetism was studied in single crystal LiFePO_4 (LFPO) and in Fe_2O_3 nanoparticles (NPs). Anisotropies in an LFPO single crystal sample, fabricated by a flux method, were found in the Lande g-factor, the Curie-Weiss temperature, and the effective magnetic moment, and were explained by a mean field theory. Effects of Au/Silica double coating on the properties of Fe_2O_3 magnetic NPs were studied. Increase in the blocking temperature and the irreversible temperature was observed for the coated NPs

Oxygen deficiency/excess on the cuprate was studied and compared with Ca-doping. Ca-doping makes two change in the compound: lattice parameter and hole doping. For an accurate understanding, we need to separate the two effects on cuprates. $\text{Ca}_2\text{M}_2\text{Cu}_5\text{O}_{10}$ where $\text{M} = \text{Y}, \text{Nd}, \text{Gd}, \text{La}, \text{Lu}$ [21, 22] is one option to study the oxygen deficiency effects on cuprates as a

function of lattice parameter. It is an interesting topic to study the oxygen effects on the fabrication and physical properties of these compounds.

The parent compound of CaYCuO shows a double peak feature from a thermal conductivity measurement [14]. The higher temperature peak is thought to be a possible candidate of magnon heat transport, which is the first observed in Cu-O-Cu edge shared compounds. However, there is a disagreement between single crystal and polycrystal data. We are building thermal conductivity probe with a 2D rotation stage to study this feature in magnetic fields.

Another interesting research topic is the hysteresis of Au/SiO₂ coated γ -Fe₂O₃. This hysteresis appeared up to 300 K contrary to the pure γ -Fe₂O₃ whose hysteresis disappeared above 100 K. Its source is not clear, but may be due to the surface effects of the coating. The surface effects of Au/SiO₂ coating of magnetic nanoparticles is worthwhile for future study.

Appendices

Appendix A

High Pressure Oxygen Furnace

The high pressure oxygen furnace model HPS-3210 by Morris Research Inc. was used to make fully oxygenated samples. Because the safety and operational details can be found in the manual provided by the company, I want to inform you of what is important to start to use the furnace.

The most important part in the furnace is the oxygen pressure vessel. The Morris Research Inc. provides three types of vessel depending on their inner and outer diameters, which are 1) 15 mm (ID) \times 32 mm (OD), 2) 10 mm (ID) \times 32 mm (OD) and 3) 15 mm (ID) \times 50 mm (OD). Vessel 1) is installed now even though all parameters for the manual is for the vessel 2). However I found Don Morris does not recommend using over 100 bar at 1000°C while 200 bar is OK at 970°C degree or below for the vessel 2), which is a much lower pressure (460 bar at 1000°C) than stated in the manual. A reduction of 50°C at a given pressure increases the vessel life about 10x. For vessel 1), the pressure rating at a given temperature is reduced by 35% from the above value. Morris recommends less than 30 bar at 1000°C for vessel 2) but even this pressure seriously reduces the life-time of the vessel (down to $\sim 10^3$ hours) according to him. Vessel 1) and 2) are interchanged within about 10

minutes by changing 2 bolts, removing and replacing the thermocouple, and reconnecting the pressure tubing connection.

Samples, which should be not combustible (no metals except noble metals: Au, Ag and Pt etc. See the manual), are mounted on a combustion boat by a special tool provided by the company. The combustion boats are made by Al_2O_3 which is also available at the company. For vessel 2), Alfa Aesar's Al-23 boat was used (stock number : 33171). This boat interacts with CaYCuO samples at high temperatures, so Au foil (0.05 mm (0.002 in)) is recommended to prevent their contact. Samples should be placed within 40 mm from the far end of the bore in the pressure vessel where the temperature is uniform during the procedure.

After inserting the samples, oxygen gas fills the bore up to the designed pressure after a couple of purging procedures. Note that the pressure can increase more than twice as fast as the temperature. The pressure rise with heating chart can be found in the manual, and keep in mind the chart is for the vessel 2) not for the installed vessel 1) whose pressure should be 75 % of the chart. Temperature control can be done with the Eurotherm 818P temperature controller and with temperature profiles whose example for the heating procedure was shown in the chapter of experiment. Care should be taken to avoid overshoot which could melt the gold(1064°C). At the condition where gas pressure is greater than about 10 bar and the furnace temperature is above about 500°C, the housing lock is blocked and cannot be released which is indicated by the UNLOCK ENABLED light on. The sample should be

removed after the pressure shows one bar and the temperature shows room temperature.

Appendix B

Iodometric Titration[69]

The following solutions should be ready for use before beginning. You will also need about 50 mg of the sample in powder form. It is wise to repeat the entire process at least twice per sample.

- 1a. 2.0 M KI
- 1b. 2.0M HCl
2. 1.0 M HCl
3. 0.7 M KI
4. Starch indicator solution
5. 0.01 N $\text{Na}_2\text{S}_2\text{O}_3 \cdot 5\text{H}_2\text{O}$

The starch indicator solution (#4) can spoil and should be prepared fresh when needed. The HCl/KI solution (#1a / #1b) must be prepared in separate components; if mixed before actual use, the solution evolves free iodine and can no longer be trusted. The other solutions appear to be stable for extended periods, although if either of the iodine solutions begin to yellow (indicating free iodine), discard it and make a fresh solution. Be sure to use the same batch of sodium thiosulfate solution (#5) for both titrations, since the

comparison requires that the concentration of this solution does not change.

B.1 Preparation of the solutions

Note : Only solution # 5 needs to be prepared with great accuracy. Make solution # 5 first because heating and cooling the water is very time consuming and you can make the other solutions while you wait

1a. 2.0 M KI

1. Weigh out 32.2 g KI. Pour it into a 100 ml volumetric flask. Add some distilled H₂O and swirl to dissolve.
2. Top off gradually to 100 ml line, swirling throughout.

1b. 2.0M HCl

1. Put about 250 ml of distilled H₂O into a 1000 ml volumetric flask
2. Pour 165 ml of full-strength HCl (12.1 N) into the same flask. Swirl
3. Top off gradually to 1000 ml with distilled H₂O, swirling throughout

2. 1.0 M HCl

1. Put about 25 ml of distilled H₂O into a 100 ml volumetric flask
2. Pipette 8.3 ml of full-strength HCl into the same flask. Swirl.
3. Top off gradually to 100 ml with distilled H₂O, swirling throughout

4. Alternately, one can dilute 50 ml 2.0 M HCl above with 50 ml distilled H₂O

3. 0.7 M KI

1. Weigh out about 11.6g of KI. Pour it into a 100 ml volumetric flask.
2. Add distilled H₂O gradually, swirling to mix. Top off to 100 ml

4. Starch indicator solution

1. Weigh or estimate ~ 1 g of soluble starch. Add a few drops of distilled H₂O and rub mixture into a paste.
2. Prepare 100 ml of boiling distilled H₂O; add starch paste and stir well.
3. Boil this suspension for about 1 minute, then let it cool.
4. Allow it to settle, then decant the fine suspension into a covered flask or vial; one can filter if somewhat if desired. One may want to keep refrigerated.

5. 0.01 N Na₂S₂O₃·5H₂O

1. Boil a liter of distilled H₂O briefly to get rid of the excess CO₂; let it cool.
2. Weigh exactly 2.4818 g 0.01 N Na₂S₂O₃·5H₂O; place it in a 1000 ml volumetric flask.

3. Add distilled H₂O gradually to dissolve sodium thiosulfate, swirling throughout. Top off to exactly 1000 ml. Be sure that the distilled water has cooled to room temperature in order to get the exact concentration.
4. Write the exact concentration of the solution on the flask together with the date it was prepared. Solutions keep their strength a few months when kept well sealed. Concentration should be verified by titration of standard (e. g., CuO) if desired.

B.2 Experimental Procedures

First: Check that all clean glassware is ready. Clean all glassware after use. Check that the argon tank is ready; establish slow argon flow.

1. **Sample** : Powder > 50 mg of the sample; about 25 mg is required for each of the two parts of the measurement.
2. **Experiment 1.**
 - (a) Check the argon flow from the needle; it may be clogged.
 - (b) Carefully weigh 20-25 mg of the sample (± 0.1 mg) into the special beakers provided for titrations. Record mass (W_1)
 - (c) Add stirring magnet and seal tube with the special red rubber seal. Allow a gentle argon flow for 2 min to remove oxygen. Keep a gentle argon flow throughout the experiment.

- (d) Cover the magnet with the 2.0 M KI (#1a) and add a similar amount of 2.0 M HCl (#1b) with the syringes through the seal (about 4 ml each). Do not add the solutions in reversed order! The yellow color is the free iodine (in form of I_3^-) from the reaction. Some light-colored precipitate may form. Stir the solution throughout the rest of the experiment.
- (e) Add ~ 1 ml of starch indicator solution (#4). Expect a dark blue color or perhaps a little greenish, too.
- (f) Titrate with $Na_2S_2O_3$ solution (#5), dropwise, until the blue color discharges; be sure to record initial and final titrant volumes. Stir vigorously. When approaching the endpoint, the greenish tint will disappear, leaving only dark blue. When the blue color discharges, a slight pinkish color may remain; if titration is continued, the solution will be white, almost clear. Choose the endpoint consistently; since a ratio will be taken, differences in endpoint choice will roughly cancel. Record the volume of titrant used (V_1). Patience pays when you approach the endpoint!

3. Experiment 2.

- (a) Again carefully weigh 20 - 25 mg of the sample (± 0.1 mg) and put it in a beaker and record the mass (W_2).
- (b) Add ~ 7 ml of 1.0 M HCl(#2) and swirl gently to dissolve the sample.

- (c) Boil gently for 10 min in air while bubbling air or oxygen through the solution.
- (d) Add the magnet. Cool and hook up the gentle argon flow for the rest of Experiment 2. Let the argon flow for 2 min.
- (e) Under argon, add 5 ml of 0.7 M KI(**#3**) and gently stir.
- (f) Add ~ 1 ml starch indicator solution (**#4**). Titrate as in Experiment 1. Record the volume of the titrant used (V_2).

B.2.1 Calculations, etc.

Calculate the average [Cu-O] valence in excess of +1 according to:

$$\Delta x = [(V_1/W_1)/(V_2/W_2)] \quad (\text{B.1})$$

Then calculate the oxygen content by using charge balance;

E.g., for $\text{Ca}_2\text{Y}_2(\text{Cu}_5^{1+\Delta x} \text{O}_y)$, we have,

$$2(+3) + 2(+2) + 5(1 + \Delta x) + y(-2) = 0 \implies y = (1/2)[5(1 + \Delta x) + 10] \quad (\text{B.2})$$

This technique can be used for the 1-2-3, 2-1-4 and Bi compounds; it cannot be used for the Tl compounds. Note that this technique measures $p+1=1 + \Delta x$, and thus measures deviations of the average copper valence from +1. This feature can improve accuracy over thermogravimetric techniques when some secondary phases are present (e.g., other oxides, see examples below).

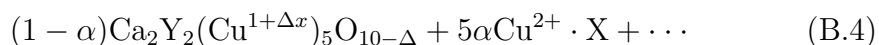
If you have used a thiosulfate solution of known concentration, you may calculate the molecular weight of your sample from experiment 2.

$$M \cdot W(\text{per Cu}) = w_2/(C_t \cdot V_2) \quad (\text{B.3})$$

For 123 and hole doped 214 compounds, the molecular weight should be within $\sim 1\%$ of the theoretical value if your sample has the stoichiometry you think it has. Electron doped 214's may cause problems due to a very low solubility. Boil the solution, kept safely under an Ar flow, under experiment 1 to avoid this problem. Finally, the determination of the oxygen content by titration relies on the following assumptions.

1. That you know the valences of the ions in question, once they get into solution. Note that you do not know anything about the valences in the solid. Special ions are PR, which is always 3+ in acidic solution, and Ce which is only slowly reduced to the 3+ state under the conditions of the experiment. Boiling under argon may speed up the process.
2. You may check that the sample has the stoichiometry that you think it has as mentioned above, but in the calculation of the oxygen content you assume that it is single phase. As a rule of thumb, the calculated oxygen content will always be too low if you have correct stoichiometry, but two phases. If you do not have correct stoichiometry, you have to go through the chemical reactions to find out how too much or too little copper affects the experiments.

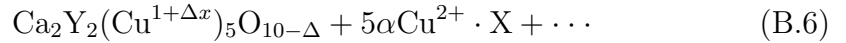
Real samples may contain impurity phases from imperfect synthesis or excessive Cu oxides. When we consider a sample is not single phase but the has correct stoichiometry, E.g.,



We always measure the average copper valence in excess of +1, Δx regardless of the composition of the sample. For this case, the average copper valence in excess of +1 equals,

$$\Delta x = \frac{\Delta x_{exp} - \alpha}{1 - \alpha} \quad (\text{B.5})$$

which is from $5(1 + x_{exp}) = 5(1 - \alpha)(1 + \Delta x) + 10\alpha$ where Δx_{exp} is the number of Cu ions measured. Therefore the inferred, incorrect value of δ is $\delta_{incorr} = \frac{5 - 5\Delta x_{exp}}{2}$ and the real, correct value of δ is $\delta_{corr} = \frac{5 - 5\Delta x}{2} = \frac{5 - 5 \cdot \Delta x_{exp}}{2(1 - \alpha)}$. If we use $x_{exp} = 0.9$ and $\alpha = 0.1$ (10 wt% impurities), then while $\delta_{incorr} = 0.25$, $\delta_{corr} = 0.278$ which is around 10% difference. Now let's think about the non-stoichiometric multi-phase case (excessive Cu oxides), which gives a wrong molecular weight in the second titrations. E.g.,



In this case, we should use this equation for copper, $5(1 + \alpha)(1 + \Delta x_{exp}) = 5(1 + \Delta x) + 10\alpha$, and $\Delta x = \Delta x_{exp}(1 + \alpha) - \alpha$. Then we get the incorrect and correct values for δ 's such as $\delta_{uncorr} = \frac{5 - 5\Delta x_{exp}}{2}$ and $\delta_{corr} = \frac{5 - 5\Delta x}{2} = \frac{5(1 + \alpha)(1 - \Delta x_{exp})}{2}$. If we use $x_{exp} = 0.9$ and $\alpha = 0.1$ (10 wt% impurities) again, then $\delta_{incorr} = 0.25$, $\delta_{corr} = 0.275$ which is about 9.5% difference.

Appendix C

Derivation of the Magnetic Susceptibilities in anisotropic systems

C.1 Magnetic field applied parallel to the z-axis

Let's start with the Hamiltonian given in the Chap. 4.

$$H_i = -(z_1 J_1 + z_2 J_2 + z_\perp J_\perp) \bar{S} S_{iz} + D S_{iz}^2 - g_{//} \mu_B S_{iz} H - \mu_B^2 \Lambda_{//} H^2. \quad (\text{C.1})$$

The eigenvalue of this Hamiltonian is

$$E_i = -(z_1 J_1 + z_2 J_2 + z_\perp J_\perp) \bar{S} m + D m^2 - g_{//} \mu_B m H - \mu_B^2 \Lambda_{//} H^2 \quad (\text{C.2})$$

where the azimuthal magnetic number m 's are 0, ± 1 and ± 2 . We may use the general equation to get magnetization (M) and magnetic susceptibility (χ) as follows:

$$M = \frac{\sum (-\frac{\partial E_m}{\partial H}) \cdot \exp(-\frac{E_m}{k_B T})}{\sum \exp(-\frac{E_m}{k_B T})} \quad (\text{C.3})$$

$$\chi = \frac{\partial M}{\partial H} = N_A k_B T \left(\frac{\partial^2 \ln Z}{\partial H^2} \right) \quad (\text{C.4})$$

where Z is the partition function given by

$$Z = \sum_m \exp(-\frac{E_m}{k_B T}). \quad (\text{C.5})$$

Now we may think in the paramagnetic state $-(z_1 J_1 + z_2 J_2 + z_\perp J_\perp)\bar{S}$ and $g_{//}\mu_B H$ are so small compared with $k_B T$ that these terms can be treated as a perturbation. Then, the energy can be written as

$$E_m = m^2 D - \mu_B^2 \Lambda_{//} H^2 + \alpha m, \quad (\text{C.6})$$

where $\alpha = -(z_1 J_1 + z_2 J_2 + z_\perp J_\perp)\bar{S} + g_{//}\mu_B H$. From Eqn. C.3,

$$M = 2\mu_B^2 \Lambda_{//} H + \frac{A}{2\exp(-4D/k_B T) + 2\exp(-D/k_B T) + 1} \quad (\text{C.7})$$

where the numerator of the second term A is

$$\begin{aligned} A &= -2 \frac{\partial \alpha}{\partial H} \exp(-4D/k_B T) \exp(2\alpha/k_B T) + 2 \frac{\partial \alpha}{\partial H} \exp(-4D/k_B T) \exp(-2\alpha/k_B T) \\ &\quad - \frac{\partial \alpha}{\partial H} \exp(-D/k_B T) \exp(\alpha/k_B T) + \frac{\partial \alpha}{\partial H} \exp(-D/k_B T) \exp(-\alpha/k_B T) \\ &= -2 \frac{\partial \alpha}{\partial H} \cdot \frac{4\alpha}{k_B T} \exp(-4D/k_B T) - \frac{\partial \alpha}{\partial H} \cdot \frac{2\alpha}{k_B T} \exp(-D/k_B T) \\ &= \frac{2\alpha}{k_B T} \cdot \frac{\partial \alpha}{\partial H} (4\exp(-4D/k_B T) + \exp(-D/k_B T) + 0\exp(0/k_B T)) \\ &= \frac{2\alpha}{k_B T} \cdot \frac{\partial \alpha}{\partial H} \left(\sum_m m^2 \exp(-m^2 D/k_B T) \right) \end{aligned}$$

, where we use $\exp(2\alpha/k_B T) \approx 1 + 2\alpha/k_B T$. Then the magnetization is

$$M = 2\mu_B^2 \Lambda_{//} H + \frac{D \cdot (\alpha \frac{\partial \alpha}{\partial H}) \cdot \sum_m m^2 \exp(-m^2 D/k_B T)}{D \cdot k_B T \sum_m \exp(-m^2 D/k_B T)} \quad (\text{C.8})$$

$$= 2\mu_B^2 \Lambda_{//} H + \frac{\alpha}{D} \cdot \frac{\partial \alpha}{\partial H} \cdot F_{//} \quad (\text{C.9})$$

$$\approx 2\mu_B^2 \Lambda_{//} H + \frac{\alpha}{D} \cdot g_{//}\mu_B \cdot F_{//} \quad (\text{C.10})$$

$$= M_0 + M', \quad (\text{C.11})$$

where we use $\frac{\partial \alpha}{\partial H} \approx g_{//}\mu_B$ and,

$$F = \frac{\sum_m -D m^2 \exp(-D m^2)}{k_B T \sum_m \exp(-D m^2/k_B T)} = \frac{-1}{0.7 + k_B T/2D}. \quad (\text{C.12})$$

Now we can obtain the susceptibility by taking a derivative of M to H , then

$$\chi = \chi_0 + \chi' \quad (\text{C.13})$$

$$= 2\mu_B^2 \Lambda_{//} + \frac{\partial \alpha}{\partial H} \cdot \frac{g_{//} \mu_B}{D} \cdot F_{//} \quad (\text{C.14})$$

where we think more term for the derivative of α to H ,

$$\begin{aligned} \frac{\partial \alpha}{\partial H} &= g_{//} \mu_B - (z_1 J_1 + z_2 J_2 + z_{\perp} J_{\perp}) \frac{\partial \bar{S}}{\partial H} \\ &= g_{//} \mu_B - (z_1 J_1 + z_2 J_2 + z_{\perp} J_{\perp}) \frac{\chi'}{g_{//} \mu_B}. \end{aligned}$$

Then we can find χ' from

$$\begin{aligned} \chi' &= \frac{\partial \alpha}{\partial H} \cdot \frac{g_{//} \mu_B}{D} \cdot F_{//} \\ &= (g_{//} \mu_B - (z_1 J_1 + z_2 J_2 + z_{\perp} J_{\perp}) \frac{\chi'}{g_{//} \mu_B}) \cdot \frac{g_{//} \mu_B}{D} \cdot F_{//}. \end{aligned}$$

Therefore the magnetic susceptibility is

$$\chi = 2N\mu_B^2 \Lambda_{//} - \frac{N_A g_{//}^2 \mu_B^2 F_{//}}{D + (z_1 J_1 + z_2 J_2 + z_{\perp} J_{\perp}) F_{//}} \quad (\text{C.15})$$

$$= 2N\mu_B^2 \Lambda_{//} + \frac{2N_A g_{//}^2 \mu_B^2}{k_B T + 1.4D - 2(z_1 J_1 + z_2 J_2 + z_{\perp} J_{\perp})}, \quad (\text{C.16})$$

which was used in fitting the experimental data in Chap. 4.

C.2 Magnetic field applied perpendicular to the z-axis

We may also start with the Hamiltonian with a field applied along x-axis, as given in the Chap. 4,

$$H_i = -(z_1 J_1 + z_2 J_2 + z_{\perp} J_{\perp}) \bar{S}_x S_{ix} + D S_{iz}^2 - g_{\perp} \mu_B S_{ix} H_x - \mu_B^2 \Lambda_{\perp} H_x^2. \quad (\text{C.17})$$

And this Hamiltonian can be written again as

$$H_i = H_0 + H_1 \quad (\text{C.18})$$

$$= DS_{iz}^2 - \mu_B^2 \Lambda_\perp H_x^2 - \alpha S_{ix}, \quad (\text{C.19})$$

where

$$\alpha = -(z_1 J_1 + z_2 J_2 + z_\perp J_\perp) \bar{S}_x S_{ix} - g_\perp \mu_B S_{ix} H_x. \quad (\text{C.20})$$

Since the applied external field is small, the effect on the x-component of the spin (H_1) can be treated as a second-order perturbation term. Then unperturbed energy (zeroth order) is given as

$$\langle 2, 0 | H_0 | 2, 0 \rangle = -\mu_B^2 \Lambda_\perp H_x^2 \quad (\text{C.21})$$

$$\langle 2, \pm 1 | H_0 | 2, \pm 1 \rangle = D - \mu_B^2 \Lambda_\perp H_x^2 \quad (\text{C.22})$$

$$\langle 2, \pm 2 | H_0 | 2, \pm 2 \rangle = 4D - \mu_B^2 \Lambda_\perp H_x^2. \quad (\text{C.23})$$

The 1st perturbed energy is zero for all states since $\langle 2, m | H_1 | 2, m \pm 1 \rangle = 0$ considering

$$S_x = \frac{1}{2}(S_+ + S_-) \quad (\text{C.24})$$

$$S_\pm = S_x \pm iS_y \quad (\text{C.25})$$

$$S_\pm |S, m\rangle = \sqrt{S(S+1) - m(m \pm 1)} |S, m \pm 1\rangle, \quad (\text{C.26})$$

where we set $\hbar = 1$ for the convenience. However the 2nd perturbed energy is not zero but given as, for example $m = 0$,

$$\sum_{m \neq 0} \frac{\langle m | H_1 | 0 \rangle^2}{E_0^0 - E_m^0} = \frac{\langle 1 | \alpha S_x | 0 \rangle^2}{E_0^0 - E_1^0} + \frac{\langle -1 | \alpha S_x | 0 \rangle^2}{E_0^0 - E_{-1}^0} \quad (\text{C.27})$$

$$= \frac{6\alpha^2}{-4D} + \frac{6\alpha^2}{-4D} = -\frac{3\alpha^2}{D}. \quad (\text{C.28})$$

In the same way, we can get the energies as follows:

$$E_0 = -\mu_B^2 \Lambda_{\perp} H_x^2 - \frac{3\alpha^2}{D} \quad (\text{C.29})$$

$$E_{\pm 1} = D - \mu_B^2 \Lambda_{\perp} H_x^2 + \frac{7\alpha^2}{6D} \quad (\text{C.30})$$

$$E_{\pm 2} = 4D - \mu_B^2 \Lambda_{\perp} H_x^2 + \frac{\alpha^2}{3D}. \quad (\text{C.31})$$

Now we can find the magnetization in the same way as in the parallel case given in the previous section,

$$M_{\perp} = 2\mu_B^2 \Lambda_{\perp} H + \frac{\alpha}{D} \cdot g_{\perp} \mu_B \cdot F_{\perp} \quad (\text{C.32})$$

$$= M_{\perp,0} + M'_{\perp}, \quad (\text{C.33})$$

where

$$F_{\perp} = \frac{\frac{4}{3} \exp(-4D/k_B T) + \frac{14}{3} \exp(-D/k_B T) - 6}{2 \exp(-4D/k_B T) + 2 \exp(-D/k_B T) + 1} = \frac{1}{0.35 - k_B T / 2D}. \quad (\text{C.34})$$

In the same way as the previous section we can also find the magnetic susceptibilities as

$$\chi_{\perp} = \chi_{\perp,0} + \chi'_{\perp} \quad (\text{C.35})$$

$$= 2N\mu_B^2 \Lambda_{\perp} + \frac{N_A g_{\perp}^2 \mu_B^2 F_{\perp}}{-D + (z_1 J_1 + z_2 J_2 + z_{\perp} J_{\perp}) F_{\perp}} \quad (\text{C.36})$$

$$= 2N\mu_B^2 \Lambda_{\perp} + \frac{2N_A g_{\perp}^2 \mu_B^2}{k_B T - 0.7D - 2(z_1 J_1 + z_2 J_2 + z_{\perp} J_{\perp})}. \quad (\text{C.37})$$

The perpendicular axes have the same expression for the susceptibility so the anisotropy comes from the differences in each parameter $\Lambda_{\perp,a}$ and $\Lambda_{\perp,c}$, and $g_{\perp,a}$ and $g_{\perp,c}$. These equations were also used in analyzing the experimental data.

Bibliography

- [1] H. R. Ott A. Freimuth A. V. Sologubenko, T. Lorenz. *Journal of Low Temperature Physics* **147**, page 387, 2007.
- [2] T. Ami, M. K. Crawford, R. L. Harlow, Z. R. Wang, D. C. Johnston, Q. Huang, and R. W. Erwin. *Phys. Rev. B* **51**, page 5994, 1995.
- [3] Y. Ando, J. Takeya, D. L. Sisson, S. G. Doettinger, I. Tanaka, R. S. Feigelson, and A. Kapitulnik. *Phys. Rev. B.* **58**, page R2913, 1998.
- [4] E. A. Appelman, L. R. Morss, A. M. Kini, U. Geiser, A. Umezawa, G. W. Crabtree, and K. D. Carlson. *Inorganic Chemistry* **26**, page 3237, 1987.
- [5] S. Banerjee, S. Roy, J. W. Chen, and D. Chakravorty. *J. Magn. Magn. Mater.* **219**, page 45, 2000.
- [6] T.H.K. Barron and G.K White. *Heat Capacity and Thermal Expansion at Low Temperatures*. Kluwer AcademicPlenum Publishers, 1999.
- [7] R. Berman. Clarendon Press Oxford, 1976.
- [8] J. W. Bulte and D. L. Kraitchman. *NMR Biomed.* **17**, page 484, 2004.
- [9] J. Carcia-Otero, M. Porto, J. Rivas, and A. Bunde. *Phys. Rev. Lett.* **84**, page 167, 2000.

- [10] Richard L. Carlin. Springer-Verlag, 1986.
- [11] M. D. Chabot and J. T. Markert. *Phys. Rev. Lett.* **86**, page 163, 2001.
- [12] Michelle Diane Chabot. Design and construction of a semi-adiabatic calorimetry apparatus with applications to the $\text{Ca}_{2+x}\text{Y}_{2-x}\text{Cu}_5\text{O}_{10}$ system. Master's thesis, University of Texas at Austin, 1998.
- [13] J.-H. Choi, G. I. Drandova, T. C. Messina, K. Park, and J. T. Markert. *AiP Conf. Proc.* **850**, page 1019.
- [14] J.-H. Choi, T. C. Messina, J. Yan, G. I. Drandova, and J. T. Markert. *Journal of Magnetism and Magnetic Materials* **272-276**, page 970.
- [15] S. Y. Chung, J. Bloking, and Y. M. Chiang. *Nat. Mater.* **1**, page 123, 2002.
- [16] T. W. Clinton, J. W. Lynn, J. Z. Liu, Y. X. Jia, T. J. Goodwin, R. N. Shelton, B. W. Lee, M. Buchgeister, M. B. Maple, and J. L. Peng. *Phys. Rev. B* **51**, page 15429, 1995.
- [17] F. Albert Cotton. Wiley-Interscience Publication, 1990.
- [18] J. G. Creer and G. J. Troup. *Physics Letter* **32A**, page 439, 1970.
- [19] M.F. Crommie, Amy Y. Liu, Marvin L. Cohen, and A. Zettl. *Phys. Rev. B* **41**, page 2526, 1990.
- [20] P. Datta, A. Manivannan, M. S. Seehra, N. Shah, and S. Seehra. *Phys. Rev. B* **70**, page 174428, 2004.

- [21] P. K. Davies. *J. Solid State Chem.* **95**, page 365, 1991.
- [22] P. K. Davies, E. Caignol, and T. King. *J. Am. Ceram. Soc.* **74**, page 569, 1991.
- [23] L. J. de Jongh. Kluwer Academic Publisher, 1990.
- [24] L. J. de Jongh and A. R. Miedema. *Adv. Phys.* **23**, page 1, 1974.
- [25] E. Du Tremolet de Lacheisserie, D. Gignoux, and M. Schlenker. Springer, 2005.
- [26] J. Dormann, D. Fiorani, and M. El Yamani. *Phys. Lett. A* **120**, page 95, 1987.
- [27] M. El-Hilo, K. O'Grady, and R. W. Chantrell. *J. Magn. Magn. Mater.* **114**, page 307, 1992.
- [28] F. Beech, S. Miraglia, A. Santoro, and R. S. Roth. *Phys. Rev. B* **35**, page 8778, 1987.
- [29] H. F. Fong, B. Keimer, J. W. Lynn, A. Hayashi, and R. J. Cava. *Phys. Rev. B* **59**, page 6873, 1999.
- [30] K. Fujita, T. Noda, K. M. Kojima, H. Eisaki, and S. Uchida. *Phys. Rev. Lett.* **95**, page 097006, 2005.
- [31] Xu Gaojie, Pu Qirong, Zhang Zengming, , and Ding Zejun. *J. Supercon.* **14**, page 509, 2001.

- [32] J. Gauthier, S. Gagne, J. Renaud, M.-E. Gosselin, P. Fournier, and P. Richard. *Phys. Rev. B* **75**, page 024424, 2007.
- [33] J. B. Goodenough. *Phys. Rev.* **100**, page 564, 1955.
- [34] John B. Goodenough. Robert E. Krieger Publishing Company, 1976.
- [35] J.E. Greedan, A. H. O'Reilly, and C. V. Stager. *Phys. Rev. B* **35**, page 8770, 1987.
- [36] E. Gurewitz, J. Makovsky, and H. Shaked. *Phys. Rev. B* **9**, page 1071, 1974.
- [37] D. C. Harris and T. A. Hewston. *Jpn. J. Appl. Phys.* **26**, page L1228, 1987.
- [38] M. Hase, I. Terasaki, and Kunimitsu Uchinokura. *Phys. Rev. Lett.* **70**, page 3651, 1993.
- [39] A. Hayashi, B. Batlogg, and R. J. Cava. *Phys. Rev. B* **58**, page 2678, 1998.
- [40] C. Hess, C. Baumann, U. Ammerahl, B. Buchner, F. Heidrich-Meisner, W. Brenig, and A. Revcolevschi. *Phys. Rev. B.* **64**, page 184305, 2001.
- [41] J. S. Higgins, Y. Dagan, M. C. Barr, B. D. Weaver, and R. L. Greene. *Phys. Rev. B* **73**, page 104510, 2006.
- [42] Z. Hiroi, M. Okumura, T. Yamada, and M. Takano. *J. Phys. Soc. Jpn* **69**, page 1824, 2000.

- [43] Z. Hiroi, M. Takano, M. Azuma, and Y. Takeda. *Nature* **364**, page 315, 1993.
- [44] Beom hoan O. *Magnetic and transport properties of T'-phase and Gallium cuprates*. PhD thesis, University of Texas at Austin, 1993.
- [45] A. Honma. *J. Phys. Soc. Japan* **15**, page 456, 1960.
- [46] P. Horsch, M. Sofin, M. Mayr, and M. Jansen. *Phys. Rev. Lett.* **94**, page 076403, 2005.
- [47] J. L. Horwood, M. G. Townsend, and A. H. Webster. *J. Solid State Chem.* **17**, page 35, 1976.
- [48] A. W. Hull. *Phys. Rev.* **10**, page 661, 1917.
- [49] M. Isobe, K. Kimoto, and E. Takayama-Muromachi. *J. Phys. Soc. Jpn.* **71**, page 782, 2002.
- [50] J. Jeong, S. Lee, J. Kim, and S. Shin. *Phys. Stat. Sol. (b)* **241**, page 1593, 2004.
- [51] Xiaojun Ji, Ruping Shao, Andrew M. Elliott, R. Jason Stafford, Emilio Esparza-Coss, James A. Bankson, Gan Liang, Zhi-Ping Luo, Keeseong Park, John T. Markert, and Chun Li. *J. Phys. Chem. C* **111**, page 6245, 2007.
- [52] J. Kanamori. *J. Phys. Chem. Solids* **10**, page 87, 1959.

- [53] J.M.Tarascon, L.H.Greene, W.R. McKinnon, and G.W.Hull. *Sol. St. Comm.* **63**, page 499, 1987.
- [54] D. C. Johnston, R. K. Kremer, M. Troyer, X. Wang, A. Klumper, S. L. Budko, A. F. Panchula, and P. C. Canfield. *Phys. Rev. B* **61**, page 9558, 2000.
- [55] Olivier Kahn. VCH Publishers, Inc., 1993.
- [56] H. J. Kang, P. Dai, B. J. Campbell, P. J. Chupas, S. Rosenkranz, P. L. Lee, Q. Huang, S. Li, S. Komiya, and Y. Ando. *Nature* **6**, page 224, 2007.
- [57] K. Kishio, J.-I. Shimoyama, T. Hasegawa, K.Kitazawa, and K. Fuelk. *Jpn. J. Appl. Phys.* **26**, page L1228, 1987.
- [58] F. B. Koch and M. E. Fine. *J. Appl. Phys.* **38**, page 1470, 1967.
- [59] J. M. Kosterlitz and D. J. THouless. *J. Phys. C* **6**, page 1181, 1973.
- [60] C. Kottel. *Introduction to Solid State Physics*. John Wiley and Sons, Inc.
- [61] K. Kudo, S. Kurogi, Y. Koike, T. Nishizaki, and N. Kobayashi. *Phys. Rev. B* **71**, page 104413, 2005.
- [62] K. I. Kumagai, S. Tsuji, M. Kato, and Y. Koike. *Phys. Rev. Lett.* **78**, page 1992, 1997.

- [63] A. M. De Leon-Guevara, P. Berthet, J. Berthon, F. Millot, A. Revcolevschi, A. Anane, C. Dupas, K. Le Dang, J. P. Renard, and P. Veillet. *Phys. Rev. B* **56**, page 6031, 1997.
- [64] J. Li, V. O. Garlea, J. L. Zarestky, and D. Vaknin. *Phys. Rev. B* **73**, page 024410, 2006.
- [65] G. Liang, K. Park, J. Li, R. Benson, D. Vaknin, J. T. Markert, and M. Croft. *submitted to Phys. Rev. B*, 2007.
- [66] M. E. Lines. *Phys. Rev.* **156**, page 543, 1967.
- [67] Q. Q. Liu, H. Yang, X. M. Qin, Y. Yu, L. X. Yang, F. Y. Li, R. C. Yu, C. Q. Jin, and S. Uchida. *Phys. Rev. B* **74**, page 100506(R), 2006.
- [68] H. M. Luo, B. N. Lin, Y. H. Lin, H. C. Chiang, Y. Y. Hsu, T. I. Hsu, T. J. Lee, H. C. Ku, C. H. Lin, H.-C. I. Kao, J. B. Shi, J. C. Ho, C. H. Chang, S. R. Hwang, and W.-H. Li. *Phys. Rev. B* **61**, page 14825, 2000.
- [69] J. T. Markert. *Lab note*, 1988.
- [70] C. Martinez-Boubeta, K. Simeonidis, M. Angelakeris, N. Pazos-Perez, M. Giersig, A. Delimitis, L. Nalbandian, V. Alexandrakis, and D. Niarchos. *Phys. Rev. B* **74**, page 054430, 2006.
- [71] M. Matsuda, K. Kakurai, S. Kurogi, K. Kudo, Y. Koike, H. Yamaguchi, T. Ito, and K. Oka. *Phys. Rev. B* **71**, page 104414, 2005.

- [72] M. Matsuda and K. Katsumata. *J. Magn. Magn. Mater.* **177-181**, page 683, 1998.
- [73] M. Matsuda, H. Yamaguchi, T. Ito, C. H. Lee, K. Oka, Y. Mizuno, T. Tohyama, S. Maekawa, and K. Kakurai. *Phys. Rev. B* **63**, page 180403, 2001.
- [74] Y. Miyazaki, I. Gameson, and P. P. Edwards. *J. Solid State Chem.* **145**, page 511, 1999.
- [75] Y. Mizuno, T. Tohyama, S. Maekawa, T. Osafune, H. Eisaki, and S. Uchida. *Phys. Rev. B* **57**, page 5326, 1998.
- [76] K. Mizushima, P. C. Jones, P. J. Wiseman, and J. B Goodenough. *Mater. Res. Bull.* **15**, page 783, 1980.
- [77] Hashini E. Mohottala, Barrett O. Wells, Joseph I. Budnick, William A. Hines, Christof Niedermayer, Linda Udby, Christian Bernhard, Arnold R. Moodenbaugh, and Fang-Cheng Chou. *Nature Materials* **5**, page 377, 2006.
- [78] M D. Mukadam, S. M. Yusuf, P. Sharma, and S. K. Kulshreshtha. *J. Magn. Magn. Mater.* **271-276**, page 1401, 2004.
- [79] A. I. Nazzal, V. Y. Lee, E. M. Engler, R. D. Jacowitz, Y. Tokura, and J. B. Torrance. *Physica C* **153-155**, page 1367, 1988.

- [80] K. Oka, H. Yamaguchi, and T. Ito. *J. Cryst. Growth* **229**, page 419, 2001.
- [81] S. Okubo, K. Kawakami, M. Yoshida, and H. Ohta. *Physica Status Solidi(c)* **3**, page 2828, 2006.
- [82] A. K. Pahdi, K. S. Najundaswamy, and J. B Goodenough. *J. Electrochem. Soc.* **144**, page 1188, 1997.
- [83] Keeseong Park, Theodore Cackowski, and John T. Markert. *Physica B in press*, 2007.
- [84] Keeseong Park, Yong J. Lee, and John T. Markert. *Physica C* **460-462(1)**, page 466, 2007.
- [85] Keeseong Park, Gan Liang, Xiaojun Ji, Zhi-Ping Luo, Chun Li, Mark C. Croft, and John T. Markert. *J. Phy. Chem. C in press*, 2007.
- [86] Charles P. Poole. *Copper oxide superconductor, Wiley-International Pub. Chap. 7*, 1988.
- [87] P. G. Radaelli, D. G. Hinks, A. W. Mitchell, B. A. Hunter, J. L. Wagner, B. Dabrowski, K. G. Vandervoort, H. K. Viswanathan, and J. D. Jorgensen. *Phys. Rev. B* **49**, page 4163, 1994.
- [88] R. Beyers and G. Lim et al. Mrs anaheim symp. page 149, 1987.
- [89] G. Rosa, H. Guerrero, D. Levy, A. Alvarez-Herrero, and R. P. del Real. *J. Appl. Phys.* **97**, page 64314, 2005.

- [90] R. P. Santaro and R. E. Newman. *Acta Cryst.* **22**, page 344, 1967.
- [91] P. Sengupta, A. W. Sandvik, and R. R. P. Singh. *Phys. Rev. B* **68**, page 094423, 2003.
- [92] S. Shi, L. Liu, C. Ouyang, D. S. Wang, Z. Wang, L. Chen, and X. Huang. *Phys. Rev. B* **68**, page 195108, 2003.
- [93] R. Shiozaki, K. Takenaka, Y. Sawaki, and S. Sugai. *Phys. Rev. B* **63**, page 184419, 2001.
- [94] T. Siegrist, R. S. Roth, C. J. Rawn, and J. J. Ritter. *Chem. Mater.* **2**, page 192, 1990.
- [95] N. G. Soffel, J. M. Tarascon, Y. Chang, M. Onelliion, D. W. Niles, and G. Margaritondo. *Phys. Rev. B* **36**, page 3986, 1987.
- [96] A. V. Sologubenko, E. Felder, K. Gianno, H. R. Ott, A. Vietkine, and A. Revcolevschi. *Phys. Rev. B.* **62**, page R6108, 2000.
- [97] A. V. Sologubenko, K. Gianno, H. R. Ott, U. Ammerahl, and A. Revcolevschi. *Phys. Rev. Lett.* **84**, page 2714, 2000.
- [98] A. V. Sologubenko, K. Gianno, H. R. Ott, A. Vietkine, and A. Revcolevschi. *Phys. Rev. B.* **64**, page 054412, 2001.
- [99] K. Sreedhar and P. Ganguly. *Phys. Rev. B* **41**, page 371, 1990.
- [100] G. R. Steward. *Rev. Sci. Instru.* **54**, page 1, 1983.

- [101] J. Stohr and H. C. Siegmann. Springer, 2006.
- [102] P. F. Sullivan and G. Seidel. *Phys. Rev.* **173**, page 679, 1968.
- [103] Steve Swinnea. *Lab experiments in X-ray diffraction (ChE 386K)*. <http://capsicum.me.utexas.edu/ChE386K>.
- [104] E. Taboada, R. P. del Real, M. Gich, A. Roig, and E. Molins. *J. Magn. Magn Mater.* **301**, page 175, 2006.
- [105] J. L. Tallon, G. V. Williams, C. Bernhard, D. M. Pooke, M. P. Staines, J. D. Johnson, and R. H. Meinhold. *Phys. Rev. B* **53**, page R11972, 1996.
- [106] J. M. Tarascon and M. Armand. *Nature* **414**, page 359, 2001.
- [107] P. Tartaj, O. Bomati-Miguel T. Gonzalez-Carreno-Carreno, and C. J. Serna. *Phys. Rev. B* **69**, page 094401, 2004.
- [108] Y. Tokura, H. Takagi, and S. Uchida. *Nature* **337**, page 345, 1989.
- [109] J. B. Torrance, A. Bezing, A. I. Nazzari, T. C. Huang, S. S. P. Parkin, D. T. Keane, S. J. LaPlaca, P. M. Horn, and G. A. Held. *Phys. Rev. B* **40**, page 8872, 1989.
- [110] M. Uehara, T. Nagata, J. Akimitsu, H. Takahashi, N. Mori, and K. Kinoshita. *J. Phys. Soc. Jpn.* **65**, page 2764, 1996.
- [111] M. Wakeshima, K. Ino, and Y. Hinatsu. *Solid State Commun.* **120**, page 145, 2001.

- [112] R. Weht and W. E. Pickett. *Phys. Rev. Lett.* **81**, page 2502, 1998.
- [113] Guy K. White. Oxford Science Publications, 1997.
- [114] Robert M. White. Springer, 2007.
- [115] G. V. M. Williams and J. L. Tallon. *Physica C* **258**, page 41, 1996.
- [116] Yong-Nian Xu, Sung-Yoon Chung, Jason T. Blocking, Yet-Ming Chiang, and W. Y. Ching. *Electrochem. Solid-State Lett.* **7**, page A131, 2004.
- [117] H. Yamaguchi, K. Oka, and T. Ito. *Physica C* **320**, page 167, 1999.
- [118] K. Yoshida. *Theory of Magnetism*. Springer-Verlag, Berlin, 1996.
- [119] J. Yu, C. Lee, S. Im, and J. Lee. *Rev. Adv. Mater. Sci.* **4**, page 55, 2003.
- [120] F. C. Zhang and T. M. Rice. *Phys. Rev. B* **37**, page 3759, 1988.

Vita

Keeseong Park was born in Taegu, Korea on June 30, 1972, the youngest son of Taseon Jung and Doocheon Park. After graduating Young-Nam high school, Taegu, Korea, in 1991, he entered Seoul National University, Seoul, Korea, in 1992. He graduated in February, 1996, with Bachelor of Science degree in physics. Keeseong continued his study at the same university and received Master of Science degree from the university in February, 1998. He served in the Korean naval academy as an physics instructor and a navy officer from March 1998 to June 2001 to fulfill his military duty. In September, 2001, he entered The Graduate School of The University of Texas at Austin.

Permanent address: Shin-wha APT 205-507,
Shin-Mae Dong 569,
Soo-seong Gu, Taegu, Korea, 706 - 170

This dissertation was typeset with \LaTeX^\dagger by the author.

[†] \LaTeX is a document preparation system developed by Leslie Lamport as a special version of Donald Knuth's \TeX Program.